UNIVERSITY OF ROCHESTER
LABORATORY FOR LASER ENERGETICS

Volume 113
October–December 2007
DOE/SF/19460-804

LLE Review

Quarterly Report

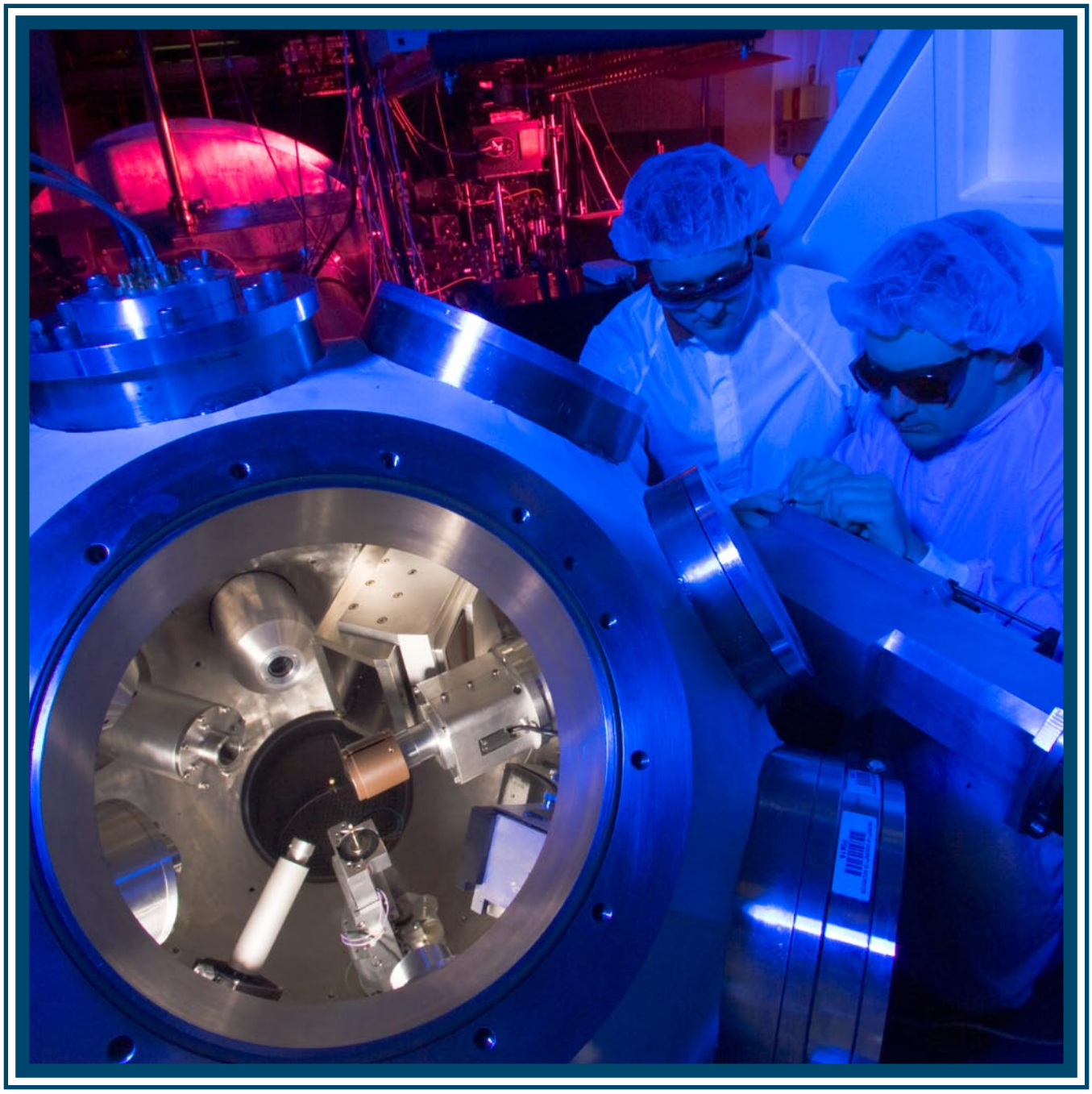

About the Cover:

The Multi-Terawatt (MTW) Laser Facility supports small-scale target-physics experiments (see **High-Intensity Laser–Plasma Interactions in the Refluxing Limit** on p. 1 and **A High-Resolution Optical Transition-Radiation Diagnostic for Fast-Electron Transport Studies** on p. 9), as well as laser- and target-diagnostic development for OMEGA EP. Fusion Science Center for Extreme States of Matter and Fast-Ignition Physics postdoctoral fellow Philip Nilson (left) and The Institute of Optics graduate student Michael Storm (right) prepare the optical transition-radiation diagnostic (TRD) for operation. The optical TRD can be seen through an open chamber port focused on a spherical alignment target at the center of the target chamber. The MTW laser pulse arrives from the grating compressor chamber (highlighted in red in the background) via a vacuum transport tube and turning mirror assembly located inside the target chamber next to the optical TRD. The beam is focused by an *f*/2 off-axis parabolic mirror opposite the optical TRD (not visible). The nose of a single-hit x-ray spectrometer located 23° from target front-surface normal is seen at the lower left-hand side of the port.

Shown is a broader view of the MTW target area where Philip Nilson is aligning the target as viewed on a computer monitor, while Michael Storm is preparing an on-shot laser-temporal diagnostic. A long collimation tube attached to the MTW target chamber supports a charge-coupled-device (CCD) camera (not visible) operating as an x-ray spectrometer in the single-photon–counting mode. Movable lead shielding protects an adjacent area from high-energy x rays produced during some target shots.

The work described in this volume includes current research at the Laboratory for Laser Energetics, which is supported by New York State Energy Research and Development Authority, the University of Rochester, the U.S. Department of Energy Office of Inertial Confinement Fusion under Cooperative Agreement No. DE-FC52-08NA28302, and other agencies.

Printed in the United States of America
Available from
National Technical Information Services
U.S. Department of Commerce
5285 Port Royal Road
Springfield, VA 22161
Price codes: Printed Copy A04
Microfiche A01

For questions or comments, contact Jonathan D. Zuegel, Editor, Laboratory for Laser Energetics, 250 East River Road, Rochester, NY 14623-1299, (585) 275-4425.

Worldwide-Web Home Page: http://www.lle.rochester.edu/

UNIVERSITY OF ROCHESTER
LABORATORY FOR LASER ENERGETICS

Volume 113
October–December 2008
DOE/NA/28302-804

LLE Review

Quarterly Report

UR LLE

Contents

In Brief

This volume of the LLE Review, covering October–December 2007, features "High-Intensity Laser–Plasma Interactions in the Refluxing Limit," by P. M. Nilson, W. Theobald, J. Myatt, C. Stoeckl, M. Storm, O. V. Gotchev, J. D. Zuegel, R. Betti, D. D. Meyerhofer, and T. C. Sangster. In this article (p. 1), the authors report on target experiments using the Multi-Terawatt (MTW) Laser Facility to study isochoric heating of solid-density targets by fast electrons produced from intense, short-pulse laser irradiation. Electron refluxing occurs due to target-sheath field effects and contains most of the fast electrons within the target volume. This efficiently heats the solid-density plasma through collisions. X-ray spectroscopic measurements of absolute K_α (x-radiation) photon yields and variations of the K_β/K_α emission ratio both indicate that laser energy couples to fast electrons with a conversion efficiency of approximately 20%. Bulk electron temperatures of at least 200 eV are inferred for the smallest mass targets.

Additional highlights of recent research presented in this issue include the following:

- M. Storm, I. A. Begishev, R. J. Brown, D. D. Meyerhofer, C. Mileham, J. F. Myatt, P. M. Nilson, T. C. Sangster, C. Stoeckl, W. Theobald, and J. D. Zuegel, along with C. Guo (The Institute of Optics) present the design of a high-resolution optical transition-radiation diagnostic for fast-electron-transport studies using the MTW Laser Facility. Coherent transition radiation is generated as relativistic electrons, generated in high-intensity laser–plasma interactions, exit the target's rear surface and move into vacuum. High-resolution images of the rear-surface optical emission from high-intensity ($I \sim 10^{19}$ W/cm^2) laser-illuminated metal foils have been recorded using a transition radiation diagnostic (TRD). The detector is a scientific-grade charge-coupled-device (CCD) camera that operates with a signal-to-noise ratio of 10^3 and has a dynamic range of 10^4. The TRD has demonstrated a spatial resolution of 1.4 μm over a 1-mm field of view, limited only by the CCD pixel size.

- V. N. Goncharov, T. C. Sangster, P. B. Radha, T. R. Boehly, T. J. B. Collins, R. S. Craxton, J. A. Delettrez, R. Epstein, V. Yu. Glebov, S. X. Hu, I. V. Igumenshchev, S. J. Loucks, J. A. Marozas, F. J. Marshall, J. P. Knauer, P. W. McKenty, S. P. Regan, W. Seka, S. Skupsky, V. A. Smalyuk, J. M. Soures, C. Stoeckl, R. Betti, R. L. McCrory, and D. D. Meyerhofer, along with D. Shvarts (Nuclear Research Center Negev), J. A. Frenje, R. D. Petrasso, C. K. Li, and F. H. Séguin (Plasma Science Fusion Center, MIT), W. Manheimer (RSI), and D. G. Colombant (Naval Research Laboratory) describe the performance of direct-drive cryogenic target implosions on OMEGA. The success of direct-drive-ignition target designs depends on two issues: the ability to maintain the main fuel adiabat at a low level and the control of the nonuniformity growth during the implosion. A series of experiments was performed to study the physics of low-adiabat, high-compression cryogenic-fuel assembly. High-areal-density (with $\rho R > 200$ mg/cm^2) cryogenic-fuel assembly has been achieved on OMEGA in designs where the shock timing was optimized using the nonlocal treatment of the heat conduction and the suprathermal-electron preheat generated by two-plasmon-decay instability was mitigated.

- W. Theobald, R. Betti, C. Stoeckl, K. S. Anderson, J. A. Delettrez, V. Yu. Glebov, V. N. Goncharov, F. J. Marshall, D. N. Maywar, R. L. McCrory, D. D. Meyerhofer, P. B. Radha, T. C. Sangster, W. Seka, V. A. Smalyuk, A. A. Solodov, B. Yaakobi, and C. D. Zhou, along with D. Shvarts (Nuclear Research Center Negev), J. A. Frenje, C. K. Li, F. H. Séguin, and R. D. Petrasso (Plasma Science Fusion Center, MIT), and L. J. Perkins (LLNL) present the results from initial experiments on the shock-ignition inertial confinement fusion concept. Shock ignition is a two-step inertial confinement fusion concept

where a strong shock wave is launched at the end of the laser pulse to ignite the compressed core of a low-velocity implosion. Initial shock-ignition technique experiments used 40-μm-thick, 0.9-mm-diam, warm surrogate plastic shells filled with deuterium gas. These experiments showed a significant improvement in the performance of low-adiabat, low-velocity implosions compared to conventional "hot-spot" implosions. High areal densities with average values exceeding ~200 mg/cm^2 and peak areal densities above 300 mg/cm^2 were measured, which is in good agreement with one-dimensional hydrodynamical simulation predictions. Shock-ignition technique implosions with cryogenic deuterium and deuterium–tritium ice shells also produced areal densities close to the 1-D prediction and achieved up to 12% of the predicted 1-D fusion yield.

- W. Seka, D. H. Edgell, J. P. Knauer, J. F. Myatt, A. V. Maximov, R. W. Short, T. C. Sangster, C. Stoeckl, R. E. Bahr, R. S. Craxton, J. A. Delettrez, V. N. Goncharov, and I. V. Igumenshchev, along with D. Shvarts (Nuclear Research Center Negev) report investigations on time-resolved absorption in cryogenic and room-temperature, direct-drive implosions on OMEGA. Time-dependent and time-integrated absorption fractions are inferred from scattered-light measurements that agree reasonably well with hydrodynamic simulations that include nonlocal electron-heat transport. Discrepancies in the time-resolved scattered-light spectra between simulations and experiments remain for complex laser pulse shapes indicating beam-to-beam energy transfer and commensurate coupling losses. Time-resolved scattered-light spectra near $\omega/2$ and $3\omega/2$, as well as time-resolved hard x-ray measurements, indicate the presence of a strongly driven two-plasmon-decay (TPD) instability at high intensities that may influence the observed laser light absorption. Experiments indicate that energetic electron production due to the TPD instability can be mitigated with high-Z-doped plastic shells.

- J. R. Rygg, F. H. Séguin, C. K. Li, J. A. Frenje, M. J.-E. Manuel, and R. D. Petrasso (Plasma Science Fusion Center, MIT), along with R. Betti, J. A. Delettrez, O. V. Gotchev, J. P. Knauer, D. D. Meyerhofer, F. J. Marshall, C. Stoeckl, and W. Theobald (LLE) report on monoenergetic proton radiography of field and density distributions in inertial confinement fusion implosions. This unique imaging technique reveals field structures through deflection of proton trajectories, and areal densities are quantified through energy lost by protons while traversing the plasma. Two distinctly different types of electromagnetic-field configurations are observed during implosions and the capsule size and areal-density temporal evolution are measured. The first field structure consists of many radial filaments with complex striations and bifurcations that permeate the entire field of view with 60-T magnetic-field magnitudes, while another coherent, centrally directed electric field of the order of 10^9 V/m is seen near the capsule surface. Although the mechanisms for generating these fields are not yet fully understood, their effect on implosion dynamics is expected to be consequential.

Jonathan D. Zuegel
Editor

High-Intensity Laser–Plasma Interactions in the Refluxing Limit

Introduction

Studies of energy transfer from high-intensity laser pulses into solid-density targets address basic issues in laser–plasma interactions, including electron acceleration, ion acceleration, and secondary radiation generation.[1–5] At laser irradiances $I\lambda^2 > 10^{18}$ (W/cm^2)μm^2, where I is the laser intensity and λ is the laser wavelength, electrons are accelerated to relativistic energies and can be used to create unique states of matter. These studies are motivated by a variety of applications in high-energy-density science,[6] including bright backlighter source development[7] and advanced inertial confinement fusion schemes such as fast ignition.[8,9]

Many uncertainties exist in the transport and energy deposition of laser-generated high-current electron beams in dense plasmas. Their propagation is strongly affected by self-generated electromagnetic fields and the ability of the plasma to draw a return current.[10–17] Simple, well-characterized target geometries can identify the dominant laser–plasma and energy-deposition phenomena and can be used for detailed code benchmarking. Of particular interest are methods for isochorically heating solid-density targets to hundreds of eV and many keV using fast electrons[18–24] to infer laser–plasma coupling and heating as a function of laser intensity, wavelength, pulse duration, and preplasma scale length.[25–33]

The fast electrons generated during high-intensity laser–plasma interactions with solid targets of just tens or hundreds of microns in extent and less than a few microns in thickness rapidly create a solid-density, high-energy-density plasma.[25,26] The electrons typically have energies of up to a few MeV and ranges of many hundreds of microns—far greater than the target thickness. The Debye sheath fields that rapidly form at the target surfaces constrain the majority of fast electrons to multiple transits through the target. This process is known as refluxing[3,34,35] and is a particularly efficient mechanism for transferring fast-electron energy into thermal-plasma energy prior to any significant hydrodynamic disassembly.[27–29]

Refluxing in small-mass targets provides a simple geometry for testing laser coupling, fast-electron generation, and plasma-heating models. For example, K-shell spectroscopy using buried fluors, a widely used technique for diagnosing fast-electron transport in massive solid targets,[18,21–23,33,36–38] is not necessary here. The target is so small that by choosing an appropriate mid-Z material (to simplify the ion de-excitation cascades and reabsorption of fluorescent x rays[21,37,39]), the target is the fluor. This is a unique property of the refluxing limit and provides insightful simplifications to the modeling of fast-electron stopping and secondary radiation generation and transport.[28]

Theobald *et al.*[27] have shown that the energy in K_α emission, per joule of laser energy, from a small-mass target is insensitive to the fast-electron spectrum and laser intensity in the relativistic regime. Myatt *et al.*[28] have published modeling of these experiments, taking into account the effect of spatial and temporal gradients, target expansion and heating, and fast-electron refluxing on the absolute and relative emission of K_α and K_β fluorescent lines. This is used to infer the laser-to-electron energy-conversion efficiency $\eta_{L\to e}$, accounting for classical fast-electron stopping and relativistic K-shell ionization cross sections.[40]

This article describes experiments that demonstrate the effect of bulk heating on L ⟶ K and M ⟶ K electron transitions in small-mass copper targets. It has previously been demonstrated using high-resolution K_α spectroscopy that high bulk-electron temperatures can be achieved (hundreds of eV) in a refluxing geometry.[25,26] In our experiment, variations in the K_β/K_α ratio as a function of target volume diagnose the bulk-electron temperature during the rapid isochoric heating phase. This allows the laser-to-electron energy-conversion efficiency $\eta_{L\to e}$ to be inferred by comparing experimental K_β/K_α measurements to numerical target-heating calculations, in addition to inferring the conversion efficiency from the absolute K_α yield.

This is a robust technique for inferring the deposited fraction of laser energy into the target bulk by fast electrons, which is required to create the experimentally observed K-photon yields. In the cold material limit, a laser-to-electron energy-conversion efficiency of $\eta_{L\to e} = (20\pm10)\%$ has been inferred. Laser pulses of 5 J and 1 ps at intensities of $I > 10^{19}$ W/cm^2 are shown to heat smaller-volume targets, culminating in $20 \times 20 \times 2$-μm^3 copper targets reaching the highest bulk-electron temperatures of $T_e > 200$ eV. An average laser-to-electron energy-conversion efficiency of around 20% has been inferred over a wide range of target volumes, in good agreement with cold K_α measurements.

The following sections (1) describe the experimental setup; (2) compare K_α-emission measurements to a model of K_α production from small-mass targets; (3) compare bulk-heating measurements with numerical target-heating calculations; and (4) provide a discussion and summary.

Experimental Setup

The experiments were performed using the Multi-Terawatt (MTW) Laser System at the Laboratory for Laser Energetics. MTW is a hybrid laser system, which operates in the conventional chirped-pulse–amplification (CPA) mode and combines optical parametric amplification (OPA) with Nd-doped laser-glass amplification.[41] The measured contrast ratio after the OPCPA stage is around 10^8 during the 100-ps period prior to the main laser pulse. Maximum output energies >10 J in a transform-limited subpicosecond pulse duration provide peak powers of the order of 10 TW. The energy in the laser pulse, the pulse duration, and the spatial distribution of the laser beam on the compressor output are monitored on a shot-to-shot basis. Typical short-term stability over a period of a few days is 3% rms in energy and 10% rms in the pulse duration.

For the experiments described here, the laser delivered 1- to 5-J, 1-ps pulses and was focused at normal incidence onto planar-foil targets using an *f*/2 off-axis parabola. The focal-spot full width at half maximum was between 4 to 6 μm and provided a peak intensity of up to 2×10^{19} W/cm^2. The targets were copper foils that ranged in cross-sectional area and thickness between $20 \times 20 \times 2$ μm^3 and $500 \times 500 \times 50$ μm^3. Two types of target mounts were used, depending on the target size: 1- to 2-μm-diam spider-silk threads and 17-μm-diam silicon carbide stalks.

Measurements of the time-integrated copper K_α (8.05-keV) and copper K_β (8.91-keV) emission were performed using a spectrometer based on an x-ray charge-coupled-device (CCD) camera operating in the single-photon–counting mode.[42] The spectrometer was located 23° to the target front-surface normal and incorporated extensive lead shielding and collimation tubes to optimize the signal to noise and minimize the detection of hard x-ray photons. It is assumed that K photons are emitted uniformly over 4π steradians and only weakly attenuated by the target plasma itself, prior to reaching the spectrometer. Copper filters of 75- to 150-μm thickness attenuated the K-shell emission, allowing K_α and K_β photons to be transmitted just below the K edge of the filter. The final K-shell spectrum is calculated taking into account the solid angle sampled by the detector, the x-ray CCD quantum efficiency, and the filter transmission.

Measurements of the K_α Yield

High-intensity laser pulses interact with solid-density targets in a short-density-scale-length preplasma. The collisionless absorption of laser energy into relativistic electrons occurs up to the relativistic critical-density surface through $\mathbf{v} \times \mathbf{B}$ acceleration, resonance absorption, vacuum heating, and parametric instabilities.[24,43–45] Electron transport and heating away from the focal spot require that the fast-electron current be opposed by an inductively or electrostatically generated electric field that draws a return current from the thermal background. At the target boundaries, escaping fast electrons rapidly form a Debye sheath that, for sufficiently small targets, provides a potential that prevents a significant fraction of fast electrons from escaping. A MeV electron, for example, which has a range of around 1 mm and a characteristic slowing-down time of approximately 1 ps at solid density, will make multiple transits across a micron-scale-thickness, solid-density plasma before stopping. The high-energy electrons essentially provide their own return current. This reduces the enhanced stopping due to resistive electric fields associated with cold return currents that are found in more-massive targets.[46,47] In this case, resistive inhibition is not important because the characteristic electron range in the resistive electric fields is greater than the foil thickness. A resistive electric field $E_{res} \approx 2 \times 10^5$ kV/cm, which is representative of interaction conditions for copper at a few hundred eV, would stop a 1-MeV electron in 50 μm, assuming a minimum conductivity $\sigma = 1 \times 10^6$ $(\Omega m)^{-1}$ (Ref. 28). This resistive range is greater than the target thickness, allowing the electrons to contribute to the return current over time scales greater than their characteristic target transit time.

K_α emission has been used in many experiments to diagnose fast-electron-energy spectra and electron angular distributions during high-intensity laser–plasma interactions.[18,21,22,33,37] K-photon emission is generated during inelastic collisions

between fast electrons (with energies exceeding the K-shell binding energy) and electrons in the K shell. The fast-electron–induced K-shell vacancy is short lived ($<10^{-12}$ s) and decays through radiative and nonradiative de-excitation. The most important processes for mid-Z elements such as copper is the competition between Auger decay and K-shell fluorescence, which is quantified by the K-shell fluorescence probability.[48] K_α and K_β emission is thus generated during L ⟶ K and M ⟶ K electronic transitions.

The copper K-shell spectrum was investigated as a function of laser intensity using $500 \times 500 \times 20$-μm^3 copper targets to access the cold-material limit by using relatively large-mass targets, while keeping them thin enough to maintain the Debye sheath fields that cause refluxing and minimize opacity effects. Figure 113.1 shows a series of K_α emission measurements (normalized to the laser energy) using 1-ps-duration laser pulses over an intensity range of 5×10^{16} W/cm^2 $< I < 5 \times 10^{20}$ W/cm^2. The intensity on target is varied by changing the laser-spot size and laser energy. Data from the MTW laser (solid circles) are shown and compared to previously published data from the Vulcan PW laser (open circles).[27,28,49]

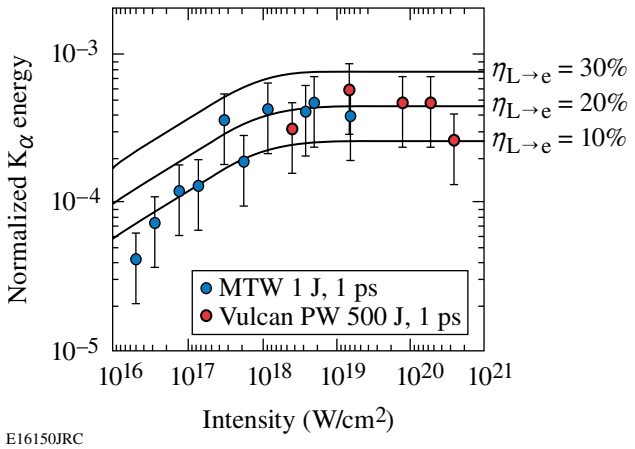

Figure 113.1
K_α energy (normalized to the laser energy) as a function of laser intensity. Data are shown for $500 \times 500 \times 20$-μm^3 copper targets from the MTW laser (solid circles) and the Vulcan PW laser (open circles).[27,28] Predictions from the K_α-production model are shown (solid lines) for laser-to-electron energy-conversion efficiencies $\eta_{L\to e}$ = 10%, 20%, and 30%.

The experimental data in Fig. 113.1 are compared to a model of K_α production (solid black lines) as described in Ref. 27. The model accounts for collisional fast-electron energy transfer only and makes no inference to the spatial homogeneity of the energy deposition, but simply allows the fast electrons to slow down. An exponential fast-electron-energy spectrum is specified using a scaling relationship between the fast-electron temperature T_e and the laser intensity I. The ponderomotive scaling $T_e\,[\text{MeV}] = 0.511\left[\left(1 + I_{18}\lambda^2_{\mu m}/1.37\right)^{1/2} - 1\right]$ is used for $I > 10^{18}$ W/cm^2 (Ref. 24), where I_{18} is the laser intensity in units of 10^{18} W/cm^2 and $\lambda_{\mu m}$ is the laser wavelength in microns. Such a scaling has been shown to become increasingly less accurate at lower laser intensities and is replaced by $T_e\,[\text{MeV}] = 0.05\, I_{18}^{1/3}$, for interactions $I < 10^{18}$ W/cm^2. This phenomenological scaling is extrapolated from existing experimental measurements that are summarized in the review by Gibbon *et al.*[10]

The K_α-production model accounts for two distinct properties afforded by the refluxing process. The fast electrons are allowed to lose all of their energy inside the target, independent of their range, described using the classical slowing-down approximation. Energy is transferred to atomic electrons with high efficiency (>90%),[28] and K-shell vacancies are created during each transit of the target by electrons with energy above the copper K-shell binding energy. This is accounted for in the K-shell ionization cross section, which is modified for relativistic effects.[39,40] There is also a correction for reabsorption of the emitted photons. The K_α transmission of a 20-μm-thick foil, for example, is 70%, which assumes a uniform fast-electron density and an attenuation length of $L = 25$ μm.

The fraction of incident laser energy deposited by fast electrons in the target, which generates the observed K-photon emission, is, to a good approximation, the laser-to-electron energy-conversion efficiency $\eta_{L\to e}$, with ion acceleration effects representing a small energy correction. For laser parameters consistent with the experiments reported here, the measured conversion efficiencies of laser energy into ion acceleration (including protons from surface contamination) are in the range of 0.1% to 2% (Refs. 34, 50–52). The experimentally inferred laser-to-electron energy-conversion efficiency therefore represents, to within experimental error, a minimum of the absolute $\eta_{L\to e}$ value.

The refluxing model predicts the K_α yield as a function of laser intensity for various laser-to-electron energy-conversion efficiencies $\eta_{L\to e}$. Figure 113.1 demonstrates good agreement between the energy emitted by K_α photons (normalized to the laser energy) and the K_α-production model. A conversion efficiency of laser energy into fast electrons $\eta_{L\to e} = (20\pm10)\%$ is inferred for $I > 10^{18}$ W/cm^2. If refluxing were not considered, K-photon production would fall dramatically for $I > 10^{18}$ W/cm^2 because there is insufficient time or material in a single pass of the plasma to support appreciable fast-electron-

energy loss or significant K-shell vacancy creation with an increasing electron range.

The data show that K_α conversion efficiency is a weakly increasing function of laser intensity above $I = 10^{18}$ W/cm^2. This is also a feature of the model, caused by the interplay between the energy dependence of the K-shell ionization cross section and the insensitivity of the K_α generation mechanism to the fast-electron temperature and energy spectrum in the refluxing regime. The effect is demonstrated in both data sets using both 1-J and 500-J laser pulses with comparable 1-ps pulse durations. For $I < 10^{18}$ W/cm^2, the fast-electron temperature T_e reduces and the K_α signal is predicted to decrease with laser intensity. This is a result of the particular energy dependence of the fast-electron range and the K-shell ionization cross section. This has been confirmed experimentally by defocusing the MTW laser and entering the nonrelativistic regime.

Influence of Target Heating on K-Shell Line Emission

The bulk-electron temperature that an initially cold target reaches during refluxing is governed by the target mass and the energy content of the laser-accelerated electrons. Numerical target-heating calculations[28] predict that volumetric heating to $T_e > 100$ eV in small-mass ($<300 \times 300 \times 20$-$\mu$m^3) copper targets is sufficient to collisionally ionize and partially deplete the M shell. Filling of the K-shell vacancy from the M shell will be suppressed and provides diagnostic access to the bulk-plasma environment through variations of the K_β/K_α ratio from that expected in the cold-material limit, as shown in Fig. 113.2. This effect can be used to provide a self-consistency check on the total fast-electron-energy content.

The variation of K_β/K_α as a function of local bulk-electron temperature is shown in Fig. 113.3, based on the calculation reported in Ref. 28, which takes into account the LTE ion population, using the code *PrismSPECT*.[53] Here, K_β/K_α is normalized to the expected cold-material value $K_\beta/K_\alpha = 0.14$. A dramatic reduction in K_β/K_α is demonstrated for bulk-electron temperatures of up to 400 eV, beyond which there are negligible numbers of ions with populated M shells and no K_β emission is possible.

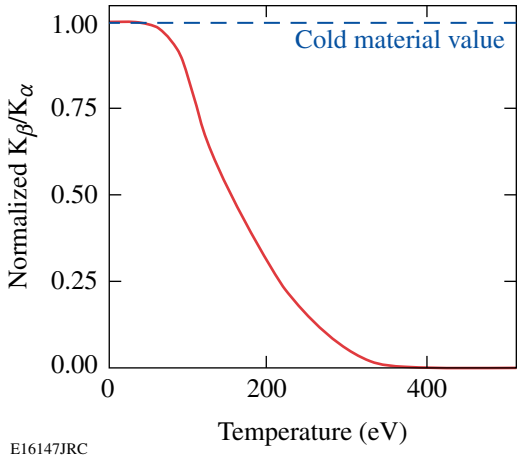

Figure 113.3
K_β/K_α ratio variation with bulk-electron temperature (normalized to the cold-material value).

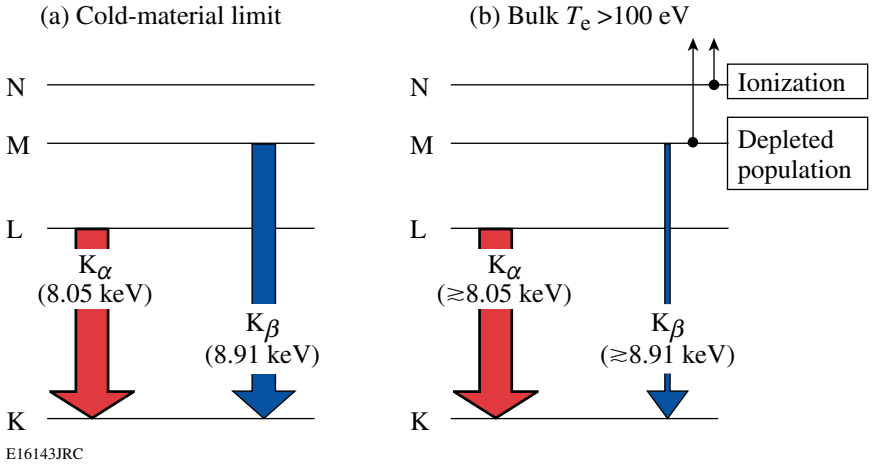

Figure 113.2
Copper-energy levels showing L ⟶ K and M ⟶ K electronic transitions that produce K_α and K_β radiative emission. Two examples are given: (a) a solid-density plasma in the cold-material limit (constant K_β/K_α) and (b) a solid-density plasma with bulk $T_e > 100$ eV (suppressed K_β/K_α). The number of emitted photons during L ⟶ K and M ⟶ K transitions is represented schematically by the relative arrow widths.

Figure 113.4 shows that the influence of bulk heating on K-shell emission predicted by the estimate in Fig. 113.3 is indeed observed experimentally. Examples of copper K-shell spectra are shown for (a) $500 \times 500 \times 50$-μm^3 and (b) $20 \times 20 \times 3$-μm^3 copper targets. The spectra were measured from interactions with 5-J, 1-ps laser pulses at an intensity of $I = 2 \times 10^{19}$ W/cm^2. The K_α and K_β peaks are fit to Gaussian line shapes with a FWHM of 220 eV. M-shell depletion in the $20 \times 20 \times 3$-μm^3 target has significantly reduced the K_β emission in comparison to that measured from the $500 \times 500 \times 50$-μm^3 target.

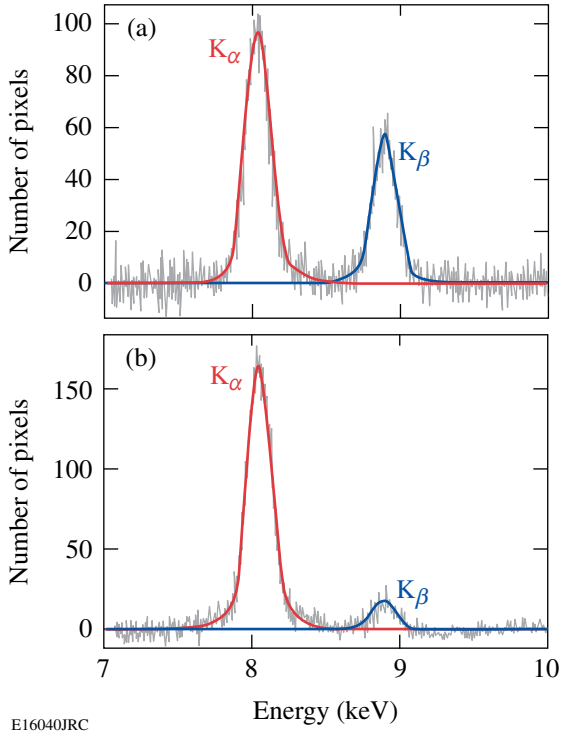

Figure 113.4
Example spectra for (a) $500 \times 500 \times 50$-μm^3 and (b) $20 \times 20 \times 3$-μm^3 copper targets and 5-J, 1-ps laser pulses at intensities $I = 2 \times 10^{19}$ W/cm^2. The K_α and K_β peaks are shown.

The copper K-shell spectrum was measured as a function of target volume for a 1-ps pulse duration and constant laser intensity of $I = 2 \times 10^{19}$ W/cm^2. This shows the variation of K_β/K_α with increasing energy density, achieved by depositing a similar amount of fast-electron energy within decreasing target plasma volumes. Figure 113.5 shows variations in the energy emitted by K_α and K_β photons (normalized to the laser energy) for target volumes of 5×10^{-6} mm^3 < V < 1×10^{-1} mm^3. Three distinct regions are highlighted. In region 1 ($V > 10^{-3}$ mm^3) the ratio of energy emitted in K_α and K_β is constant, consistent with the cold-material value. In region 2 (5×10^{-6} mm^3 < V < 1×10^{-3} mm^3) the energy emitted in K_α remains approximately constant but K_β emission is increasingly suppressed for decreasing plasma volumes. This is consistent with M-shell depletion due to collisional ionization from the thermal background plasma. Any shifts in the K_β emission as M-shell electrons are being removed, however, are not resolved by our spectrometer. At sufficiently high-energy densities, achieved in region 3 ($V < 5 \times 10^{-6}$ mm^3), the energy in both K_α and K_β emission is dramatically suppressed. It is possible that for these very small targets, expansion during the period of active K-shell emission might impact the K_α and K_β yields. In all cases, a hot plasma corona of less than solid density is always present but will contribute negligibly to the total K_α and K_β signal because the emission is naturally weighted toward higher densities. Nonetheless, the total mass of the solid part is, in all cases, considerably larger than in the preplasma/corona during the time of K-shell emission. Figure 113.5 shows the insensitivity of K_α yield to target mass for volumes ranging between 5×10^{-6} to 1×10^{-3} mm^3, suggesting that a significant fraction of the target remains at solid density. Over the same range, however, K_β/K_α drops by almost an order of magnitude.

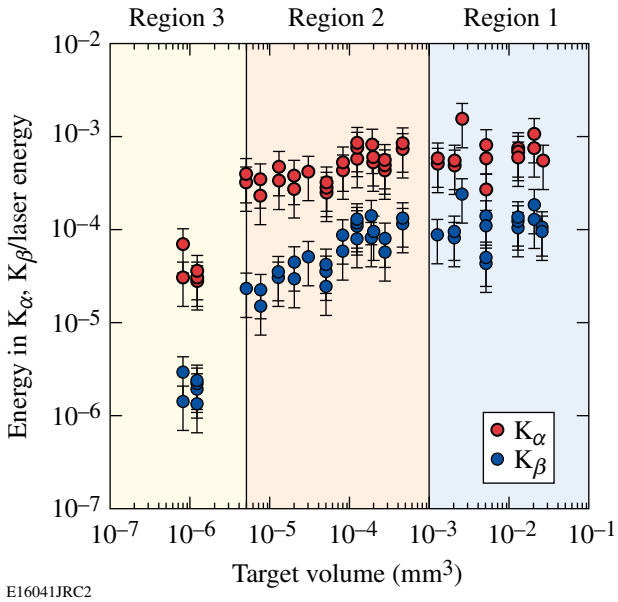

Figure 113.5
Energy in K_α and K_β (normalized to the laser energy) as a function of target volume. Three distinct regions of behavior (1, 2, and 3) in the K-photon emission are identified for increasing energy densities (see text for details).

Figure 113.6 shows the experimentally measured variation in K_β/K_α (left axis; taken from the data presented in Fig. 113.5) as a function of target volume. The error associated with each K_β/K_α value is given by the standard deviation from a number

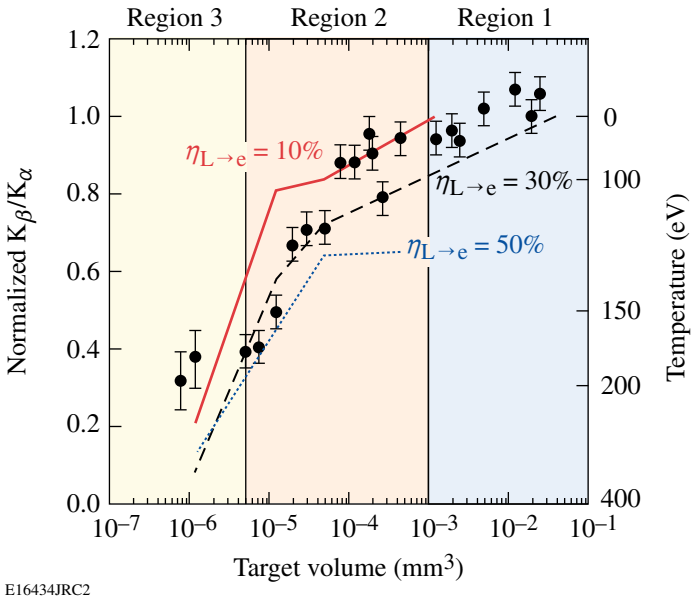

Figure 113.6
K_β/K_α (normalized to the cold-material value—left axis) and bulk-electron temperature (right axis) as a function of target volume. Calculated K_β/K_α [assuming laser-to-electron energy-conversion efficiencies $\eta_{L\to e}$ = 10% (solid line), 30% (dashed line), and 50% (dotted line)] as a function of target volume.

of shots at a given target volume. The right axis shows the corresponding bulk-electron temperatures using the model shown in Fig. 113.3. A 3.5× reduction in K_β/K_α for target volumes $V = 10^{-6}$ mm^3 below the cold-material value is consistent with a bulk-electron temperature $T_e \approx 200$ eV. The drop in K_α yield in region 3 may indicate temperatures even greater than 200 eV, causing L-shell depletion through collisional ionization.

A thorough analysis of K_β/K_α variations requires numerical calculations to take into account the spatial and temporal variations in the fast-electron distribution and the target heating. This is achieved by combining ion-population distribution calculations from the collisional-radiative code *PrismSPECT*[53] with 3-D numerical target-heating calculations[28] using the implicit-hybrid PIC code *LSP*.[54] The fast-electron source is defined in *LSP* by promoting electrons from the cold bulk-electron population at a rate consistent with a constant fraction ($\eta_{L\to e}$) of the laser power. The use of a collisional-radiative code to calculate the ion-population distribution is justified because a copper plasma at a few hundred eV and $n_e = 10^{23}$ cm^{-3} reaches a steady state in around 1 ps and the charge-state dynamics in the plasma is governed by the thermal background, with little influence from the MeV-scale fast-electron component of the distribution function.

Results of this calculation are shown in Fig. 113.6. The calculated variation in K_β/K_α as a function of target volume is shown for $\eta_{L\to e}$ = 10% (solid line), 30% (dashed line), and 50% (dotted line). Good agreement is demonstrated between the experimental K_β/K_α measurements and numerical calculations for $\eta_{L\to e}$ = (20±10)% in the cold-material limit (region 1), consistent with the previous section (p. 4) on K_α emission. This demonstrates that the dominant physical phenomena present in the refluxing limit have been reasonably accounted for in the cold K-photon production model. On average, the variation of K_β/K_α is broadly consistent with a mean laser-to-electron energy-conversion efficiency of around 20%, except for the very smallest mass targets. For target volumes $V < 2 \times 10^{-5}$ mm^3, the theoretical curves begin to converge, making data comparisons increasingly challenging within the experimental uncertainties. Nonetheless, the significant reduction of K_β/K_α in this region below the cold-material limit remains consistent with the smallest mass targets, reaching the highest bulk-electron temperatures.

Discussion and Summary

In summary, high-temperature, solid-density plasmas have been produced and characterized on the MTW Laser System and compared to previous measurements from the Vulcan PW laser. Experiments have shown that absolute K_α yields from copper-foil targets, which are not heated significantly by the refluxing process, are constant for laser–plasma interactions in the relativistic regime. The measured K_α yields are compared to a K_α-production model, which shows good agreement, confirming the weak dependence of K_α generation on laser intensity, fast-electron temperature, and fast-electron range for $I > 10^{18}$ W/cm^2. Using this comparison, a laser-to-electron energy-conversion efficiency of $\eta_{L\to e}$ = (20±10)% has been inferred in the cold-material limit. Variations in K_β/K_α over a range of target volumes (and energy density) for $T_e > 100$ eV have been measured. Experiments show numerical target-heating calcula-

tions are in good agreement with experimental observations over a wide range of target volumes that are broadly consistent with laser-to-electron energy-conversion efficiencies inferred from the simple K_α-production model.

The exploitation of refluxing in small-mass targets offers exciting potential. It provides a readily achievable method for the creation of extremely high-energy-density plasmas using the next generation of multikilojoule-class, high-intensity laser facilities, such as OMEGA EP.[55] These studies will provide new insights into electron generation, transport, and radiative emission of plasmas at unprecedented energy densities and under conditions relevant to fast ignition. On the basis of these experiments, the combined use of absolute K_α yields and K_β/K_α variations with increasing bulk-electron temperatures presents a method for determining the fast-electron-energy content. This implies that for picosecond-pulse-duration interactions in the relativistic regime, the laser energy is more important than the laser intensity for maximizing the fast-electron-energy content. This has far-reaching ramifications for the creation of high-energy-density plasmas using fast-electron–induced isochoric heating. Future experiments on OMEGA EP, for example, will use small-mass targets to access unprecedented energy densities using fast-electron–driven isochoric heating. Variations in the laser intensity and pulse duration up to the multikilojoule, 10-ps regime will make possible the formation of high-temperature, solid-density plasma in the 1- to 10-keV range.

ACKNOWLEDGMENT

This work was supported by the U.S. Department of Energy under Cooperative Agreement Nos. DE-FC52-08NA28302 (Office of Inertial Confinement Fusion) and DE-FC02-ER54789 (Fusion Science Center, Office of Inertial Fusion Energy Science), the University of Rochester, and the New York State Energy Research and Development Authority. The support of DOE does not constitute an endorsement by DOE of the views expressed in this article.

REFERENCES

1. F. N. Beg *et al*., Phys. Plasmas **4**, 447 (1997).
2. E. L. Clark *et al*., Phys. Rev. Lett. **85**, 1654 (2000).
3. S. P. Hatchett, C. G. Brown, T. E. Cowan, E. A. Henry, J. S. Johnson, M. H. Key, J. A. Koch, A. B. Langdon, B. F. Lasinski, R. W. Lee, A. J. MacKinnon, D. M. Pennington, M. D. Perry, T. W. Phillips, M. Roth, T. C. Sangster, M. S. Singh, R. A. Snavely, M. A. Stoyer, S. C. Wilks, and K. Yasuike, Phys. Plasmas **7**, 2076 (2000).
4. R. D. Edwards *et al*., Appl. Phys. Lett. **80**, 2129 (2002).
5. M. H. Key, M. D. Cable, T. E. Cowan, K. G. Estabrook, B. A. Hammel, S. P. Hatchett, E. A. Henry, D. E. Hinkel, J. D. Kilkenny, J. A. Koch, W. L. Kruer, A. B. Langdon, B. F. Lasinski, R. W. Lee, B. J. MacGowan, A. MacKinnon, J. D. Moody, M. J. Moran, A. A. Offenberger, D. M. Pennington, M. D. Perry, T. J. Phillips, T. C. Sangster, M. S. Singh, M. A. Stoyer, M. Tabak, G. L. Tietbohl, M. Tsukamoto, K. Wharton, and S. C. Wilks, Phys. Plasmas **5**, 1966 (1998).
6. B. A. Remington *et al*., Science **284**, 1488 (1999).
7. H.-S. Park, D. M. Chambers, H.-K. Chung, R. J. Clarke, R. Eagleton, E. Giraldez, T. Goldsack, R. Heathcote, N. Izumi, M. H. Key, J. A. King, J. A. Koch, O. L. Landen, A. Nikroo, P. K. Patel, D. F. Price, B. A. Remington, H. F. Robey, R. A. Snavely, D. A. Steinman, R. B. Stephens, C. Stoeckl, M. Storm, M. Tabak, W. Theobald, R. P. J. Town, J. E. Wickersham, and B. B. Zhang, Phys. Plasmas **13**, 056309 (2006).
8. M. Tabak *et al*., Phys. Plasmas **1**, 1626 (1994).
9. M. H. Key, Phys. Plasmas **14**, 055502 (2007).
10. P. Gibbon and E. Förster, Plasma Phys. Control. Fusion **38**, 769 (1996).
11. M. Tatarakis *et al*., Phys. Rev. Lett. **81**, 999 (1998).
12. M. Borghesi *et al*., Phys. Rev. Lett. **83**, 4309 (1999).
13. L. Gremillet *et al*., Phys. Rev. Lett. **83**, 5015 (1999).
14. J. A. Koch *et al*., Phys. Rev. E **65**, 016410 (2001).
15. Y. T. Li *et al*., Phys. Rev. E **64**, 046407 (2001).
16. R. J. Kingham and A. R. Bell, Phys. Rev. Lett. **88**, 045004 (2002).
17. J. R. Davies *et al*., Phys. Rev. E **56**, 7193 (1997).
18. J. D. Hares *et al*., Phys. Rev. Lett. **42**, 1216 (1979).
19. S. J. Gitomer *et al*., Phys. Fluids **29**, 2679 (1986).
20. B. Luther-Davies, A. Perry, and K. A. Nugent, Phys. Rev. A **35**, 4306 (1987).
21. H. Chen, B. Soom, B. Yaakobi, S. Uchida, and D. D. Meyerhofer, Phys. Rev. Lett. **70**, 3431 (1993).
22. K. B. Wharton *et al*., Phys. Rev. Lett. **81**, 822 (1998).
23. K. Yasuike *et al*., Rev. Sci. Instrum. **72**, 1236 (2001).
24. S. C. Wilks *et al*., Phys. Rev. Lett. **69**, 1383 (1992).
25. G. Gregori *et al*., Contrib. Plasma Phys. **45**, 284 (2005).
26. S. N. Chen *et al*., Phys. Plasmas **14**, 102701 (2007).
27. W. Theobald, K. Akli, R. Clarke, J. Delettrez, R. R. Freeman, S. Glenzer, J. Green, G. Gregori, R. Heathcote, N. Izumi, J. A. King, J. A. Koch, J. Kuba, K. Lancaster, A. J. MacKinnon, M. Key, C. Mileham, J. Myatt, D. Neely, P. A. Norreys, H.-S. Park, J. Pasley, P. Patel, S. P. Regan, H. Sawada, R. Shepherd, R. Snavely, R. B. Stephens, C. Stoeckl, M. Storm, B. Zhang, and T. C. Sangster, Phys. Plasmas **13**, 043102 (2006).
28. J. Myatt, W. Theobald, J. A. Delettrez, C. Stoeckl, M. Storm, T. C. Sangster, A. V. Maximov, and R. W. Short, Phys. Plasmas **14**, 056301 (2007).

29. P. M. Nilson, W. Theobald, J. Myatt, C. Stoeckl, C. Mileham, I. A. Begishev, J. Brown, J. D. Zuegel, R. Betti, D. D. Meyerhofer, and T. C. Sangster, "Laser-to-Electron Energy Conversion Efficiency and Bulk Heating of Solid-Density Matter During High-Intensity Laser-Plasma Interactions in the Refluxing Limit," submitted to Physical Review Letters.

30. K. Eidmann *et al*., J. Quant. Spectrosc. Radiat. Transf. **81**, 133 (2003).

31. A. Saemann *et al*., Phys. Rev. Lett. **82**, 4843 (1999).

32. Z. Jiang *et al*., Phys. Plasmas **2**, 1702 (1995).

33. A. Rousse *et al*., Phys. Rev. E **50**, 2200 (1994).

34. A. J. Mackinnion, Phys. Rev. Lett. **88**, 215006 (2002).

35. R. A. Snavely, M. H. Key, S. P. Hatchett, T. E. Cowan, M. Roth, T. W. Phillips, M. A. Stoyer, E. A. Henry, T. C. Sangster, M. S. Singh, S. C. Wilks, A. MacKinnon, A. Offenberger, D. M. Pennington, K. Yasuike, A. B. Langdon, B. F. Lasinski, J. Johnson, M. D. Perry, and E. M. Campbell, Phys. Rev. Lett. **85**, 2945 (2000).

36. R. Kodama *et al*., Phys. Plasmas **8**, 2268 (2001).

37. D. C. Eder *et al*., Appl. Phys. B **70**, 211 (2000).

38. R. Kodama *et al*., Nature **412**, 798 (2001).

39. M. Green and V. E. Cosslett, J. Phys. D **1**, 425 (1968).

40. H. Kolbenstvedt, J. Appl. Phys. **38**, 4785 (1967).

41. V. Bagnoud, I. A. Begishev, M. J. Guardalben, J. Puth, and J. D. Zuegel, Opt. Lett. **30**, 1843 (2005).

42. C. Stoeckl, W. Theobald, T. C. Sangster, M. H. Key, P. Patel, B. B. Zhang, R. Clarke, S. Karsch, and P. Norreys, Rev. Sci. Instrum. **75**, 3705 (2004).

43. F. Brunel, Phys. Rev. Lett. **59**, 52 (1987).

44. N. A. Ebrahim *et al*., Phys. Rev. Lett. **45**, 1179 (1980).

45. K. Estabrook and W. L. Kruer, Phys. Fluids **26**, 1888 (1983).

46. A. R. Bell *et al*., Plasma Phys. Control. Fusion **39**, 653 (1997).

47. F. Pisani *et al*., Phys. Rev. E **62**, R5927 (2000).

48. W. Bambynek *et al*., Rev. Mod. Phys. **44**, 716 (1972).

49. Previously published data[27] incorrectly accounted for photon attenuation by the target. The diagnostic observation angle with respect to the target normal was incorrectly stated as 16°; in fact it was 60° and the present data set takes the correct angle into account.

50. L. Robson *et al*., Nat. Phys. **3**, 58 (2007).

51. J. Fuchs *et al*., Nat. Phys. **2**, 48 (2006).

52. P. K. Patel *et al*., Phys. Rev. Lett. **91**, 125004 (2003).

53. Prism Computational Sciences, Inc., Madison, WI 53711.

54. D. R. Welch *et al*., Phys. Plasmas **13**, 063105 (2006).

55. C. Stoeckl, J. A. Delettrez, J. H. Kelly, T. J. Kessler, B. E. Kruschwitz, S. J. Loucks, R. L. McCrory, D. D. Meyerhofer, D. N. Maywar, S. F. B. Morse, J. Myatt, A. L. Rigatti, L. J. Waxer, J. D. Zuegel, and R. B. Stephens, Fusion Sci. Technol. **49**, 367 (2006).

A High-Resolution Optical Transition Radiation Diagnostic for Fast-Electron Transport Studies

Introduction

High-current relativistic electron beams are generated by high-intensity laser interactions with solids.[1] These electron beams may have applications in compact, tabletop-based, high-brightness laser–plasma particle accelerators,[2] narrowband x-ray sources for medical applications,[3] x-ray sources for high-density inertial fusion energy (IFE) target backlighter radiography,[4] and collimated electron beams required for the fast-ignition approach to IFE.[5] The MeV fast electrons are generated in high-intensity laser–matter interactions, and their subsequent motion must be understood if their potential applications are to be fully realized. A promising technique that provides information about the fast-electron energy and divergence, as well as spatial and temporal distribution inside the target, is spatially resolving the spectrum of transition radiation (TR).[6] TR is emitted when a charged particle passes through a refractive index interface,[7] as in the case of fast electrons exiting a metal foil into vacuum. The emitted electromagnetic energy is undetectably small for a single electron; however, laser–solid interactions typically produce a large number of fast electrons whose individual contributions sum to provide a measurable signal. If the fast-electron beam possesses a strongly correlated longitudinal electron-density structure, the electromagnetic emission can undergo a considerable coherent enhancement, producing coherent transition radiation (CTR).[8] This enhancement is restricted to a narrow spectral band determined by the details of the longitudinal fast-electron density profile. Electrons accelerated by laser–matter interactions have the required longitudinal density profile to generate the CTR.[9] The exact form of this profile depends on the nature of the dominant acceleration mechanism. For example, the resonance absorption process[10] accelerates electrons into the target once per optical cycle, whereas the $\vec{v} \times \vec{B}$ component of the Lorentz force[11] accelerates electrons twice every optical cycle. These electrons then travel through the target as a train of microbunches separated in time by an optical period or half an optical period, generating a CTR signal at the fundamental or second harmonic of the laser frequency, respectively. The spatial-intensity distribution and spectrum of the CTR emission provide information about the electron-transport physics in solid density.[12]

Experimental Setup

A transition radiation diagnostic (TRD) has been designed to acquire high-resolution images of rear-side optical emission at the second harmonic ($\lambda \sim 527$ nm) of the laser frequency from laser-illuminated planar targets. In the optical design shown in Fig. 113.7, a 20× infinity corrected objective,[13] with a 20-mm working distance, a numerical aperture of 0.42, a 1.2-mm field of view, a 1.6-μm depth of focus, and a 0.7-μm resolving power, collects the optical emission from the target's rear surface. A 150-μm-thick sacrificial glass microscope cover slip, acting as a debris shield, is placed on the target side of the objective. The objective is mounted on a motorized 1-D linear actuator[14] with a 10-mm full range of motion and a 20-nm step size. The objective has an exit pupil diameter of 8.4 mm. A 4-mm-thick Schott KG5 glass filter with $\sim 10^{-10}$ transmission at $\lambda = 1053$ nm and ~70% transmission from $\lambda = 400$ to 600 nm prevents laser light from propagating through the system.[15] A 200-mm-focal-length achromatic lens focuses the light through a pinhole that blocks stray light. A narrowband 50/50 beam splitter steers the signal beam through 90°, and a unit magnification optical arrangement relays the light to the detector. A 24-nm bandpass filter centered on $\lambda = 529$ nm is placed in the collimated region of this path.[16] Optical-quality, neutral-density (ND) filters can be placed here to control the level of the signal without significantly compromising the spatial resolution. The overall transmission of the TRD at $\lambda = 527$ nm is ~20%. The detector is a Spectral Instruments (SI) 800-series charge-coupled-device (CCD) camera with a dynamic range of 10^4 (Ref. 17). The 14-mm × 14-mm front-illuminated chip is composed of 1024 × 1024, 13.5-μm × 13.5-μm pixels with a full-well capacity of 10^5 electrons. At $\lambda = 527$ nm the CCD quantum efficiency is 20%. The CCD chip is cooled to –40°C to minimize dark current (<0.1 e^-/pixel/s). The readout rate for the 16-bit analog-to-digital converter can be varied from 100 to 800 kHz, with a read noise of <5 electrons at the slowest speed.

To obtain high-resolution images of the target's rear-surface emission, the microscope objective must be positioned 20 mm away from the rear surface with ~1-μm precision. This is accomplished by using the second arm of the optical system

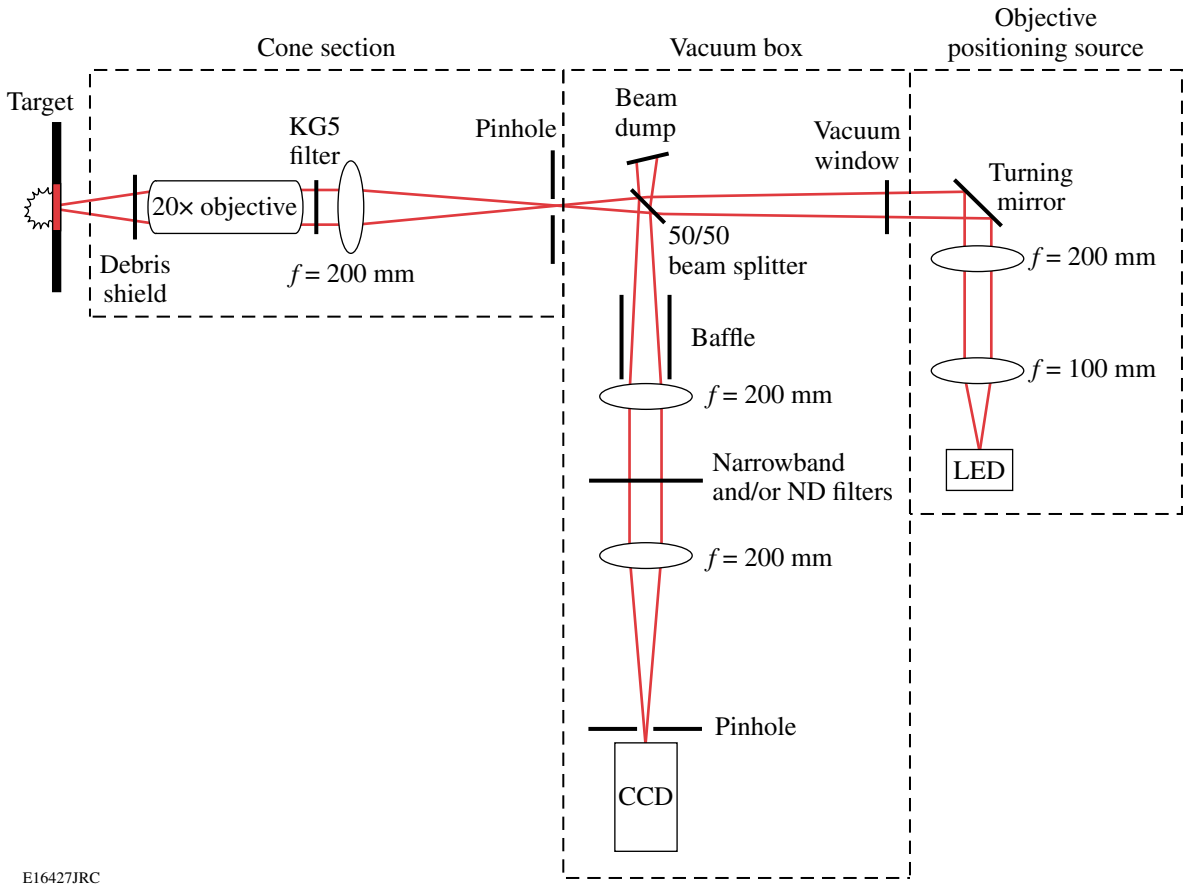

Figure 113.7
A schematic layout of the TRD optical system. Light emitted from the rear side of the target is magnified and relayed to a CCD camera. Filters and pinholes minimize background contributions. The right arm of the system is used only for pre-shot focusing on the rear surface.

(Fig. 113.7). Light from an ultrabright green LED[18] is transmitted through the collection optics and reflected off the target's rear side. Small-scale surface features present on the rear surface of the target act as focusing fiducials and are imaged onto the CCD camera. The camera's external shutter control channel is used to synchronize the LED illumination with the CCD chip exposure period. The CCD exposure time and readout speed are selected to accommodate the ND filter strength for the duration of this procedure. They are returned to standard values of 1 s and 400 kHz, respectively, for the experiment. The baffle and beam dump shown in Fig. 113.7 minimize the propagation of stray LED light through the system during positioning.

The TRD shown in Fig. 113.8 is comprised of two sections: The cone section resides inside the target chamber and is mounted on a target chamber port flange. The rear section, the TRD vacuum box, is attached to the outside face of the cone section. The rear panel of the vacuum box can be removed (as

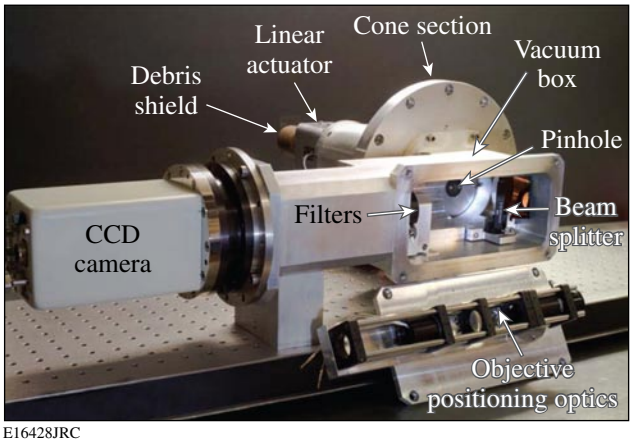

Figure 113.8
A photograph of the TRD with the rear-side access panel removed and laid along side. A detailed discussion of the device is found in the text.

shown in Fig. 113.8) for easy access to the filtering optics and pinhole between shots. Vent holes in the KG5 filter mount link the TRD vacuum box volume to that of the target chamber, allowing the TRD to be pumped. This allows the CCD camera to be operated in vacuum without an independent vacuum system. Operating pressure is reached within 12 min. The TRD vacuum box can be isolated from the main volume of the target chamber by replacing the KG5 filter mount and allowing the KG5 filter to act as a vacuum window. A computer-controlled linear actuator provides high-precision positioning of the microscope objective (see Fig. 113.9). The objective is mounted to the carriage and driven by a pico-motor with a 20-nm step size over a 10-mm range. An encoder using a holographically ruled grating[19] provides closed-loop control of the objective position with ~0.5-μm precision. The system is enclosed in an aluminum casing. To mitigate the risks posed to the actuator circuitry by electromagnetic pulses, it is disconnected during the shot. The actuator maintains its position when powered down.

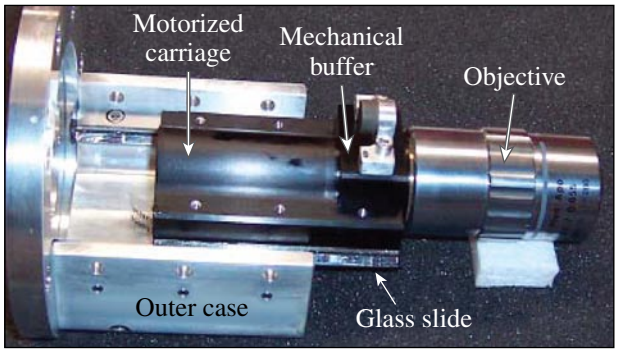

E16429JRC

Figure 113.9
The microscope objective is firmly held by the carriage, which glides in and out smoothly on rails attached to the inside of the outer case. The New Focus pico motor (not shown) is housed in the upper outer case and attached to the carriage via the mechanical buffer. It moves the objective in 20-nm steps over a range of 10 mm. Attached to the under side of the carriage is a glass slide encoded with a holographic ruler with 1-μm graduations. The hologram is read out from below by a reader embedded in the lower outer case to provide closed-loop positioning control.

The TRD was deployed on experiments conducted on LLE's Multi-Terawatt (MTW) Laser Facility.[20] This system is a front-end prototype for OMEGA EP.[21] The TRD is mounted on the MTW target chamber (shown in Fig. 113.10), where it occupies the port directly facing the off-axis parabolic focusing mirror. This assignment drove many components of the mechanical design. Significant amounts of γ radiation are produced in the forward direction during a high-intensity laser-target shot.[22] To prevent this radiation from contaminating the CTR signal, the system is folded through 90° so that the detector can be

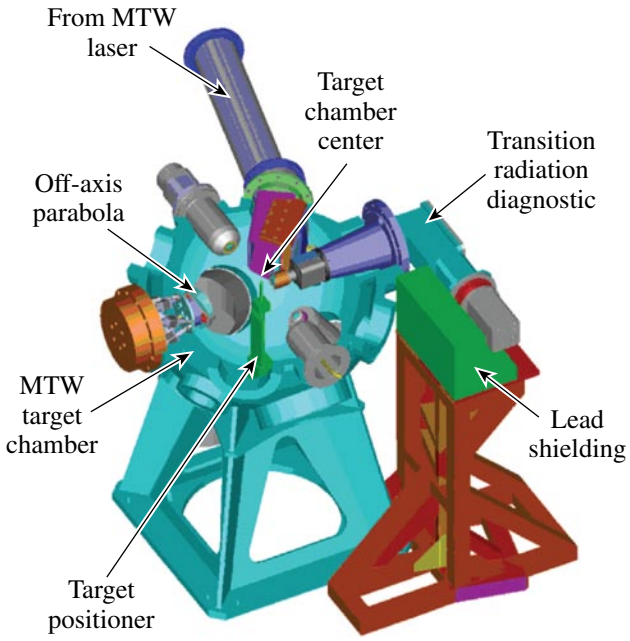

E16430JRC

Figure 113.10
A 3-D model of the MTW target chamber. An off-axis parabola (OAP) steers the MTW laser beam to focus at target chamber center (TCC). The TRD is housed in the port directly opposite the OAP. It images the rear-side optical emission from a normally illuminated target placed at TCC. The TRD optical system is folded through 90° so that the CCD camera lies in the γ-ray shadow of the TRD lead shielding.

shielded behind a 10-cm-thick lead brick wall. An additional 2-mm lead shield (not shown in Fig. 113.10) is placed around the CCD camera to minimize single hits by scattered γ rays arriving from the rear and top sides. Figure 113.11 illustrates the effect of the lead shielding in suppressing the number of γ-ray single hits. The images were taken under nearly identical experimental conditions. The solid-curve histogram was taken with no lead shielding in place. Individual γ rays are seen to produce pixel values of up to ~4000 analog-to-digital units. A reduction in the number of single hits by more than an order of magnitude was observed on the subsequent shot with the lead shielding in place (dashed-curve histogram).

System Performance

The calculated optical transmission curve for the TRD is shown in Fig. 113.12. The transmission of individual optical components was obtained either from the corresponding data sheet or by direct measurement using a spectrophotometer.[23] The curve shows that the transmission varies by 15 orders of magnitude between λ = 1053 nm and λ = 527 nm, so the laser light makes no contribution to an image obtained using the TRD. This was verified with 3-J laser shots taken on 20-μm-

thick, 500-μm-sq iron foils with the 24-nm bandpass filter replaced by an RG1000 filter glass.[15] This material efficiently transmits at the laser frequency while strongly attenuating its second harmonic. The results indicate that no light at the laser frequency enters the optical system.

The optical resolution of the TRD was determined by measuring the modulation transfer function (MTF).[24] The MTF of an imaging system is a measure of the image contrast at the object spatial frequencies; it describes with what efficiency the system can pass each spatial frequency in the object plane. The optical resolution can be defined as the reciprocal of the highest frequency passed at which the contrast is maintained above a specified value. Tatian[25] has shown that the MTF can be obtained directly by analyzing equally spaced samples of the image edge function, which is the image space conjugate of a back-illuminated half plane as described below.

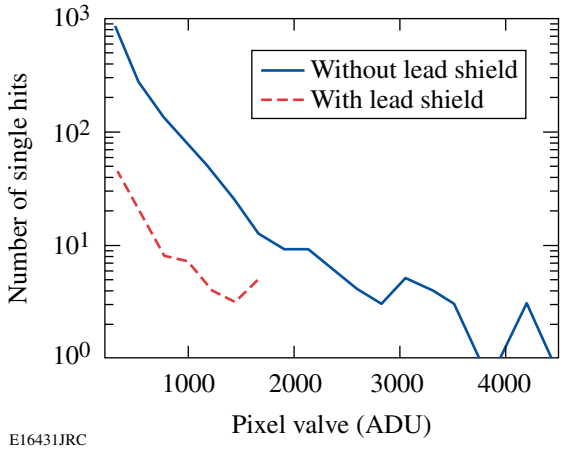

Figure 113.11
Histogram of the number of γ-ray single hits from two shots conducted under almost identical conditions. The pixel values are shown in analog-to-digital units (ADU's). The solid curve corresponds to a shot taken without lead shielding; the dashed curve corresponds to a shot with the lead shielding in place, demonstrating the efficiency of TRD shielding in suppressing the number of γ-ray photons incident on the CCD.

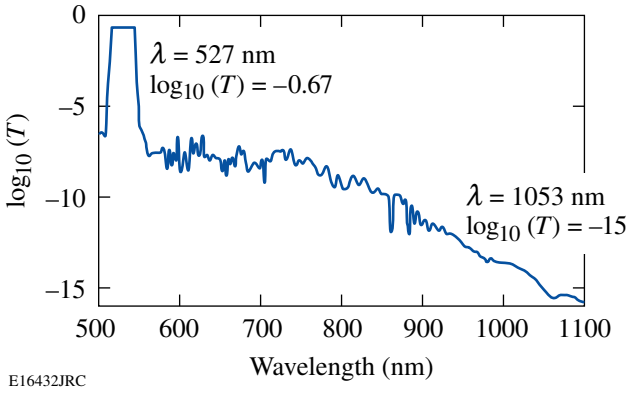

Figure 113.12
The optical transmission curve for the TRD. The transmission efficiency at the laser second harmonic, $\lambda = 527$ nm, is ~20%. The transmission efficiency at the laser wavelength, $\lambda = 1053$ nm, is ~15 orders of magnitude lower.

The experimental half plane was provided by an edge in a scanning electron microscope (SEM) 400-resolution grid [see Fig. 113.13(b)]. The grid was placed in the focal plane of the 20× objective, and an ultrabright LED illuminated the grid from its front side. The illumination was evenly distributed over the object plane to ensure good contrast in the object. The amount of stray light entering the optical system was minimized by mounting the SEM grid in a pinhole and constructing a set

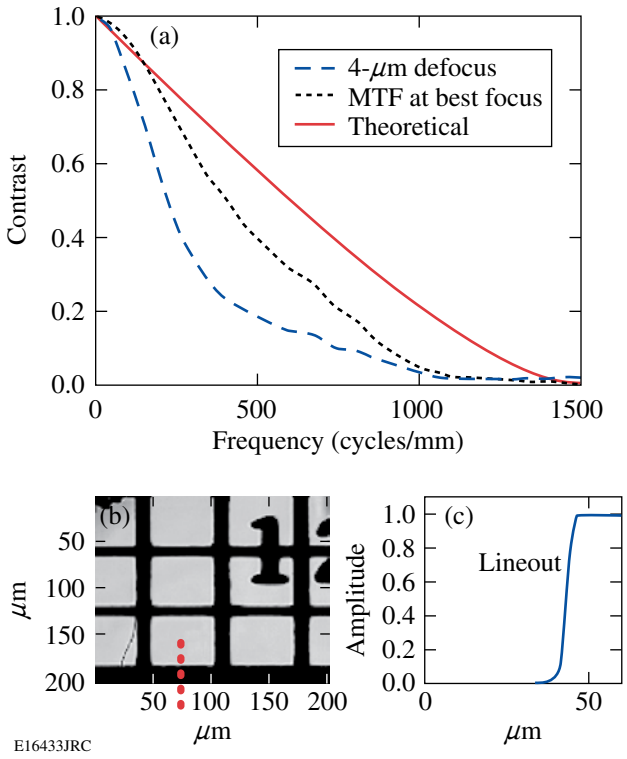

Figure 113.13
(a) The modulation transfer function (MTF) of the TRD. The curves are produced by analyzing images obtained using the TRD fitted with a 20× microscope objective. The solid line shows the theoretical MTF. The measured MTF at best focus is indicated by the dotted line; the contrast falls to ~1/10 at around 900 cycles/mm corresponding to a spatial resolution of ~1.1 μm. The dashed-line MTF expresses the effect of defocusing the collection optics. A 4-μm defocus reduces the optical performance of the system. (b) A section of an SEM 400-resolution grid. The dotted line indicates the position from which the lineout shown in (c) was taken. The lineout is normalized and used to calculate the MTF.

of opaque screens around the objective. The objective was positioned so that the grid was slightly defocused before being scanned through best focus. An image of the SEM grid was obtained every 500 nm, after which the images were post-processed to obtain the MTF. Figure 113.13(c) shows a normalized lineout, at best focus, taken through the image edge function. The CCD camera cannot sufficiently sample the image edge function with a 20× magnification, so it was necessary to linearly interpolate the data to effectively double the sampling rate to avoid aliasing in the MTF. Figure 113.13(a) shows the MTF for the case where a debris shield was placed in front of the objective. The solid line is the theoretical MTF; the dotted line shows the measured MTF at best focus. The limit of the spatial resolution is defined here to be the point at which the contrast ratio is ~10%. At best focus this corresponds to a spatial frequency of approximately 900 cycles/mm or 1.1 μm. Since it was necessary to linearly interpolate the image edge function, the value of 1.1 μm corresponds to the MTF of the optical part of the system. The CCD camera limits the optical resolution of the full system to ~1.4 μm, the size of a CCD pixel over the full field of view. This pixel-size–imposed limit could be reduced by increasing the system's magnification. The effect of defocus is illustrated in Fig. 113.13(a) by the dashed line MTF. A 4-μm defocus of the TRD collection optics reduces the MTF-limited resolution to about 1.5 μm at 10% contrast with the contrast falling about twice as fast as in the best-focus case.

The TRD has been fielded on experiments conducted to diagnose electron transport in a variety of solid materials of varying thickness under differing laser conditions. Figure 113.14 shows three characteristic images of the rear-side emission in both a linear (top) and a logarithmic (bottom) scale. From left to right the targets are 20-μm-thick aluminum, 30-μm-thick aluminum and 50-μm-thick copper; all are 500 μm in the transverse directions. These images are produced by light emitted at the target's rear surface in a narrow spectral window around λ = 527 nm, the laser second harmonic. The emission can be explained as CTR caused by a density-modulated relativistic electron beam generated by the $\vec{v} \times \vec{B}$ component of the Lorentz force. The upper-frame images clearly indicate the presence of small-scale structures, ~≥2 μm in the emission region, which is indicative of electron-beam filamentation.[26] The lower-frame images show that the filamentary structures are superimposed onto a ring-like structure. The annular pattern is almost always observed and suggests that only the electrons accelerated along the beam envelope possess the required density modulation to be observed with the CTR technique. Our calculations suggest that these electrons make up only a small fraction, <5%, of the total fast-electron population.

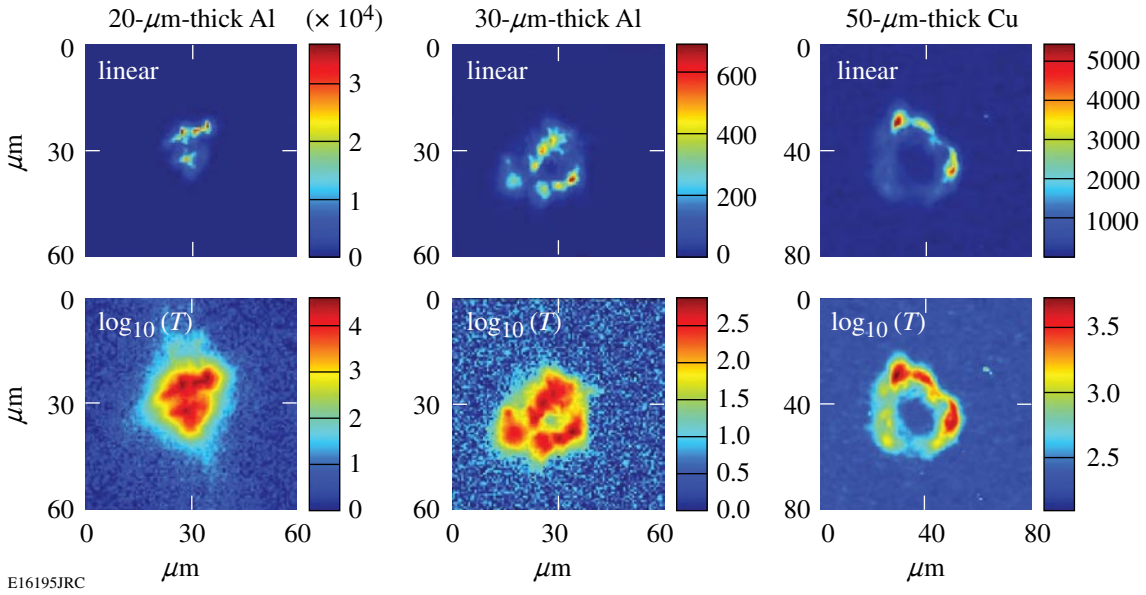

Figure 113.14
Images of the rear-side optical emission from thin foil targets normally illuminated with a laser intensity of 10^{19} W/cm^2. The upper row shows the images plotted on a linear scale, while the lower row shows the corresponding log-scale representation. From left to right the images are from 20-μm-thick aluminum, 30-μm-thick aluminum, and 50-μm-thick copper. The upper-frame images indicate the presence of filamentary structures in the emission pattern. The lower images are demonstrating that the background emission pattern possesses an annular property.

Figure 113.14 further indicates that the spatial size of the emission region increases with target thickness. This is presented explicitly in Fig. 113.15, where the radius of the observed emission pattern is plotted against the target thickness. A least squares fit to the data shows that the beam diverges inside the target with a half angle of ~16°. The corresponding intercept with the radius axis indicates that the beam emerges from a source of radius ~4 μm, consistent with the spatial size of the focused MTW laser beam.

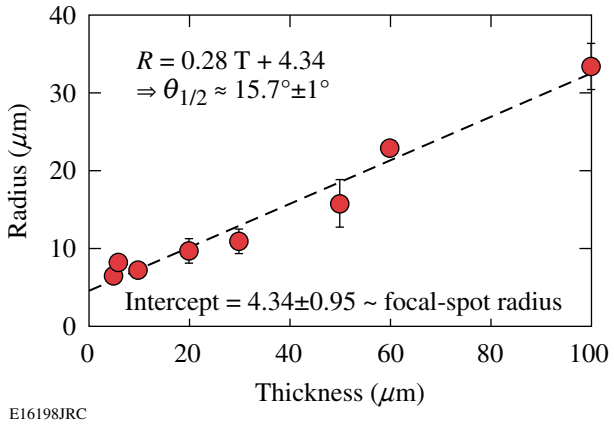

Figure 113.15
The size of the rear-surface emission region grows with target thickness. The growth is consistent with a fast-electron divergence angle of 16°. The data has been fitted using a least squares routine. The intercept of the least squares fit with the radius axis, representing the size of the electron source, is ~4.5 μm and consistent with the size of the laser focus.

Summary

A coherent transition radiation diagnostic has been developed to image the rear-side emission from high-intensity-laser–irradiated foil targets. The device has been optimized to measure radiation in a 24-nm bandwidth around λ = 529 nm with a dynamic range of 10^4. The transmission at λ = 527 nm is 15 orders of magnitude higher than the transmission at the laser frequency, and no laser light has been detected in the system during experiments. We have demonstrated, by measuring the modulation transfer function, that the CCD pixel size limits spatial resolution to 1.4 μm. The diagnostic is being used to infer information about the transport of high-current relativistic electron beams through solid targets. Small-scale structures, ~2 μm in size, have been observed in the rear-surface emission of metal foils irradiated with laser intensities of ~10^{19} W/cm^2. These are indicative of electron-beam filamentation.

ACKNOWLEDGMENT

This work was supported by the U.S. Department of Energy Office of Inertial Confinement Fusion under Cooperative Agreement No. DE-FC52-08NA28302, the University of Rochester, and the New York State Energy Research and Development Authority. The support of DOE does not constitute an endorsement by DOE of the views expressed in this article.

REFERENCES

1. M. H. Key, M. D. Cable, T. E. Cowan, K. G. Estabrook, B. A. Hammel, S. P. Hatchett, E. A. Henry, D. E. Hinkel, J. D. Kilkenny, J. A. Koch, W. L. Kruer, A. B. Langdon, B. F. Lasinski, R. W. Lee, B. J. MacGowan, A. MacKinnon, J. D. Moody, M. J. Moran, A. A. Offenberger, D. M. Pennington, M. D. Perry, T. J. Phillips, T. C. Sangster, M. S. Singh, M. A. Stoyer, M. Tabak, G. L. Tietbohl, M. Tsukamoto, K. Wharton, and S. C. Wilks, Phys. Plasmas **5**, 1966 (1998).
2. T. Katsouleas, Nature **444**, 688 (2006).
3. K. K. Kainz *et al.*, Med. Phys. **31**, 2053 (2004).
4. H.-S. Park, D. M. Chambers, H.-K. Chung, R. J. Clarke, R. Eagleton, E. Giraldez, T. Goldsack, R. Heathcote, N. Izumi, M. H. Key, J. A. King, J. A. Koch, O. L. Landen, A. Nikroo, P. K. Patel, D. F. Price, B. A. Remington, H. F. Robey, R. A. Snavely, D. A. Steinman, R. B. Stephens, C. Stoeckl, M. Storm, M. Tabak, W. Theobald, R. P. J. Town, J. E. Wickersham, and B. B. Zhang, Phys. Plasmas **13**, 056309 (2006).
5. M. Tabak *et al.*, Phys. Plasmas **1**, 1626 (1994).
6. S. D. Baton *et al.*, Phys. Rev. Lett. **91**, 105001 (2003).
7. V. L. Ginzburg, Phys.-Usp. **39**, 973 (1996).
8. J. Zheng *et al.*, Phys. Plasmas **10**, 2994 (2003).
9. J. C. Adam, A. Héron, and G. Laval, Phys. Rev. Lett. **97**, 205006 (2006).
10. W. L. Kruer, *The Physics of Laser Plasma Interactions*, Frontiers in Physics (Westview Press, Boulder, CO, 2003), pp. 39–43.
11. S. C. Wilks *et al.*, Phys. Rev. Lett. **69**, 1383 (1992).
12. H. Popescu *et al.*, Phys. Plasmas **12**, 063106 (2005).
13. M-plan Apo 20×, Mitutoyo, Japan.
14. New Focus, Inc., a division of Brookham, San Jose, CA, 2004, http://www.newfocus.com (14 December 2004).
15. Schott North America, Inc., Elmsford, NY 10523.
16. Semrock, Rochester, NY 14624.
17. Spectral Instruments, Tucson, AZ 85745 (http://www.specinst.com/files/datasheets/4204-.pdf).
18. Luxeon III Star, Philips Lumileds Lighting Company, San Jose, CA 95131.

19. LIP 481R, Heidenhain, 83301 Traunreut, Germany.

20. V. Bagnoud, in *Frontiers in Optics 2004* (Optical Society of America, Rochester, NY, 2004), Paper FMM2.

21. J. H. Kelly, L. J. Waxer, V. Bagnoud, I. A. Begishev, J. Bromage, B. E. Kruschwitz, T. J. Kessler, S. J. Loucks, D. N. Maywar, R. L. McCrory, D. D. Meyerhofer, S. F. B. Morse, J. B. Oliver, A. L. Rigatti, A. W. Schmid, C. Stoeckl, S. Dalton, L. Folnsbee, M. J. Guardalben, R. Jungquist, J. Puth, M. J. Shoup III, D. Weiner, and J. D. Zuegel, J. Phys. IV France **133**, 75 (2006).

22. S. P. Hatchett, C. G. Brown, T. E. Cowan, E. A. Henry, J. S. Johnson, M. H. Key, J. A. Koch, A. B. Langdon, B. F. Lasinski, R. W. Lee, A. J. MacKinnon, D. M. Pennington, M. D. Perry, T. W. Phillips, M. Roth, T. C. Sangster, M. S. Singh, R. A. Snavely, M. A. Stoyer, S. C. Wilks, and K. Yasuike, Phys. Plasmas **7**, 2076 (2000).

23. Lambda900 Spectrophotometer, PerkinElmer, Waltham, MA 02451.

24. J. W. Goodman, *Introduction to Fourier Optics*, 3rd ed. (Roberts and Company Publishers, Englewood, CO, 2005), Chap. 6, p. 127.

25. B. Tatian, J. Opt. Soc. Am. **55**, 1014 (1965).

26. L. Gremillet, G. Bonnaud, and F. Amiranoff, Phys. Plasmas **9**, 941 (2002).

Performance of Direct-Drive Cryogenic Targets on OMEGA

Introduction

In the inertial confinement fusion (ICF) approach to fusion, a spherical shell filled with a deuterium–tritium (DT) mixture is compressed to reach a temperature of 10 to 12 keV in the lower-density central core region (hot spot) to initiate a burn wave through the higher-density colder main fuel surrounding the core.[1–3] The main fuel areal density (ρR) at that time must be large enough to burn a significant fraction of the fuel.[1,2] The peak areal density depends mainly on the fuel adiabat (defined as a ratio of the shell pressure to the Fermi-degenerate pressure at the shell density) and laser energy:[4]

$$(\rho R)_{\max} = \frac{2.6}{\alpha^{0.54}} E_{\mathrm{MJ}}^{1/3}. \tag{1}$$

To study the physics of low-adiabat, high-compression fuel assembly, a series of experiments with cryogenic D_2 and DT fuel was designed and performed on OMEGA.[5] Figure 113.16 summarizes the experimental results reported earlier.[6,7] The targets used in these experiments were D_2-filled CD shells with an outer diameter of ~860 μm, a shell thickness of 3 to 5 μm, and a cryogenic layer thickness between 92 and 98 μm. The targets were driven with shaped laser pulses at peak intensities of 6 to 10 × 10^{14} W/cm^2 to set the fuel adiabat at α = 2 to 25. Figure 113.16 compares the experimental areal density $\langle \rho R \rangle_{\mathrm{exp}}$ inferred from the energy loss of the secondary protons[8] while they propagate through the compressed fuel and the simulated areal density $\langle \rho R \rangle_{\text{1-D}}$ averaged over the 1-D neutron-production history calculated using the hydrocode *LILAC*.[9] The constant flux-limiter thermal conduction model[10] with f = 0.06 was used in such simulations. As seen in the figure, the experimental data significantly deviate from simulation results for the implosions with a mid-to-low designed adiabat when the predicted $\langle \rho R \rangle_{\text{1-D}} > 100$ mg/cm^2. The goal of the current study presented here is to identify the main sources of the measured $\langle \rho R \rangle$ deviation from the theoretical predictions. Equation (1) is used for guidance in this study. According to this equation, the observed degradation in the areal density comes from the underestimation of the predicted adiabat.

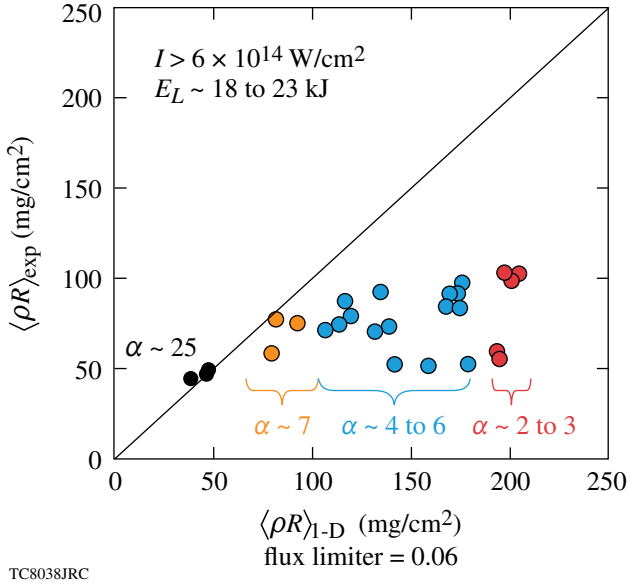

Figure 113.16
Measured neutron-averaged areal density $\langle \rho R \rangle$ as a function of the simulated value using the hydrocode *LILAC*, which uses a thermal conduction model with a constant flux limiter. The drive intensities were above 6 × 10^{14} W/cm^2 and the laser energy varied from 18 to 23 kJ.

In this article we consider several sources for the adiabat degradation during the implosion, including the shock heating and the preheat due to the suprathermal electrons. Based on the result of this study, target designs were optimized using the improved nonlocal thermal-conduction model implemented in the 1-D hydrodynamic code *LILAC*. High-areal-density[11] cryogenic fuel assembly with $\langle \rho R \rangle > 200$ mg/cm^2 has been achieved on OMEGA in designs where the shock timing was optimized and the suprathermal-electron preheat generated by the two-plasmon-decay instability was mitigated. The following sections (1) describe the modeling of the shock heating; (2) consider both the preheat effects due to the suprathermal electrons and the reduction in the measured areal density due to the burn truncation before the peak shell ρR is reached; and (3) present conclusions.

Modeling of Shock Heating

A typical laser pulse for a low-adiabat, direct-drive design consists of a lower-intensity foot (or, as shown in Fig. 113.17,

a picket used in adiabat-shaping designs[12,13] to mitigate the Rayleigh–Taylor instability growth[14]), a transition region, and the higher-intensity main pulse. At the beginning of the pulse, a shock wave (SW) is launched into the shell. Its strength determines the shell adiabat α. The compression wave (CW), initiated as the intensity rises during the transition region, must be properly timed to avoid an excessive adiabat increase at the inner part of the shell. Indeed, if the CW catches the SW too early in the shell, the SW strength increases, raising the adiabat. Delaying the CW, on the other hand, steepens up its front and turns into a shock as the CW travels along the density gradient produced by a rarefaction wave (RW) that is formed after the SW breaks out at the inner surface of the cryogenic layer. To prevent an excessive reduction in the fuel areal density, the coalescence of the RW with the CW must occur within the last 10% of the main fuel mass, as observed in calculations. This condition limits its allowable mistiming of the shock breakout to $\Delta t_s / t_s \le 5\%$ and constrains the modeling accuracy in the absorbed laser energy E_s during the shock propagation. For a constant-intensity foot pulse, the shock-propagation time is $t_s = \Delta_0 / U_s$, where $U_s \sim \sqrt{P_a}$ is the shock speed and Δ_0 is the initial shell thickness. The ablation pressure scales as[1] $p_a \sim P^{2/3}$, where P is the laser power, and writing $E_s \sim P t_s$ gives $t_s \sim \Delta_0^{3/2} E_s^{-1/2}$. The same scaling can be obtained when the shock is launched by a narrow picket. The shock-breakout time in this case[12] is $t_s \sim \left(E_p^{-1/3}\Delta_0\right)^{\beta}$, where $\beta = \left[1 - \sqrt{2\gamma(\gamma-2)}/2(2\gamma-1)\right]^{-1}$, γ is the ratio of specific heats, and t_p and E_p are the picket duration and energy, respectively. For $\gamma > 1.2$, the exponent is $\beta \simeq 3/2$ with less than 10% error, leading to $t_s \sim E_p^{-1/2}$, similar to the case of a constant-intensity pulse. Using $\Delta t_s / t_s < 5\%$, the requirement for the modeling accuracy in the absorbed picket energy becomes $\Delta E_p / E_p < 10\%$.

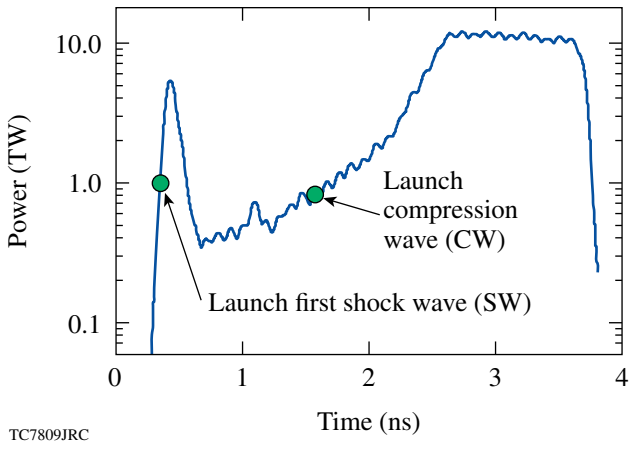

Figure 113.17
A typical pulse shape for the OMEGA direct-drive, low-adiabat design.

Inverse bremsstrahlung is the main absorption mechanism for the $\lambda = 0.351$-μm-wavelength laser irradiation. The absorption fraction depends on the electron-temperature and electron-density profiles.[15] These profiles, in turn, are determined by the thermal conduction near the location of the peak in the laser-energy deposition. Thermal-conduction modeling is crucial, therefore, when calculating the laser-energy deposition. In addition to inverse bremsstrahlung, resonance absorption[15] can be important at early times when the electron density at the critical surface is steep enough for the electric field to tunnel from the laser turning point to the critical density and excite plasma waves. The next two subsections study the contribution of resonance absorption and the effects of nonlocal electron transport to the laser absorption in ICF plasmas.

1. Resonance Absorption Modeling

The effect of resonance absorption was studied for direct-drive–relevant conditions using a numerical solution of the wave equations in planar geometry. The results of these calculations[16] were used to develop a simplified analytical model that can be implemented into hydrodynamic codes to model spherical implosions. The model is based on the approach described in Ref. 15. We consider a p-polarized electromagnetic wave with incident angle θ between the direction of propagation and the density gradient, which points along the z direction. The z component of the electric field E_z tunnels through from the laser turning point to the critical density, depositing a fraction f_A of the incident laser energy into the plasma waves (resonance absorption[15]). Propagating down the density gradient, the energy of these waves is damped into the electrons. Calculations show[16] that the average temperature of the resonance electrons for $\lambda_L = 0.351$-μm-wavelength laser irradiation does not exceed ~5 keV. Resonance absorption, therefore, enhances the local absorption due to the inverse bremsstrahlung. Resonance absorption is calculated by evaluating the energy flux[15] $I_{\text{abs}} = \int_0^{\infty} \nu E_z^2 / 8\pi \mathrm{d}z$, where ν is the damping rate of the plasma waves. The main contribution to this integral comes near the resonance point, in the vicinity of the critical density, resulting in

$$I_{\text{abs}} = \frac{\omega L_n}{8}\left(\sin\theta B_{\text{cr}}\right)^2, \tag{2}$$

where B_{cr} and L_n are the magnetic field and the density scale length at the critical density, respectively. The resonance field is calculated by multiplying the field amplitude at the turning point, $B_t = 0.9\, E_0 \left(c/\omega L_n\right)^{1/6}$, by a tunneling factor.[15] Here, E_0 is the laser field in free space. In deriving B_t the laser-energy absorption in the region below critical density was neglected, leading to an overestimate in the resonance field. Corrected

for this absorption and adding the intensity of the incoming and outgoing waves, $f_t E_0^2$ and $(f_t - f_A)E_0^2$, respectively, the magnetic field becomes $0.9\sqrt{2f_t - f_A}\,E_0(c/\omega L)^{1/6}/2$, where f_t is the fraction of the laser energy that reaches the turning point. Multiplying B_t by the tunneling factor $\exp\left(-\omega/c\int_{z_t}^{z_c}\sqrt{-\epsilon}\,\mathrm{d}z\right)$, we obtain $f_A = \phi^2(2f_t - f_A)/8$ and

$$f_A = \frac{2f_t}{8/\phi^2 + 1}, \tag{3}$$

where $\phi = 2.3\tau\exp\left(-2\tau^3/3\right)$, $\tau = \left(3\omega/2c\int_{z_t}^{z_c}\sqrt{-\epsilon}\,\mathrm{d}z\right)^{1/3}$, $\epsilon = 1 - n/n_{\mathrm{cr}}$ is the dielectric function, n and n_{cr} are the electron and critical densities, respectively, and z_t and z_c are the position of the turning point and critical density, respectively. Since the incident laser light in ICF experiments consists of a mixture of *s* and *p* polarizations, the resonance absorption fraction in a hydrocode simulation is taken as a half value predicted by Eq. (3). Simulations show that Eq. (3) agrees very well with the results of more rigorous calculations.[16]

The tunneling factor depends on the density scale length at the critical surface. Thus, an accurate calculation of both the inverse bremsstrahlung and resonance absorption relies on thermal transport modeling, which affects hydrodynamic profiles in the energy-deposition region. The next subsection discusses electron thermal transport in laser-produced plasmas.

2. Heat-Transport Modeling

Because of the steep temperature and density profiles where the laser deposition is at maximum, the validity of Spitzer thermal conduction[17] breaks down (the mean free path of the heat-carrying electrons is comparable to or larger than the temperature scale length). In a model using flux limitation,[10] the thermal flux is calculated as a fraction f of the free-stream flux $q_{\mathrm{fs}} = nTv_T$, when the Spitzer heat flux $q_{\mathrm{sp}} > fq_{\mathrm{fs}}$. Here, $v_T = \sqrt{T/m}$ is the electron thermal velocity and m, T, and n are the electron mass, temperature, and free electron density, respectively. Since the flux-limiter value f cannot be determined directly from the physical principles, its value, usually taken to be a constant in time, is obtained by comparing the simulation results with experimental observables. Remarkably, such a simple model is able to successfully explain a large number of experiments with simple pulse shapes. However, for the shaped, low-adiabat pulses, the flux limiter, as first shown in the Fokker–Planck simulations,[18] must be time dependent. The time dependence is especially important in simulating the adiabat-shaping designs,[12,13] where a narrow picket is introduced at the beginning of the laser pulse to tailor the shell adiabat and mitigate the Rayleigh–Taylor instability growth.[14] Accurate accounting for the absorbed picket energy as well as for the laser coupling during the transition region (see Fig. 113.17) is crucial for the shock-timing calculation. Since it is highly impractical to obtain the temporal shape of the flux limiter based only on the experimental data, a thermal-transport model must be developed for self-consistent flux calculations. Such a model was proposed in Ref. 19, where the simplified Boltzmann equation was solved using the Krook approximation.[20] The main disadvantage of such a model is the lack of particle and energy conservation because of the energy-dependent collisional frequency. Calculations show that, for the conditions relevant to ICF experiments, the error in calculating the local electron density and energy using the solution of the model described in Ref. 19 does not exceed 5%. Despite the fact that the error is small, the model used in the present calculations is modified to recover the conservation properties. This is accomplished by renormalizing the local density and temperature used in evaluating the symmetric part of the electron-distribution function. Similar modifications appear in the classical limit when the ratio of the electron mean-free path λ_{ei} to the temperature scale length L_T is small.[21] The second-order deviations from the Maxwellian f_{M}, $f_{\mathrm{sym}} = f_{\mathrm{M}} + f_n + v^2 f_T$, where $f_{n,T} \sim O\left[(\lambda_{\mathrm{ei}}/L_T)^2\right]$, are due in such a limit to the contribution from the electron–electron collisions.[21] These corrections are equivalent to the renormalization in the electron density and temperature used in the local Maxwellian distribution, $f_{\mathrm{sym}} = f_{\mathrm{M}}(n', T')$. Next, we describe the renormalization procedure used in the present nonlocal model.

The Boltzmann equation with the Krook collisional operator[20] $v_x\,\partial_x f + (eE_x/m)\,\partial_v f = -\nu_{\mathrm{ei}}(v)(f - f_0)$ can be solved analytically by substituting f_0 into the second term of the left-hand side:[19]

$$\begin{aligned} f &= f_0 - \int^x G(x', v)e^{\xi/y}\,\mathrm{d}\xi, \\ G &= \lambda_{\mathrm{ei}}(x')\left(\frac{\partial f_0}{\partial x} + \frac{eE_x}{T}\frac{\partial f_0}{\partial \epsilon}\right), \end{aligned} \tag{4}$$

where

$$\xi(x') = \int_x^{x'} \mathrm{d}x''/\lambda_{\mathrm{ei}}(x''),$$

$\epsilon = mv^2/2T$, $y = \cos\theta$, $\lambda_{\mathrm{ei}} = v/\nu_{\mathrm{ei}}$, $\nu_{\mathrm{ei}} \sim v^{-3}$ is the electron–ion collisional frequency, and E_x is the slowly varying electric field. Assuming that f_0 is a function of the renormalized density n' and temperature T', the relations between (n', T') and (n, T) are found by integrating Eq. (4), multiplied by 1 and $mv^2/2$, yielding $n = n' - R_1$ and $3nT/2 = 3n'T'/2 - R_2$, respectively, where

$$R_1 = 2\pi \int_0^\infty \mathrm{d}v v^2 \int_0^1 \mathrm{d}y \left(H_L - H_R\right),$$

$$R_2 = \pi m \int_0^\infty \mathrm{d}v v^4 \int_0^1 \mathrm{d}y \left(H_L - H_R\right),$$

$$H_L = \int_{x_L}^{x} G e^{\xi/y} \mathrm{d}\xi,$$

and

$$H_R = \int_{x}^{x_R} G e^{-\xi/y} \mathrm{d}\xi.$$

The integration limits are defined as

$$\int_{x}^{\{x_R, x_L\}} \mathrm{d}x'' / \lambda_{\mathrm{ei}} = \{+, -\}\infty.$$

The electric current and the heat flux are calculated using the standard definitions $j_x = e\int \mathrm{d}^3 v v_x f$ and $q_x = m\int \mathrm{d}^3 v v^2 v_x f/2$. The electric field E_x is defined by the zero-current condition $j_x = 0$. This condition yields an integral equation for E_x, which is solved by the iteration method.[19] For the distribution function f_0, we use the Maxwellian function with the corrections due to the laser field[22] $f_0 = f_M \exp\left(-0.07\,\alpha_L \epsilon^{5/2}\right)$, where $\alpha_L = Z v_e^2 / v_T^2$, Z is the average ion charge, and v_e and $v_T = \sqrt{T/m}$ are the electron quiver and thermal velocities, respectively.

Two main effects are introduced by the nonlocal treatment of the thermal transport: First, the flux is reduced from the Spitzer value in the regions with steep temperature gradients; second, the main fuel is heated by the long-range electrons from the hotter plasma corona. The heat flux calculated using the distribution function in Eq. (4) does not correctly reproduce the nonlocal heating because the integrand in Eq. (4) does not go to zero at $\int_{x'}^{x} \mathrm{d}x'' / \lambda_E = 1$, where λ_E is the electron-deposition range. Since the calculations must accurately account for every preheat source, it is essential to include a deposition cutoff. In the previous version of the nonlocal model,[19] this was accomplished by replacing the exponential kernel $e^{\xi/y}$ in Eq. (4) with $\sqrt{1 - \xi/y}$. Such a substitution, however, does not properly recover the Spitzer limit. In the current version of the model, a test-particle approximation is used in evaluating λ_{ei} to produce the deposition cutoff. This approach gives Spitzer conductivity when $\lambda_{\mathrm{ei}} / L_T \ll 1$. In the test-particle approximation, λ_{ei} is calculated along the particle trajectory using the energy-loss equation $\mathrm{d}K/\mathrm{d}s = -K/2\,\lambda_E$. Since $\lambda_E \sim K^2$, we obtain

$$K = K_0 \sqrt{1 - \int_{x'}^{x} \mathrm{d}x'' / y\lambda_E},$$

where $\mathrm{d}s = \mathrm{d}x/y$ is a path element. Then, the deposition cutoff is introduced in Eq. (4) by replacing $\lambda_{\mathrm{ei}}(x')$ with

$$\lambda_{\mathrm{ei}}(x', x) = \lambda_{\mathrm{ei}}(x') \left(1 - \int_{x'}^{x} \mathrm{d}x' / y\lambda_E\right).$$

Next, we compare the results obtained using the described nonlocal model with simulations based on the flux-limited Spitzer conduction. Figure 113.18 shows the effective flux limiter (defined as a maximum ratio of the nonlocal heat flux to the free-stream flux q_{fs} in the vicinity of maximum q_{sp} in the plasma corona) as a function of time for an $\alpha = 2$ cryogenic implosion. The higher value of the flux limiter during the picket indicates a larger predicted laser absorption and a stronger SW, relative to calculations based on the constant flux-limiter model. Then, as the laser intensity relaxes after the picket, the effective flux limiter takes on a reduced value, leading to a weaker CW. If these effects are not properly modeled in a simulation, they lead to a significant shock mistiming and areal-density reduction.

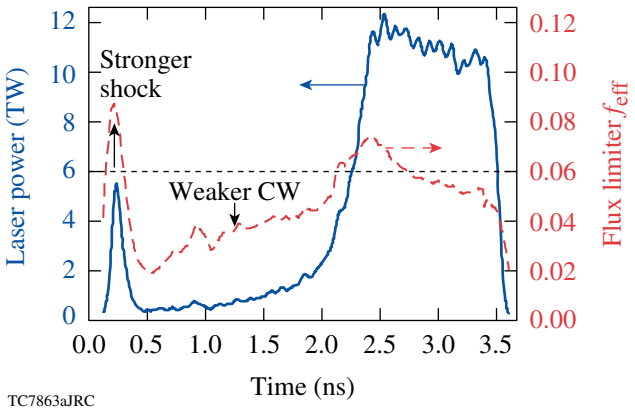

Figure 113.18
Laser pulse (solid line, left axis) and the effective flux limiter f_{eff} (dashed line, right axis) obtained using the nonlocal model for an $\alpha = 2$ cryogenic OMEGA design with a 95-μm-thick D_2 layer and a 10-μm-thick CD overcoat. The thin dashed line shows standard values of the flux limiter used in the hydrocode *LILAC*.

To test the accuracy of the absorption calculations with the nonlocal transport model, the simulation results were compared with experimental absorption data[23] for implosions of 20-μm-thick plastic shells driven with a 200-ps Gaussian pulse at peak intensities varied from 5×10^{13} to 1.5×10^{15} W/cm^2. Figure 113.19 shows the laser absorption fraction calculated using the flux-limited transport model with $f = 0.06$ and no resonance absorption (open squares), the flux-limited model with resonance absorption (solid squares), and the nonlocal model with resonance absorption (triangles). The resonance absorption

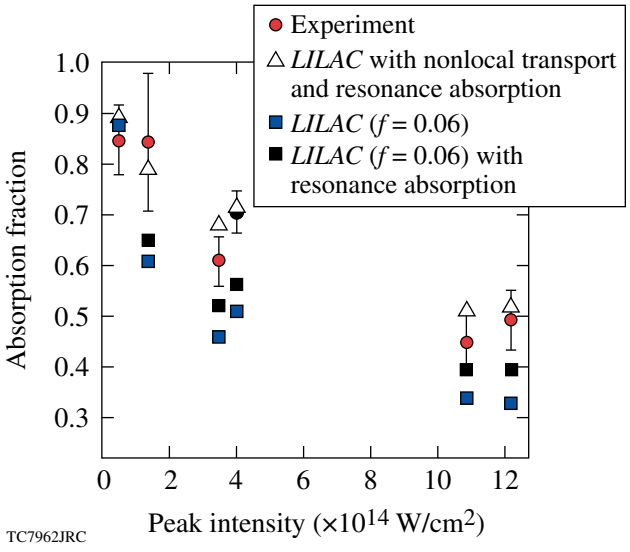

Figure 113.19
Absorption fraction of the incident laser energy for a 20-μm-thick CH shell driven by a 200-ps Gaussian pulse at different peak intensities.

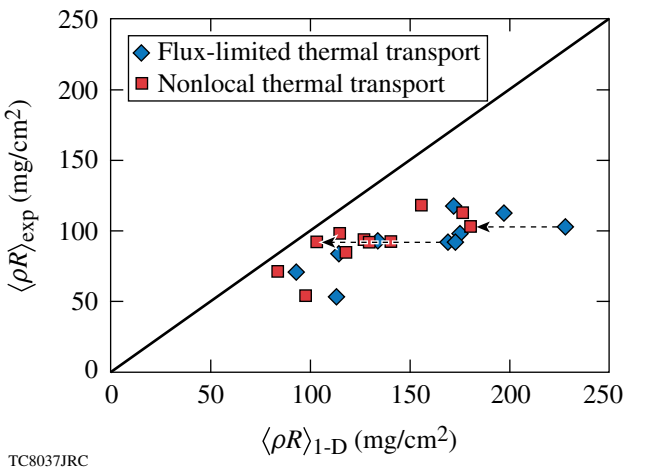

Figure 113.20
Measured $\langle \rho R \rangle$ in a thin CD cryogenic shell as a function of the simulated value using the hydrocode *LILAC* with a constant flux limiter f = 0.06 (diamonds) and the nonlocal (squares) thermal conduction models. Arrows indicate reduction in calculated $\langle \rho R \rangle$ when the nonlocal model is used.

effects are small when the nonlocal thermal-transport model is used. These results, therefore, are not shown in Fig. 113.19. The flux-limited transport model produces much steeper electron-density profiles near the laser turning point, resulting in larger resonance absorption in comparison with the nonlocal model calculations. However, even with resonance absorption taken into account, the flux-limited model underestimates the laser absorption fraction for most of the cases shown in Fig. 113.19. The nonlocal model, on the other hand, reproduces the experimental results very well. The non-monotonic behavior of the absorption fraction with peak intensity is due to shot-to-shot variations in the picket width and the rate of intensity rise.

Next, the areal densities for the cryogenic implosions shown in Fig. 113.16 were recalculated using the nonlocal thermal-transport model. The data are plotted in Fig. 113.20. The improved agreement with the experimental data is due to a reduction in the calculated areal density, resulting from significant shock mistiming predicted by the nonlocal model (see arrows in Fig. 113.20 showing this reduction for individual shots). Even though the calculations with the nonlocal model are in better agreement with the experimental data, some discrepancy still remains. In the next section we examine possible sources for the remaining discrepancy, starting with suprathermal-electron preheat.

Suprathermal-Electron Preheat and ρR Sampling

Several laser–plasma interaction processes are capable of generating suprathermal electrons in the plasma corona. As discussed in the **Introduction** (p. 16), the degradation in ρR is significant if the adiabat at the inner part of the shell is increased. The electron preheat is important, therefore, if the electron-deposition ranges exceed the thickness of the cold part of the shell during the implosion. Thus, for the OMEGA designs, only electrons with energy in excess of 50 keV can reduce the peak shell compression. To estimate the amount of the energy deposited in the shell required to degrade the fuel areal density, we use the pressure–density relation[1] $p \sim \alpha \rho^{5/3}$ and assume the ideal gas equation of state. This gives $\alpha \sim T^{5/3} / p^{2/3}$. The shell pressure is proportional to the ablation pressure p_a, which is determined by the laser intensity. Therefore, for a given drive intensity, according to Eq. (1), $\rho R = (\rho R)_0 / (T/T_0)^{0.09}$, where $(\rho R)_0$ and T_0 are the areal density and electron temperature without the effects of preheat. The shell temperature during the acceleration phase in a typical low-adiabat design is ~20 eV. A 20% reduction in the areal density corresponds to a 6-eV increase in the shell temperature. For an OMEGA target, this leads to ~10 J of preheat energy deposited into the unablated part of the shell. The lowest-threshold mechanism capable of producing energetic electrons with $T_{hot} > 50$ keV is the two-plasmon-decay instability.[15] The threshold parameter η for this instability[24] is

$$\eta = \frac{I_{14} L_n(\mu\text{m})}{230\, T_{\text{keV}}} \frac{\lambda_L}{0.351\ \mu\text{m}}, \tag{5}$$

where I_{14} is the laser intensity in units of 10^{14} W/cm^2, L_n is the density scale length, and λ_L is the laser wavelength. The instability develops when $\eta > 1$. For a typical OMEGA implosion, $L_n \sim$

150 μm and $T_{keV} \sim 1$ at $I_{14} \sim 1$. Thus, the instability is expected to develop when the drive intensity exceeds a few 10^{14} W/cm^2.

The experimental signature of the suprathermal-electron preheat is the measured hard x-ray[25] signal. This correlates with the $3/2\omega$ signal,[23] indicating that the two-plasmon-decay instability is the main mechanism producing the energetic electrons. The hard x-ray signal measured in cryogenic implosions, shown in Fig. 113.21, increases with the laser intensity.[26] Taking this result into account, the peak drive intensity was reduced to below 3×10^{14} W/cm^2 to minimize the suprathermal-electron-preheat effect on the target performance.[26] The measured and predicted areal densities, together with the data for $I > 5 \times 10^{14}$ W/cm^2, are plotted on Fig. 113.22. The improved agreement observed for the lower-intensity shots suggests that suprathermal-electron preheat contributes to a modest degradation in ρR at higher drive intensities.

As the next step, the peak drive intensity was raised to 5×10^{14} and the CD overcoat thickness was increased from 5 to 10 μm. The thicker plastic shell was used to prevent the laser from burning through the plastic to the deuterium during the target implosion and thus mitigate the suprathermal-electron preheat at higher intensity. If the higher-Z plastic burns through during the pulse, as in the case of a 5-μm-thick shell, lower-Z D_2 penetrates into the subcritical-density region, reducing the laser absorption. This in turn leads to a drop in the coronal temperature and an increase in the laser intensity at the quarter-critical surface. All of these factors raise the value of η, exciting the two-plasmon-decay instability at the time when the CD layer burns through. Increasing the CD overcoat thickness to 10 μm allowed the drive intensity to be raised to 5×10^{14} W/cm^2. This produced a significantly less amount of the hard x-ray signal compared to the thinner plastic shell, indicating lower suprathermal preheat. The stars in Fig. 113.22 show the high areal densities (up to 202±7 mg/cm^2) measured in the implosions, which are described in greater detail in Ref. 11. Despite the small hard x-ray signal, the measured areal densities were ~18% lower than the 1-D prediction, indicating that additional mechanisms could be responsible for the measured ρR deviation from the predicted value.

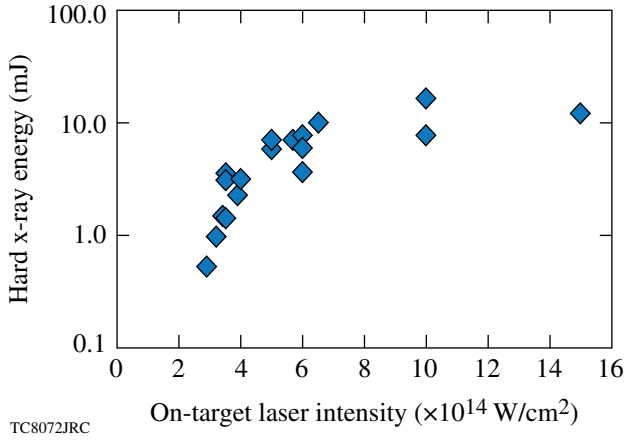

Figure 113.21
Measured bremsstrahlung radiation above 40 keV for the thin-CD-shell cryogenic implosions. The inferred hard x-ray temperature in these implosions is above 50 keV.

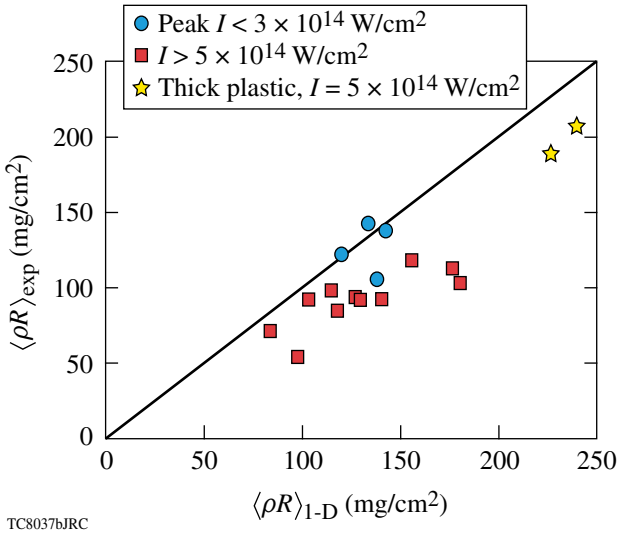

Figure 113.22
Measured $\langle \rho R \rangle$ as a function of the simulated value using the hydrocode *LILAC* with the nonlocal transport model for cryogenic implosions at peak intensities $I > 5 \times 10^{14}$ W/cm^2 (squares) and $I < 3 \times 10^{14}$ W/cm^2 (circles), and for a 10-μm-thick CD shell at $I = 5 \times 10^{14}$ W/cm^2 (stars).

The areal density in the experiment is inferred from the energy downshift in the secondary protons created in the D^3He reaction.[8] The experimentally inferred $\langle \rho R \rangle$, therefore, is affected by the timing of the production of these protons with respect to the ρR temporal evolution. Shown in Fig. 113.23(a) are the experimental and predicted neutron-production histories for a cryogenic implosion with a 10-μm-thick CD overcoat that yielded the highest $\langle \rho R \rangle_{exp}$. The predicted areal-density history is plotted on the same figure. The figure shows that the experimental burn rate is significantly reduced (presumably by the perturbation growth during the shell deceleration) at the time when the shell ρR reaches its peak value.[27] This could explain the lower measured areal density with respect to the results of 1-D calculations [compare solid (measurement) and dotted (calculation) curves in Fig. 113.23(a)]. To address the

sampling issue, Fig. 113.23(b) plots the predicted D^3He proton spectrum averaged over the experimental burn history (dashed curve), showing good agreement with the measured spectrum (solid curve) averaged over five individual measurements at different views of the implosion.

The suprathermal-electron–generation efficiency for the NIF-scaled targets, not fully understood at present time, is currently under investigation. Preliminary experiments have been carried out to study the preheat mitigation by doping the outer layer of the ablator with high-Z elements. In these experiments, warm plastic shells filled with 15 atm of D_2 gas were imploded using two pulse shapes to set the shell adiabat to $\alpha = 2$ and 3, respectively. The outer 3 μm to 10 μm of the shell were doped with 6%/atom of Si or 2% to 2.6%/atom of Ge. The total shell thickness was 27 μm. The increased laser absorption caused by the higher averaged ion charge in the plasma corona is predicted to raise the threshold for the two-plasmon-decay instability [see Eq. (5)], reducing the suprathermal-electron preheat. Figure 113.24 shows the hard x-ray signal measured

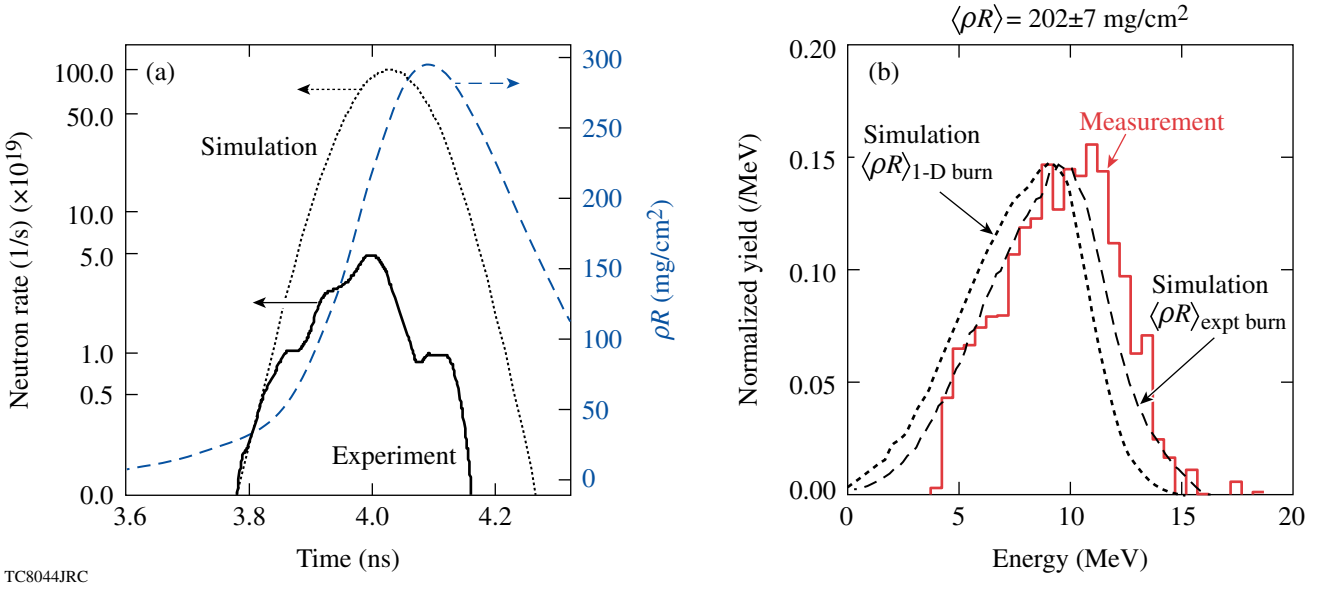

Figure 113.23
(a) The burn history measured (solid line) and predicted (dotted line). Also shown is the ρR evolution calculated with the 1-D code *LILAC* (dashed line, right axis). (b) Measured secondary-proton spectrum (solid line) for a 10-μm-thick CD shell with a 95-μm-thick D_2 cryogenic layer driven on an $\alpha = 2$ adiabat at $I = 5 \times 10^{14}$ W/cm^2. The dotted line shows the calculated spectrum averaged over the predicted 1-D burn, and the dashed line represents the calculated spectrum averaged over the experimental burn history.

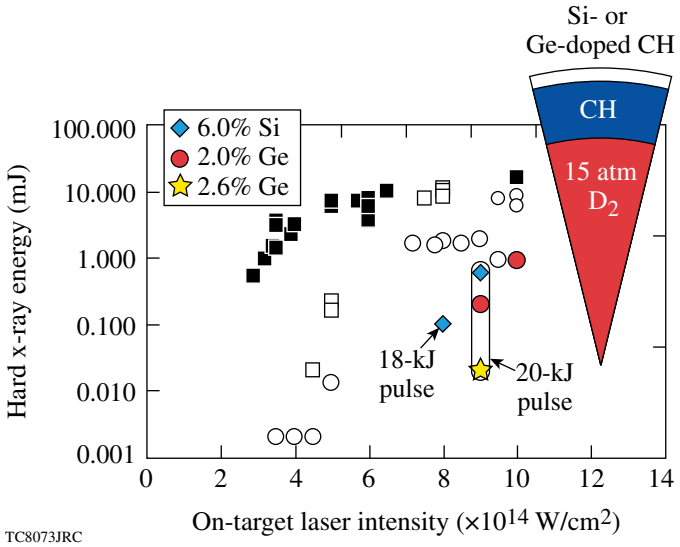

Figure 113.24
Measured bremsstrahlung radiation above 40 keV for the implosions with warm plastic (open circles), doped plastic (diamond, solid circle, and star), cryogenic 5-μm-thick CD (solid squares), and cryogenic 10-μm-thick CD (open squares) shells.

in pure-CH and CH shells doped with Si or Ge. The observed significant reduction in the signal level confirms the lower preheat level in the doped ablators. For comparison, Fig. 113.24 also shows the signal for cryogenic targets with 5- and 10-μm-thick CD shells.

In addition to the reduction in the hard x-ray signal, the shells with Si-doped layers show improved hydrodynamic stability. The radiation from the higher-Z dopant preheats the shell, reducing both the initial imprint levels[28,29] and the Rayleigh–Taylor instability growth. The improved stability of Si-doped shells with respect to the pure-CH shells results in an increase in both the experimental yields and the ratio of the experimental to the predicted yield. The latter is shown in Fig. 113.25. The increased yield is especially pronounced in the most-unstable, $\alpha = 2$ implosions when the thickness of the doped layer is 3 μm or greater. The stabilizing property of the high-Z dopants will be used in the future OMEGA cryogenic designs. Calculations show that the radiation from the dopant preferably preheats the higher-opacity CD layer without significantly heating the lower-opacity main fuel. This enhances cryogenic shell stability without compromising the fuel adiabat.

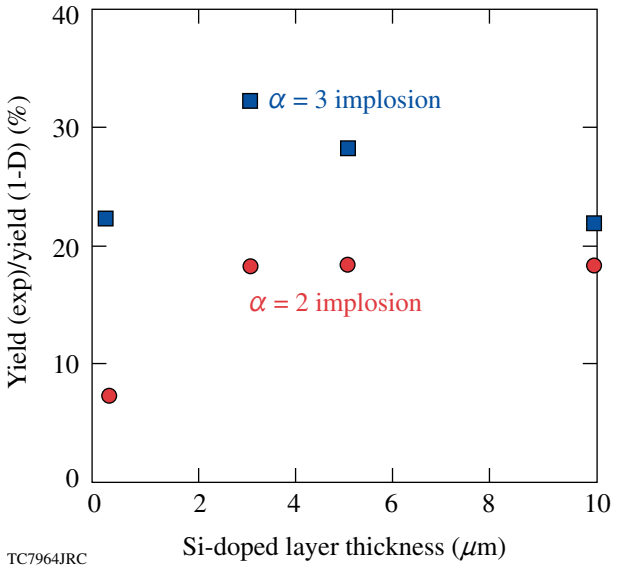

Figure 113.25
Ratio of the experimental yield and the predicted yield for warm-plastic-shell implosions with different Si-doped layer thicknesses.

Conclusions

Ignition target designs rely on low-adiabat, high-areal-density fuel compression. A series of implosions with 92- to 95-μm-thick cryogenic D_2 layers were performed on OMEGA to study the physics of ignition-relevant, low-adiabat fuel assembly using the direct-drive configuration. The main sources of the adiabat degradation, observed in earlier experiments,[6,7] were attributed to (1) the shock mistiming resulting from inaccuracies in the laser-absorption modeling, (2) suprathermal-electron preheat generated by the two-plasmon-decay instability, and (3) under-sampling of higher ρR in the shell due to burn truncation. To increase the calculation accuracy, the nonlocal transport model was implemented in the 1-D hydrocode *LILAC*. High cryogenic areal density with $\langle \rho R \rangle > 200$ mg/cm^2 was measured in the experiments[11] when the shock timing was optimized using the nonlocal treatment of the heat transport and the suprathermal-electron-preheat source was mitigated.

ACKNOWLEDGMENT

This work was supported by the U.S. Department of Energy Office of Inertial Confinement Fusion under Cooperative Agreement No. DE-FC52-08NA28302, the University of Rochester, and the New York State Energy Research and Development Authority. The support of DOE does not constitute an endorsement by DOE of the views expressed in this article.

REFERENCES

1. S. Atzeni and J. Meyer-ter-Vehn, *The Physics of Inertial Fusion: Beam Plasma Interaction, Hydrodynamics, Hot Dense Matter*, International Series of Monographs on Physics (Clarendon Press, Oxford, 2004).

2. J. D. Lindl, *Inertial Confinement Fusion: The Quest for Ignition and Energy Gain Using Indirect Drive* (Springer-Verlag, New York, 1998).

3. S. E. Bodner, D. G. Colombant, J. H. Gardner, R. H. Lehmberg, S. P. Obenschain, L. Phillips, A. J. Schmitt, J. D. Sethian, R. L. McCrory, W. Seka, C. P. Verdon, J. P. Knauer, B. B. Afeyan, and H. T. Powell, Phys. Plasmas **5**, 1901 (1998).

4. R. Betti and C. Zhou, Phys. Plasmas **12**, 110702 (2005).

5. T. R. Boehly, D. L. Brown, R. S. Craxton, R. L. Keck, J. P. Knauer, J. H. Kelly, T. J. Kessler, S. A. Kumpan, S. J. Loucks, S. A. Letzring, F. J. Marshall, R. L. McCrory, S. F. B. Morse, W. Seka, J. M. Soures, and C. P. Verdon, Opt. Commun. **133**, 495 (1997).

6. F. J. Marshall, R. S. Craxton, J. A. Delettrez, D. H. Edgell, L. M. Elasky, R. Epstein, V. Yu. Glebov, V. N. Goncharov, D. R. Harding, R. Janezic, R. L. Keck, J. D. Kilkenny, J. P. Knauer, S. J. Loucks, L. D. Lund, R. L. McCrory, P. W. McKenty, D. D. Meyerhofer, P. B. Radha, S. P. Regan, T. C. Sangster, W. Seka, V. A. Smalyuk, J. M. Soures, C. Stoeckl, S. Skupsky, J. A. Frenje, C. K. Li, R. D. Petrasso, and F. H. Séguin, Phys. Plasmas **12**, 056302 (2005).

7. T. C. Sangster, R. Betti, R. S. Craxton, J. A. Delettrez, D. H. Edgell, L. M. Elasky, V. Yu. Glebov, V. N. Goncharov, D. R. Harding, D. Jacobs-Perkins, R. Janezic, R. L. Keck, J. P. Knauer, S. J. Loucks, L. D. Lund, F. J. Marshall, R. L. McCrory, P. W. McKenty, D. D. Meyerhofer, P. B. Radha, S. P. Regan, W. Seka, W. T. Shmayda, S. Skupsky, V. A. Smalyuk, J. M. Soures, C. Stoeckl, B. Yaakobi, J. A. Frenje, C. K. Li, R. D. Petrasso, F. H. Séguin, J. D. Moody, J. A. Atherton, B. D. MacGowan, J. D. Kilkenny, T. P. Bernat, and D. S. Montgomery, Phys. Plasmas **14**, 058101 (2007).

8. F. H. Séguin, C. K. Li, J. A. Frenje, D. G. Hicks, K. M. Green, S. Kurebayashi, R. D. Petrasso, J. M. Soures, D. D. Meyerhofer, V. Yu. Glebov, P. B. Radha, C. Stoeckl, S. Roberts, C. Sorce, T. C. Sangster, M. D. Cable, K. Fletcher, and S. Padalino, Phys. Plasmas **9**, 2725 (2002).

9. J. Delettrez, R. Epstein, M. C. Richardson, P. A. Jaanimagi, and B. L. Henke, Phys. Rev. A **36**, 3926 (1987).

10. R. C. Malone, R. L. McCrory, and R. L. Morse, Phys. Rev. Lett. **34**, 721 (1975).

11. T. C. Sangster, V. N. Goncharov, P. B. Radha, V. A. Smalyuk, R. Betti, R. S. Craxton, J. A. Delettrez, D. H. Edgell, V. Yu. Glebov, D. R. Harding, D. Jacobs-Perkins, J. P. Knauer, F. J. Marshall, R. L. McCrory, P. W. McKenty, D. D. Meyerhofer, S. P. Regan, W. Seka, R. W. Short, S. Skupsky, J. M. Soures, C. Stoeckl, B. Yaakobi, D. Shvarts, J. A. Frenje, C. K. Li, R. D. Petrasso, and F. H. Séguin, "High-Areal-Density Fuel Assembly in Direct-Drive Cryogenic Implosions," submitted to Physical Review Letters.

12. V. N. Goncharov, J. P. Knauer, P. W. McKenty, P. B. Radha, T. C. Sangster, S. Skupsky, R. Betti, R. L. McCrory, and D. D. Meyerhofer, Phys. Plasmas **10**, 1906 (2003).

13. K. Anderson and R. Betti, Phys. Plasmas **11**, 5 (2004).

14. S. Chandrasekhar, in *Hydrodynamic and Hydromagnetic Stability*, International Series of Monographs on Physics (Clarendon Press, Oxford, 1961), p. 428.

15. W. L. Kruer, *The Physics of Laser–Plasma Interactions*, Frontiers in Physics, Vol. 73, edited by D. Pines (Addison-Wesley, Redwood City, CA, 1988), Chap. 4, p. 39.

16. I. V. Igumenshchev, V. N. Goncharov, W. Seka, D. Edgell, and T. R. Boehly, Phys. Plasmas **14**, 092701 (2007).

17. L. Spitzer, Jr. and R. Härm, Phys. Rev. **89**, 977 (1953).

18. A. Sunahara, J. A. Delettrez, C. Stoeckl, R. W. Short, and S. Skupsky, Phys. Rev. Lett. **91**, 095003 (2003).

19. V. N. Goncharov, O. V. Gotchev, E. Vianello, T. R. Boehly, J. P. Knauer, P. W. McKenty, P. B. Radha, S. P. Regan, T. C. Sangster, S. Skupsky, V. A. Smalyuk, R. Betti, R. L. McCrory, D. D. Meyerhofer, and C. Cherfils-Clérouin, Phys. Plasmas **13**, 012702 (2006).

20. N. A. Krall and A. W. Trivelpiece, *Principles of Plasma Physics* (San Francisco Press, Inc., San Francisco, 1986), p. 316.

21. A. V. Maksimov, V. P. Silin, and M. V. Chegotov, Sov. J. Plasma Phys. **16**, 331 (1990).

22. V. N. Goncharov and G. Li, Phys. Plasmas **11**, 5680 (2004).

23. W. Seka, D. H. Edgell, J. P. Knauer, J. F. Myatt, A. V. Maximov, R. W. Short, T. C. Sangster, R. E. Bahr, R. S. Craxton, J. A. Delettrez, V. N. Goncharov, I. V. Igumenshchev, and D. Shvarts, "Time-Resolved Absorption in Cryogenic and Room-Temperature, Direct-Drive Implosions," submitted to Phys. Plasmas (invited).

24. A. Simon, R. W. Short, E. A. Williams, and T. Dewandre, Phys. Fluids **26**, 3107 (1983).

25. C. Stoeckl, V. Yu. Glebov, D. D. Meyerhofer, W. Seka, B. Yaakobi, R. P. J. Town, and J. D. Zuegel, Rev. Sci. Instrum. **72**, 1197 (2001).

26. V. A. Smalyuk, D. Shvarts, R. Betti, J. A. Delettrez, D. H. Edgell, V. Yu. Glebov, V. N. Goncharov, R. L. McCrory, D. D. Meyerhofer, P. B. Radha, S. P. Regan, T. C. Sangster, W. Seka, S. Skupsky, C. Stoeckl, B. Yaakobi, J. A. Frenje, C. K. Li, R. D. Petrasso, and F. H. Séguin, "The Role of Hot-Electron Preheat in the Compression of Direct-Drive Imploding Targets with Cryogenic D_2 Ablators," submitted to Physical Review Letters.

27. P. B. Radha, V. N. Goncharov, T. J. B. Collins, J. A. Delettrez, Y. Elbaz, V. Yu. Glebov, R. L. Keck, D. E. Keller, J. P. Knauer, J. A. Marozas, F. J. Marshall, P. W. McKenty, D. D. Meyerhofer, S. P. Regan, T. C. Sangster, D. Shvarts, S. Skupsky, Y. Srebro, R. P. J. Town, and C. Stoeckl, Phys. Plasmas **12**, 032702 (2005).

28. M. Karasik *et al.*, Bull. Am. Phys. Soc. **49**, 276 (2004).

29. A. N. Mostovych, D. G. Colombant, M. Karasik, J. P. Knauer, A. J. Schmitt, and J. L. Weaver, "Enhanced Direct-Drive Implosion with Thin High-*Z* Ablation Layers," to be published in Physical Review Letters.

Initial Experiments on the Shock-Ignition Inertial Confinement Fusion Concept

Introduction

Shock ignition is a concept for direct-drive laser inertial confinement fusion (ICF)[1–3] that was recently proposed by Betti *et al.*[4,5] It promises to achieve ignition with ~3×-lower driver energy than the conventional isobaric hot-spot ignition concept.[6] The fuel is assembled to a high areal density (ρR) on a low adiabat (α) with a sub-ignition implosion velocity using shaped nanosecond laser pulses. The adiabat[3] is defined as the ratio of the plasma pressure to the Fermi pressure of a degenerate electron gas and is typically $\alpha \sim 1$ to 2. Because of the low implosion velocity, the temperature of the central hot spot is too low for conventional ignition to occur. A strong shock wave launched at the end of the laser pulse with an intensity spike hits the compressed core, further compresses the hot spot, and triggers ignition. The resulting burn wave ignites the entire dense core, producing high yields due to the large areal densities. Similar to fast ignition[7] and impact ignition,[8] the fuel assembly and ignition are separated and the energy gain (G) scales as $G \sim \theta \big/ v_i^{1.25}$ (Ref. 9), where θ is the burnup fraction that increases with ρR (Ref. 2) and v_i denotes the implosion velocity. A low implosion velocity and high ρR are advantageous to producing the highest ICF gains.[4] The peak areal density is approximately independent of the shell's implosion velocity and depends on the in-flight adiabat according to $(\rho R)_{\max} \sim \alpha^{-0.6}$ (Ref. 4), favoring as low an adiabat as achievable. Low-velocity, high-ρR, $\alpha \approx 1.5$ implosions have recently demonstrated experimentally a neutron-averaged areal density of 0.13 g/cm^2 and peak ρR of ~0.24 g/cm^2 (Ref. 10). In fast ignition, the implosion laser facility must be combined with a high-intensity, short-pulse, multipetawatt-ignitor laser facility delivering a particle beam for ignition. Shock ignition makes use of the pulse-shaping capabilities of the implosion laser facility, significantly relaxing the technical constraints on the concept.

The strong shock wave that triggers ignition is achieved by adding a sharp intensity spike at the end of the main drive pulse.[4] The laser power must rise to several hundred terawatts in a few hundred picoseconds to drive the ignitor shock. The spike pulse is timed so that the shock wave meets with the return shock driven by the rising hot-spot pressure during the deceleration phase in the shell close to the cold fuel/hot spot interface. The colliding shocks generate two new shock waves with one propagating inward, leading to further compression of the hot spot and a peaked pressure profile with its maximum in the center. The resulting fuel assembly is nonisobaric with a hot-spot pressure greater than the surrounding dense fuel pressure[4] and, to achieve ignition, requires a lower energy than the conventional isobaric hot-spot ignition.[4,5] The required driver energy is lowered roughly by the factor $\left(p_{\rm hs} \big/ p_{\rm iso}\right)^{2.5}$ (Ref. 5), where $p_{\rm hs}$ is the nonisobaric hot-spot pressure and $p_{\rm iso}$ is the isobaric pressure. A pressure ratio of ~1.6 results in a 3×-lower ignition energy. This mechanism is very effective in thick-shell implosions, where the ignitor shock wave significantly increases its strength as it propagates through the converging shell. Massive shell implosions have good hydrodynamic-stability properties during the acceleration phase because of low acceleration and small in-flight aspect ratio (IFAR). The number of e foldings of Rayleigh–Taylor (RT) instability growth for the most-dangerous modes with wave numbers about equal to the inverse in-flight target thickness is roughly proportional to the square root of IFAR.[3] Low IFAR implosions are not significantly affected by RT instability.

This article describes initial implosion experiments of the shock-ignition concept that were performed on the OMEGA Laser System[11] using warm plastic surrogate shells and cryogenic shell targets. The power of the OMEGA laser is limited to about 20 TW, thus preventing the investigation of the shock-ignition scheme in ignition-relevant regimes (requiring more than 300 TW). Nevertheless, by lowering the power during the assembly pulse to about 7 TW, a late shock can be launched by a fast rise to about 18 TW. Such OMEGA experiments are used to study important features of the shock-ignition scheme such as hydrodynamic stability, shell compression, and hot-spot compression induced by the late shock. One of the most important aspects to be investigated is the uniformity of the shock-induced hot-spot compression. Since the ignitor shock is launched late in the pulse, its uniformity might be compromised by the large amplitude modulations of the ablation front.

The ignitor shock could transfer such perturbations from the ablation front to the hot spot, thus reducing the uniformity of the compression and possibly quenching the thermonuclear burn. By comparing the implosion performance with and without a shock, we infer the relative effectiveness of the shock compression and hot-spot heating. The low-mode uniformity of the compression is assessed by measuring the modulation in the areal density and by the magnitude of the neutron yield with respect to the calculated 1-D yield. Varying the timing of the peaks in the laser pulse shape optimizes the timing of the shock waves and the implosion performance. Plastic-shell implosions study how fuel–shell mixing affects the yield performance for shock-ignition pulse shapes, compared to standard low-adiabat picket-pulse capsule implosions.[10] Significantly improved performance using shock-ignition–type pulse shapes has been observed, leading to peak ρR exceeding ~0.3 g/cm^2. The following sections present the target types, the laser pulse shapes, and diagnostics; fusion-reaction yield measurements in plastic-shell implosions; areal-density analysis of plastic-shell implosions; and initial spike pulse cryogenic-shell implosions. A summary and conclusions are also presented.

Targets, Laser Pulse Shapes, and Diagnostics

Figure 113.26 shows the targets that were used in the experiments: (a) 40-μm-thick, 430-μm-outer-radius, plastic (CH) shells coated outside with a 0.1-μm layer of aluminum and filled with D_2 gas with pressures ranging from 4 to 45 atm and (b) cryogenic targets comprising a 10-μm-thick, strong deuterated plastic shell and frozen layers of 95-μm-deuterium (D_2) and 78-μm-deuterium–tritium (DT) ice, respectively. Details of the direct-drive cryogenic-target program can be found in Refs. 12–14.

The capsules were imploded by relaxation adiabat pulse shapes[9] for ~16- to 20-kJ UV laser pulses. The 351-nm-wavelength laser light was smoothed with polarization smoothing[15] and distributed phase plates,[16] and in some shots the laser beam was smoothed with 1-THz-bandwidth, 2-D smoothing by spectral dispersion (SSD).[17] Typical experimental pulse shapes with and without spike for warm plastic targets and $\alpha \sim 1.5$ are compared in Fig. 113.27. The shaped pulses comprise an 80-ps full width at half maximum (FWHM) Gaussian prepulse ("picket pulse") and a subsequent shaped main-drive portion consisting of an ~1-TW foot power and a moderate ~6- to 8-TW plateau; the solid curve comprises a high-intensity spike portion ("spike pulse") with a peak power of about ~17 TW. The corresponding nominal laser intensity in the spike portion exceeds 7×10^{14} W/cm^2. The nominal laser intensity refers to the initial target size, while the actual intensity at the critical-density surface at the pulse end is a factor of ~2 higher due to compression. A similar pulse shape without spike but the same laser energy is shown by the dashed curve. The pulse shapes are very similar in the first nanosecond, including the picket intensity, the picket timing, and the foot of the main drive pulse. The no-spike shape reaches a slightly higher power in the plateau. The energy difference in the plateau is transferred to form the spike (solid curve). Zero time marks the onset of the foot of the main drive laser pulse. The picket pulse in front of the foot of the main pulse launches a shock wave that sets the

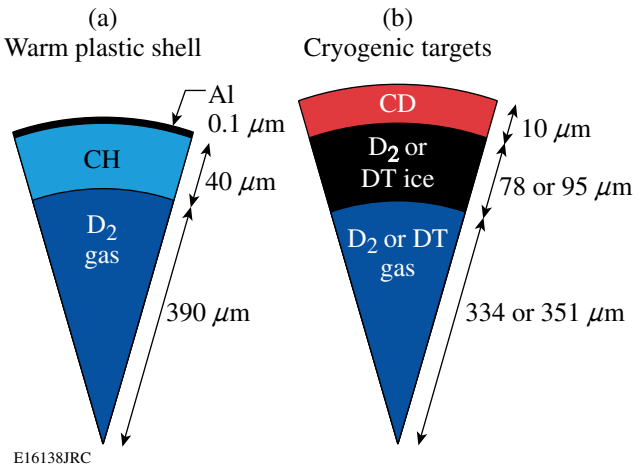

Figure 113.26
Targets that were used to test shock-ignition pulse-shape implosions on the OMEGA Laser Facility.

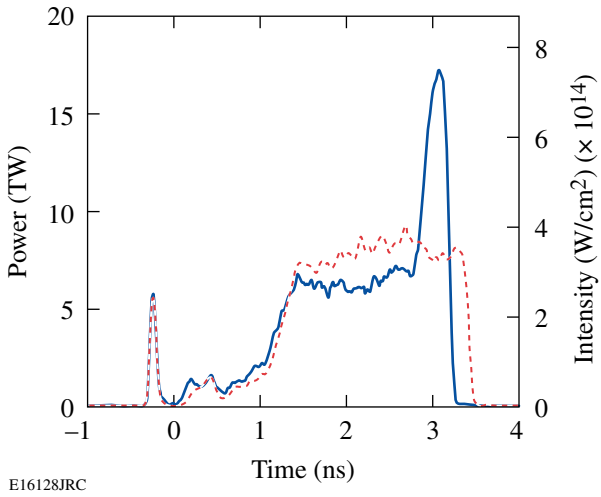

Figure 113.27
Pulse shapes with (solid curve, 46078) and without (dashed, 46073) spike, no SSD. The laser energies were 18.6 kJ (46078) and 19.4 kJ (46073), respectively. The onset of the spike pulse was at 2.8 ns.

adiabat of the implosion and generates a shaped-adiabat profile within the shell that is monotonically decreasing from the outer (ablation) surface toward the inner shell surface (see Fig. 2 in Ref. 10). The use of adiabat-shaping pulses in the context of fast-ignition implosions was suggested in Ref. 9. The relaxation technique[18,19] for adiabat shaping simplifies the laser pulse by lowering the contrast ratio between the peak laser power and the power in the foot of the main pulse. It also improves the hydrodynamic stability of the implosion by decreasing the in-flight aspect ratio and increasing the ablation velocity.

Figure 113.28 shows a schematic of the timing of the various shock waves in a warm surrogate shock-ignition implosion. The picket pulse that is optimally timed with respect to the main drive pulse launches a shock wave (SW) and sets the adiabat of the implosion. The slowly rising part of the main drive launches a compression wave (CW) steepening up while propagating through the shell and then overtakes the SW just before shock breakout at the inner interface. A sharp rise in intensity at the end (spike pulse) generates a "spike shock wave" (SSW) that must be properly timed to meet the return shock in the inner region of the cold shell material. The colliding shocks then generate the shock wave that travels back to the capsule center. In the experiments, the implosion was optimized by measuring the fuel assembly performance as a function of the timing of the picket and spike pulses. The picket pulse was timed by a variable delay line, and the spike pulse timing was varied by using different pulse shapes that were designed so that the low-intensity foot drive was kept the same but had a different temporal onset of the spike portion, which was varied in 100-ps time increments. The trailing edge of the main drive pulse was designed to keep the total laser energy constant.

The diagnostics that were used to measure the implosion performance include proton wedged range filters (WRF's),[20] a nuclear temporal diagnostic (NTD),[21,22] and neutron time-of-flight diagnostics comprising scintillator counters coupled to fast photomultipliers for primary and secondary neutron yield measurements.[23] The kinetic energy downshift of protons generated by the D^3He fusion reactions, which is a secondary-proton production reaction in D_2 fuel, was used to infer areal density[24,25]

$$D + D \longrightarrow {}^3He + n, \tag{1}$$

followed by

$${}^3He + D \longrightarrow p(12.6 - 17.5\ \text{MeV}) + {}^4He. \tag{2}$$

The secondary protons have a considerable energy spread due to the kinetic-energy spread of ^3He produced in the primary reaction. The protons produced in the central hot-spot region pass through the dense, cold shell where their kinetic energy suffers a considerable downshift. Therefore the measurement of the downshifted kinetic-energy spectrum provides information about the shell areal density. By using wedges with an appropriate range of thicknesses and a CR-39 plastic detector, it is possible to make an accurate reconstruction of the proton spectrum by applying the technique discussed by Séguin *et al.* in Ref. 20. The lower detection limit given by the thinnest

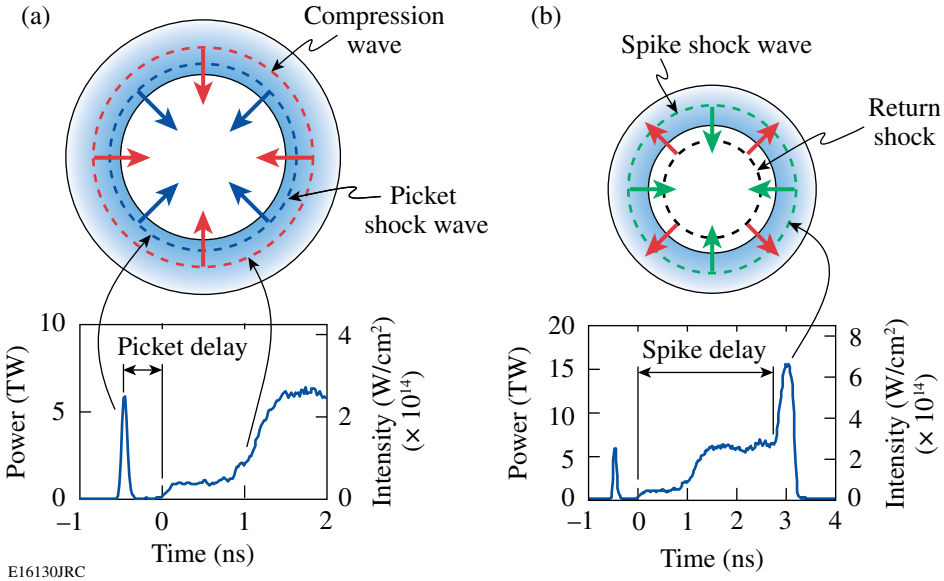

Figure 113.28
Schematic of the timing of the various shock waves generated by the picket pulse, the drive pulse, and the high-intensity spike pulse.

wedge section is ~4 MeV. The proton spectra were measured at four locations around the target. Areal-density measurements based on the fusion proton-spectrum downshift are routinely used at LLE.[25,26]

Measurements of Fusion-Reaction Yield in Plastic-Shell Implosions

A series of plastic-shell implosions with D_2-fill pressures in the range of 9 to 45 atm were performed with and without SSD using a low-adiabat pulse shape without a spike portion [Fig. 113.29(a)]. The pulse shapes were similar to that shown in Fig. 113.27 (dashed curve) but with a higher main-drive power of ~11 to 13 TW. The ratio of the measured primary neutron yield to that predicted by 1-D simulations using the hydrodynamic code *LILAC*,[27] or neutron yield-over-clean (YOC), is shown in Fig. 113.29(b) for these implosions as a function of the calculated hot-spot convergence ratio (bottom) and fill pressure (top). The calculated hot-spot convergence ratio (CR) is defined as the initial inner target-shell radius divided by the minimum radius of the gas–shell interface at peak compression. The YOC is ~4% at 45 atm and decreases with lower pressure and higher CR to ~1%. SSD has no significant effect on the yield performance, indicating that thermal conductivity in the plasma formed by the picket pulse effectively smoothes short-wavelength structures in the laser beams (imprinting). A YOC decrease by a factor of ~4 when CR increases from ~9 to ~23 indicates an increased small length mixing for smaller hot-spot radii. Large convergence ratios of the fuel and the slow assembly make plastic shells inherently RT instable during the deceleration phase, giving rise to a substantial shell–fuel mixing[28] that quenches fusion reactions and typically results in YOC of a few percent.[10] Mixing is enhanced in these low-velocity implosions because the hot spot is small relative to the target size.[29] In comparison, shock-ignition–type pulse shapes considerably improve the performance (see Fig. 113.32 on p. 30).

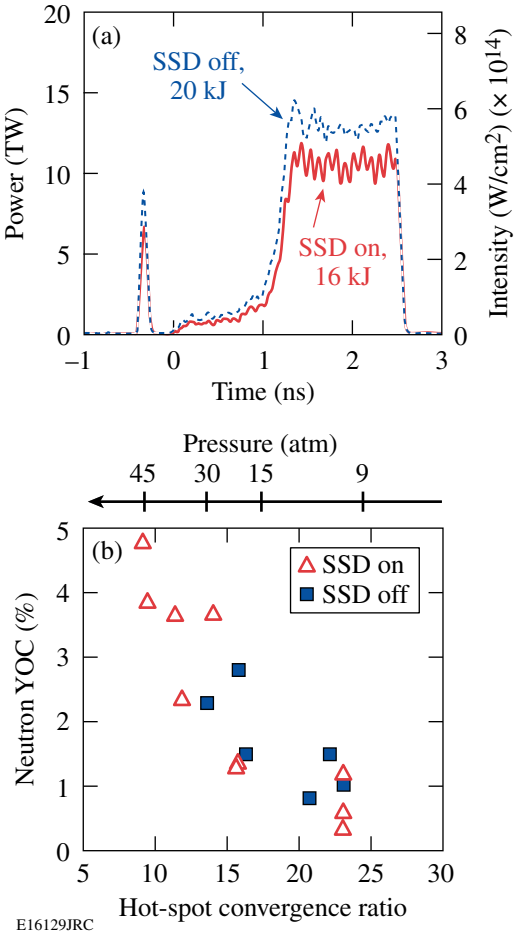

Figure 113.29
(a) Low-adiabat relaxation laser pulse shapes without a spike pulse. (b) Measured neutron yield over clean versus hot-spot convergence ratio (bottom) and D_2-fill pressure (top) of plastic-shell implosions. The open triangles depict measurement with SSD; the solid squares depict measurement without SSD.

A systematic study of low-adiabat ($\alpha \approx 1.5$) plastic-shell implosions with a short picket and a high-intensity spike was performed at a constant pressure of 25 atm, a fixed laser energy of 17 kJ, and a fixed spike-pulse timing of 2.8 ns as a function of picket timing (see Fig. 113.30). The measured neutron (open circles) and proton (solid squares) numbers are shown in Fig. 113.30(a) as a function of the picket-pulse delay. Zero determines the onset of the foot of the main drive, and an increased delay shifts the picket earlier in time away from the foot. The neutron and proton yields increase by a factor of ~2 from $3.5\pm0.4 \times 10^9$ to $8.0\pm0.8 \times 10^9$ and $2.6\pm0.5 \times 10^6$ to $6.2\pm1.2 \times 10^6$, respectively, when shifting from –550 ps to zero, which is the optimum picket timing. Calculated neutron and proton yields using the 1-D hydrocode *LILAC*[27] and a constant flux limiter of 0.06 show a similar trend, but the predicted yield variation is not as pronounced as in the measurement. Figure 113.30(b) shows that the picket timing also affects the measured average areal density ($\langle \rho R \rangle$). An ~100-ps mistiming lowers the yield by ~25%, which is significant compared to the neutron-yield measurement uncertainty of ~10%, and a delay by up to approximately –550 ps degrades the yield by a factor of ~2 and $\langle \rho R \rangle$ by ~20%. The measurement shows how shock-wave timing of SW and CW affects the implosion performance of these surrogate targets (see Fig. 113.28). If the CW is too late, the first shock enters the fuel, prematurely compressing and heating it, while if the CW is too early, the inner target portion is placed on too high an adiabat, reducing its compressibility. For direct-drive, hot-spot ignition target designs, the CW must overtake the first shock within ±150 ps of the design

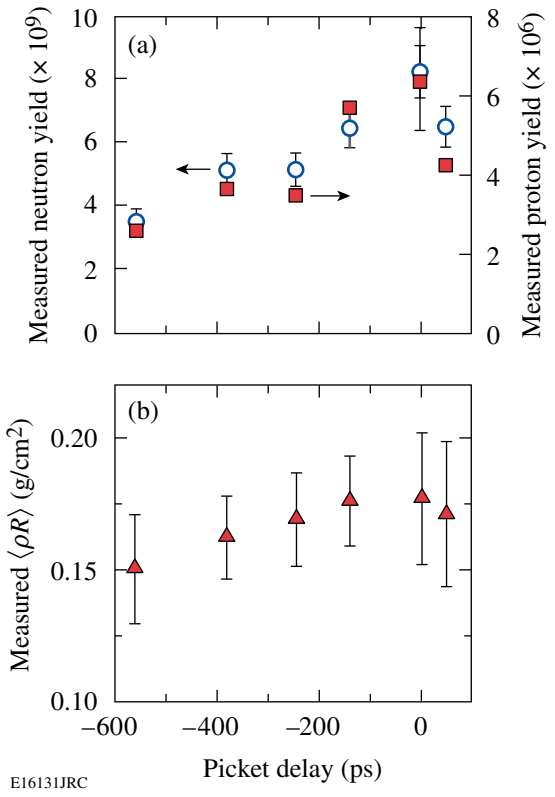

Figure 113.30
(a) Measured neutron (open circles) and proton (solid squares) yields as functions of the picket-pulse timing. Zero determines the onset of the foot of the main drive and an increased delay shifts the picket earlier in time away from the foot. (b) Corresponding measured average areal density. The relative $\langle \rho R \rangle$ error bars are shown.

specification.[30] For the surrogate CH experiments, the best results were obtained for time-zero for both the yield and $\langle \rho R \rangle$ with $\langle \rho R \rangle = 0.18 \pm 0.02$ g/cm^2 under the experimental conditions of Fig. 113.30. This shows that the correct timing of SW and CW has been obtained. More details on the areal-density measurements are discussed in **Areal-Density Analysis of Plastic-Shell Implosions** (p. 30).

The implosion was further optimized by studying how the timing of the SSW affects the implosion performance. This was done with different pulse shapes that were designed to have the same low-intensity foot and plateau, but a different spike-pulse timing. Figure 113.31(a) shows an overview of the neutron-yield measurements. The solid circle data point represents a measurement for a pulse shape without a high-intensity spike, yielding $1.8 \pm 0.2 \times 10^9$ neutrons with 19.4-kJ laser energy. In comparison, a spike pulse with a 2.8-ns delay and slightly less laser energy (18.6 kJ) results in 4× more neutrons ($8.0 \pm 0.8 \times 10^9$, upper triangle). The proton yield increases by a factor of ~5 from $1.3 \pm 0.3 \times 10^6$ to $6.2 \pm 1.2 \times 10^6$. All other data points were measured with ~17-kJ laser energy, which explains why the second triangle at 2.8 ns is lower. The triangles represent the measurement for a picket delay of –300 ps, and the squares are a series with –100-ps picket delay. Figure 113.30(a) shows that a shorter picket delay results in an improved yield, which is consistent with the fact that the square data points in Fig. 113.31(a) are slightly higher than the triangles. The measurement in Fig. 113.31(a) demonstrates an optimum timing of the spike-pulse delay at 2.8 ns. A mistiming by 100 ps significantly affects the yield. One-dimensional hydrodynamic simulations using the code *LILAC* do not predict a maximum in neutron yield at 2.8 ns and show very little sensitivity of the fusion-product yield on SSW timing [see Fig. 113.31(b)]. The calculated 1-D yield for the SSW implosion with 18.6 kJ (upper triangle at 2.8 ns) is only slightly higher than a comparable implosion without SSW and 19.4 kJ of laser energy. Calculations for exactly the same laser energy predict ~30%

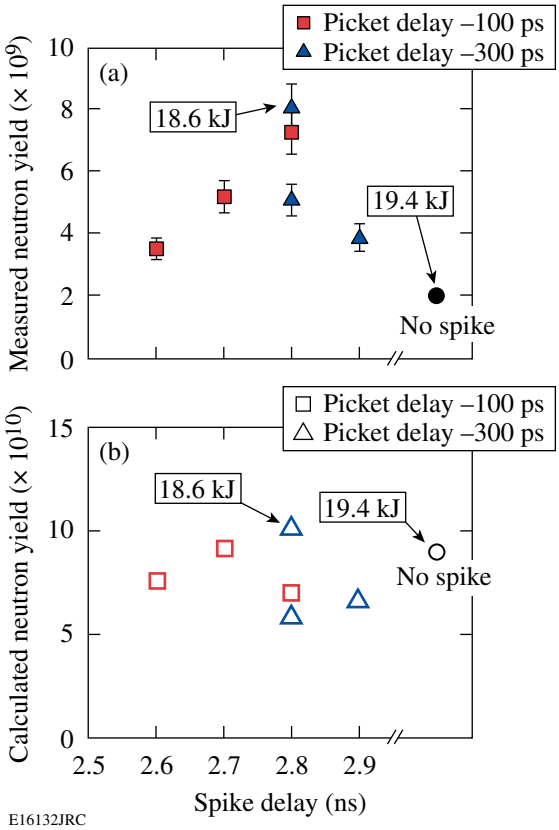

Figure 113.31
(a) Measured neutron yield as a function of the onset of the spike pulse, for two different picket-pulse delays. The targets were filled with 25 atm of D_2. The pulse without spike (solid circle) used a −300-ps picket delay. (b) Calculated neutron yield versus spike-pulse delay.

yield enhancement by the SSW, which is much lower than measured. As mentioned before, the SSW energy coupling into the hot spot is optimal for thick-shell targets because the ignitor shock strength increases significantly when traveling through the converging shell. Compared to an ignition design with a target shell thickness of ~350 μm (Ref. 5), the present targets (40 μm CH, ~100 μm cryo) are thin-shell targets, which explains why the simulated enhancement is only marginal. It is not yet clear why the targets perform much better than predicted, but there are several possible explanations. Plastic shells with low-pressure fills are inherently RT instable during the deceleration phase, giving rise to substantial shell–fuel mixing that quenches fusion reactions, which is believed to be the main cause for the YOC's in the percent range. The experiments presented here suggest that for optimal SSW timing, the mixing processes are mitigated, which might be caused by the impulse acceleration by the SSW that shortens the time period for the instability growth or by a steepening of the density profile at the inner shell surface. Another possibility, which is not very likely, would be that the hot-spot heat-transport losses are not modeled correctly and that the temperature increase produced by the SSW is larger than predicted, leading to the higher yield. Multidimensional hydrodynamic simulations have been started to study this effect in more detail.

The implosion performance was studied with the optimized spike-pulse shape for various shell-fill pressures between 4 and 25 atm. Figure 113.32 compares the YOC versus CR for implosions with an optimized spike-pulse shape (circles) and various pulse forms without a spike pulse (diamonds), including the data from Fig. 113.29(b). The implosions without a spike pulse were not optimized with respect to shock-wave timing. The experiments demonstrate that YOC close to 10% has been obtained for plastic-shell, α = 1.5 to 1.9, low-adiabat implosions and CR of up to 30, indicating an improved stability with shock-ignition–type pulse shapes.

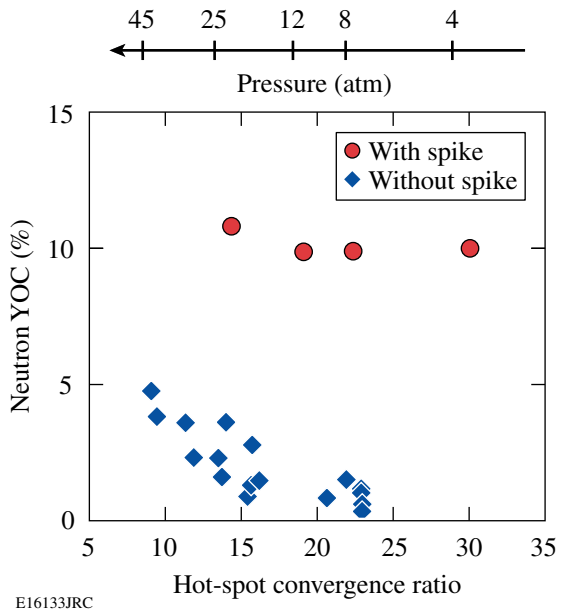

Figure 113.32
The neutron YOC versus 1-D calculated hot-spot convergence ratio. The YOC is close to 10% for a hot-spot convergence of up to 30.

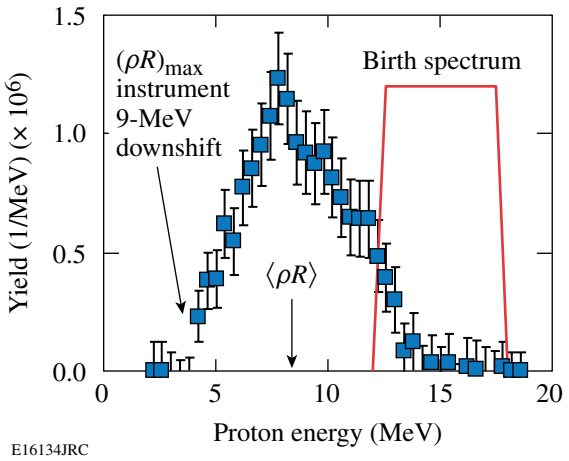

Figure 113.33
Measured proton spectra for shot 48674, which is the average of four spectra taken from different directions. The 8.3-atm, D_2-filled CH shell was imploded with 18.0 kJ without SSD. The average areal density was measured with $\langle \rho R \rangle$ = 0.204±0.014 g/cm^2, and the measured maximum areal density of 0.3 g/cm^2 is restricted by the detection limit of the instrument.

Areal-Density Analysis of Plastic-Shell Implosions

Figure 113.33 shows the measured proton spectrum, which is the average of four individual proton spectra taken from different lines of sight, for an 8.3-atm, D_2-fill implosion with a laser energy of 18 kJ without SSD. All of the measurements described in this section were performed without SSD. A mean downshift of 6.38±0.13 MeV was measured where the error represents the standard deviation over the four measurements. Following Refs. 20 and 24, an areal density averaged over the proton spectral distribution of $\langle \rho R \rangle$ = 0.204±0.003 g/cm^2 is inferred where the uncertainty represents the standard deviation of $\langle \rho R \rangle$ from the four measurements. SSD smoothing was found to have no significant effect on ρR for relaxation-type low-adiabat implosions,[10] and the small standard deviation of the ρR measurement indicates high shell stability. Notice that the lower limit of the detector given by the thickness of the Al wedges[20] is at a proton energy of 4 MeV, which appears as a cutoff in the measured spectrum. The protons need to be

downshifted by ~9 MeV to reach the cutoff that corresponds to a ρR value of ~0.3 g/cm^2. Therefore, the proton spectrum indicates that areal densities even higher than 0.3 g/cm^2 were experimentally realized. Calculations with the 1-D code *LILAC*[27] using a constant flux limiter of 0.06 predict, for shot 48674, $(\rho R)_{max}$ = 0.345 g/cm^2 and with a time-dependent flux limiter (Refs. 31 and 32) $(\rho R)_{max}$ = 0.331 g/cm^2. The time-dependent flux-limiter calculations model the nonlocal heat transport by introducing an effective temporal varying flux limiter.[32] For the ρR inference a fusion-reaction-rate–averaged density of 110 g/cm^3 and a temperature of 0.1 keV were taken from simulations. The inferred ρR value depends slightly on the density. A density variation of ±50 g/cm^3 changes the areal density by ~±0.01 g/cm^2. The temperature dependence is negligible. The absolute calibration uncertainty of the WRF is ±0.4 MeV for the mean value of the proton spectral distribution corresponding to ±0.01 g/cm^2. Taking the statistical fluctuation, the density variation, and the calibration uncertainty into account, an absolute measurement error of ~±0.014 g/cm^2 is estimated, leading to $\langle \rho R \rangle$ = 0.204±0.014 g/cm^2.

Areal-density measurements were performed for various fill pressures corresponding to various hot-spot convergence ratios. Figure 113.34 shows that implosions with optimized spike pulse shapes (open triangles) achieve the highest $\langle \rho R \rangle$ values that have a tendency to increase with CR from ~15 to ~25. The data point at CR ~ 30 falls below the scaling, indicating that for large CR the $\langle \rho R \rangle$ measurement is affected by the instrumental cutoff and by the sampling over the $\langle \rho R \rangle$ time evolution (see Fig. 113.35). The solid line is a linear fit through the first three open triangle data points. In contrast, lower $\langle \rho R \rangle$ values are measured for a mistimed picket (solid triangles) and the lowest $\langle \rho R \rangle$ values are observed without SSW (squares), showing also a larger data scattering. Figures 113.32 and 113.34 reveal that optimum timed shock-ignition pulse-shape implosions show an improved performance with higher $\langle \rho R \rangle$ and suggest less instability growth.

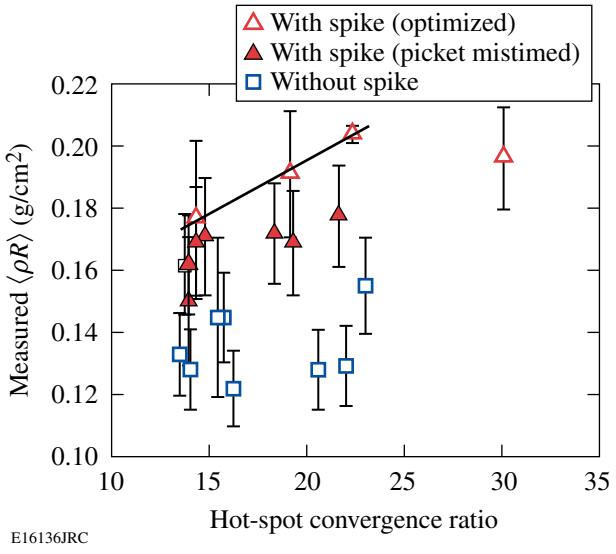

Figure 113.34
$\langle \rho R \rangle$ versus CR for 2.8-ns spike-delay pulse implosions (optimized pulse shape—open triangles; picket mistimed—solid triangles) and no-spike pulse-shape implosions (open squares). The relative $\langle \rho R \rangle$ error bars are shown.

Figure 113.35(a) shows all of the measured SSW implosion $\langle \rho R \rangle$ data versus the 1-D prediction with a time-dependent flux limiter. To relate the measured $\langle \rho R \rangle$ obtained from the mean of the proton spectrum to the 1-D calculation, the predicted ρR evolution is averaged over a time window in which the fusion products are generated and weighted according to the production rate.[33] The simulations in Fig. 113.35(b) show that the ρR (thick solid curve) increases during neutron production and that the fusion reactions are quenched near the time of a peak areal density of 0.33 g/cm^2. The measured neutron rate (thin solid curve) is lower and truncated compared to the 1-D simulated fusion rate (dashed), probably caused by shell–fuel mixing. Mixing is a time-dependent process that is small in the initial phase of ρR buildup and then grows during the deceleration, leaving a clean hot-spot radius equal to the so-called free-fall line.[34] The corresponding time-integrated proton spectrum is shown in Fig. 113.33; each point of the spectrum corresponds to a different downshift and, therefore, to a different ρR. The energy downshift of the low-energy tail of the spectrum represents a measure of the peak ρR during the neutron production, which was limited by the instrument indicating peak ρR exceeding 0.3 g/cm^2, in agreement with the simulations. The temporal shape of the neutron-production rate is close to the secondary-proton–production rate[26] and is used to calculate the neutron-rate–averaged $\langle \rho R \rangle_n$ [Fig. 113.35(a)]. The experimental error of the absolute timing of NTD[22] is ~50 ps and, considering that the neutron-production duration is typically less than 300 ps, the calculated $\langle \rho R \rangle_n$ values are very sensitive to the timing of the measured neutron rate. The timing error of the measured rate was taken into account for these calculations, leading to the uncertainties in the calculated $\langle \rho R \rangle_n$ shown as x-error bars in Fig. 113.35(a). Figure 113.35 shows that the fuel assembly is close to the burn-weighted 1-D predictions of the code *LILAC* with measured ρR values achieving larger than 90% of the 1-D prediction. The slight deviation at high compression is partially due to the instrumental cutoff resulting in a slightly lower $\langle \rho R \rangle$ reading.

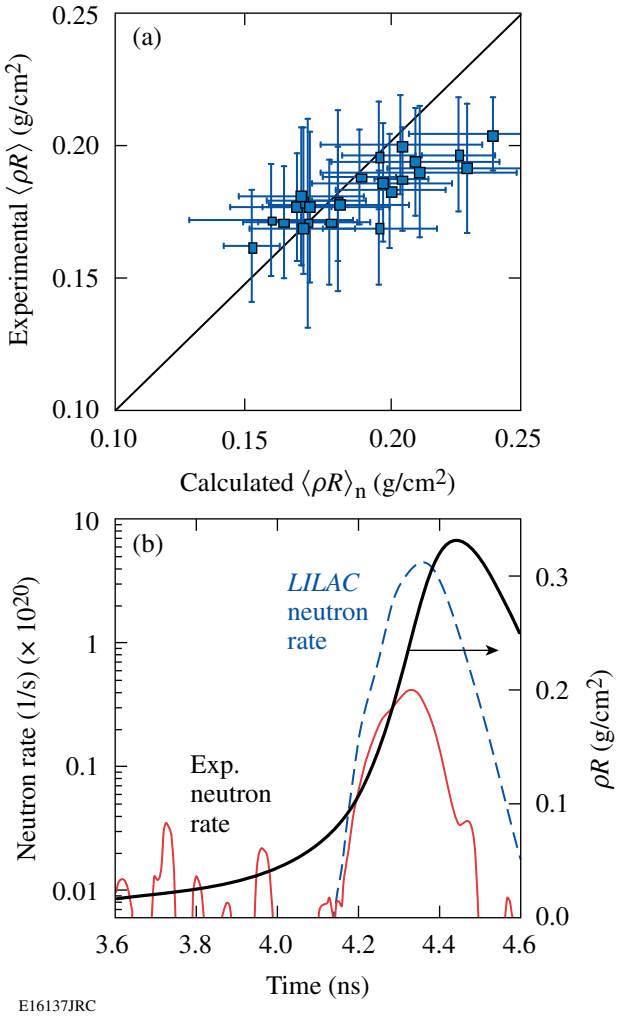

Figure 113.35
(a) Measured spike-pulse implosion $\langle \rho R \rangle$ versus *LILAC*-calculated neutron-rate–averaged $\langle \rho R \rangle_n$ and (b) comparison of measured neutron rate (thin solid curve), 1-D predicted neutron rate (dashed curve), and predicted ρR evolution (thick solid curve) for shot 48674 (proton spectrum in Fig. 113.33). The absolute measurement $\langle \rho R \rangle$ uncertainties are shown in (a).

Initial Spike-Pulse Cryogenic-Shell Implosions

Initial shock-spike implosions with cryogenic D_2 and DT targets [Fig. 113.26(b)] were performed using spike-pulse shapes similar to that shown in Fig. 113.27 with a total laser energy of 16.0 kJ for the D_2 target and 17.9 kJ for the DT target. In both cases SSD was used. High-quality targets with ice-layer nonuniformities of σ_{rms} = 1.5 μm (D_2) and 0.9 μm (DT) were imploded. The D_2 target implosion suffered from a large 49±3-μm offset of the capsule center from target chamber center, which caused a significant drive asymmetry. A low-mode ρR modulation was measured with the higher areal density toward the higher-intensity drive side. By averaging the four lines of sight, an areal density of $\langle \rho R \rangle$ = 0.18±0.05 g/cm^2 was measured, which is compared to a calculated value of 0.20 g/cm^2 (time-dependent flux limiter)[32] taking the measured fusion-reaction history into account. Therefore, the assembled fuel reaches ~90% of the 1-D prediction. The neutron yield is ~5% of the 1-D prediction. A similar D_2 cryogenic-target implosion using a similar waveform but without a spike pulse and with a better target offset of 19±3 μm yielded a slightly higher YOC of ~7% and $\langle \rho R \rangle$ = 0.20±0.02 g/cm^2 (Ref. 35). Table 113.I compares the implosion performance of cryogenic targets using low-adiabat picket-pulse shapes with and without a high-intensity spike at the end of the drive pulse. No measured ρR data are available for the DT implosions because the WRF diagnostic is compromised by the large neutron influx. DT target shot 48734 (with a late spike pulse) had very good ice-layer quality and small target offset resulting in YOC of ~12%, while a comparable shot without a spike pulse (48304) gave a YOC of ~10%. Due to a diagnostic error, no target-offset data are available for shot 48304. The first few shock-ignition cryo implosions on OMEGA were among the best performing (in terms of yield and ρR) but did not yet exceed the performance of standard pulse shapes. This is likely due to a non-optimal pulse shape when SSD was employed. The SSD bandwidth broadened the spike pulse sufficiently so that *LILAC* simulations do not show a SSW. The spike-pulse rise time without SSD in the plastic-shell implosions is about twice as fast and generates a significant SSW. Further experimental studies will assess the implosion performance of cryogenic targets without SSD, working toward an improved pulse shape with SSD, which will then allow a strong enough shock with the late spike pulse to be generated.

Parametric plasma instabilities are of concern in an ignition target design[5] with spike-pulse intensities in the range of 10^{15} to 10^{16} W/cm^2 and an ~150-ps FWHM pulse. The instabilities increase the back-reflection of laser light from the target and therefore lower the coupling efficiency into the capsule, while an increased fraction of the coupled energy will be transferred into suprathermal electrons, which are a potential source of preheat. No measurable amount of stimulated Raman and Brillouin backscatter is detected in the above-discussed cryogenic implosions having nominal laser peak intensities of ~8×10^{14} W/cm^2. The actual intensity at the critical-density surface is a factor of ~2 higher when the target compression is taken into account. There is a measurable amount of hard x-ray yield above ~50 keV due to fast electrons produced by the two-plasmon–decay (TPD) instability. Since $\langle \rho R \rangle$ reaches ~90% of the 1-D prediction, there is no significant degradation of the implosion due to preheat. There are no parametric-

Table 113.I: A comparison of the implosion performance of cryogenic targets using low-adiabat picket-pulse shapes with and without a high-intensity spike at the end of the drive pulse.

Shot #	47206	48386	48304	48734
Target	D_2	D_2	DT	DT
Ice layer σ (μm)	2.4	1.5	0.7	0.9
Target offset (μm)	19±3	49±3	No data	10±5
Spike pulse	No	Yes	No	Yes
E_{laser} (kJ)	16.5	16.0	19.3	17.9
Adiabat	1.8	2.0	2.0	2.0
$\langle\rho R\rangle_{\text{exp}}$ (g/cm^2)	0.201±0.021	0.182±0.046	No data	No data
$\langle\rho R\rangle_{LILAC}$ (g/cm^2)	0.216	0.204	0.186	0.194
T_{ion} (keV) (exp)	2.1±0.5	1.8±0.5	2.5±0.5	1.9±0.5
T_{ion} (keV) (*LILAC*)	2.0	1.9	2.3	2.3
Y_{n}	7.70×10^9	3.40×10^9	1.60×10^{12}	1.43×10^{12}
(YOC)	7.3%	5.3%	9.8%	12.3%

instability measurements for shock-ignition-target–relevant conditions available (spherical cryogenic target, long density scale length, and intensities above 2×10^{15} W/cm^2). However, measurements of parametric instabilities for indirect-drive–relevant ignition-plasma conditions with millimeter-density scale length and 15% critical-density targets report a backscatter of the order of a few percent to 10% at 5×10^{15} W/cm^2 (Ref. 36). The density scale lengths in shock-ignition targets are shorter, and for similar laser intensities the backscatter is expected to be of the order of ~10% or less. Parametric instability and fast-electron–generation scaling measurements at direct-drive-ignition–relevant intensities and long density scale lengths in warm surrogate targets show that the TPD-generated preheat starts to saturate at intensities above $\sim 1 \times 10^{15}$ W/cm^2 (Ref. 37). Moderate-energy fast electrons (~100 keV) generated by the late high-intensity spike might even be beneficial for the shock-ignition concept. The effect of preheating was studied in marginal-igniting, 350-μm-thick massive shells with the 1-D *LILAC* code using a multigroup diffusion model for the fast-electron transport and a Maxwellian hot-electron-energy distribution of 150-keV characteristic energy.[5] There is considerable compression at the time when the fast electrons are generated with $\langle\rho R\rangle \approx 70$ mg/cm^2, compared to a 17-mg/cm^2 stopping range of a 100-keV electron in the cryogenic DT shell. The majority of the fast electrons are stopped in the outer layers of the shell and pose no threat of the implosion performance being compromised by preheat. Moderate-energy fast electrons actually increase the strength of the SSW, therefore widening the shock-launching ignition window.[5]

Summary and Conclusions

Fuel assembly that is relevant for the shock-ignition ICF concept has been experimentally studied for the first time. The experiments were performed on the OMEGA laser using shock-ignition laser pulse shapes and warm plastic surrogate and cryogenic targets. Systematic studies of low-adiabat ($\alpha \approx 1.5$) implosions with a short picket and a high-intensity spike were performed. It was demonstrated that the fuel assembly with warm plastic targets is close to 1-D simulation predictions with neutron-rate–averaged areal densities exceeding ~0.2 g/cm^2 and maximum ρR above ~0.3 g/cm^2, which are significantly higher than without the spike pulse. Implosions of D_2-filled, 40-μm-thick plastic shells were optimized by measuring the performance as a function of the timing of the picket and spike pulses. The spike-shock–generated implosion produces a factor of ~4–enhanced neutron yield compared to a laser pulse shape without intensity spike for 25-atm fill pressure and the same laser energy. For an optimized spike-pulse shape with respect to shock-wave timing, the measured neutron yields are ~10% of the yields calculated by 1-D simulations (YOC) for fill pressures down to 4 atm, while the YOC without a spike pulse (not optimized) is less than 1% for pressures below 9 atm. These are the highest YOC's reported so far for $\alpha \approx 1.5$ implosions of warm plastic shells and a hot-spot convergence ratio of ~30. Plastic shells with low fill pressures are inherently RT instable during the deceleration phase, giving rise to a substantial shell–fuel mixing that quenches fusion reactions, which is not described by 1-D simulations. The measurements have shown that the shock-ignition concept is very promising by achieving higher

compression and better stability than comparable low-adiabat, relaxation-picket plastic-shell implosions without a spike pulse. Initial experiments with cryogenic D_2 and DT targets and $\alpha = 2$, spike and no-spike pulse shapes were performed, showing close to 1-D performance and a neutron YOC of ~12%.

ACKNOWLEDGMENT

This work was supported by the U.S. Department of Energy Office of Fusion Energy Sciences under contract DE-FC02-04ER54789 and by the Office of Inertial Confinement Fusion under Cooperative Agreement No. DE-FC52-08NA28302, the University of Rochester, and the New York State Energy Research and Development Authority. The support of DOE does not constitute an endorsement by DOE of the views expressed in this article.

REFERENCES

1. J. Nuckolls *et al.*, Nature **239**, 139 (1972).
2. J. D. Lindl, *Inertial Confinement Fusion: The Quest for Ignition and Energy Gain Using Indirect Drive* (Springer-Verlag, New York, 1998), p. 4.
3. S. Atzeni and J. Meyer-ter-Vehn, *The Physics of Inertial Fusion: Beam Plasma Interaction, Hydrodynamics, Hot Dense Matter*, International Series of Monographs on Physics (Clarendon Press, Oxford, 2004), p. 52.
4. R. Betti, C. D. Zhou, K. S. Anderson, L. J. Perkins, W. Theobald, and A. A. Solodov, Phys. Rev. Lett. **98**, 155001 (2007).
5. R. Betti, W. Theobald, C. D. Zhou, K. S. Anderson, P. W. McKenty, D. Shvarts, and C. Stoeckl, "Shock Ignition of Thermonuclear Fuel with High Areal Density," to be published in the Journal of Physics: Conference Series (Institute of Physics).
6. M. C. Herrmann, M. Tabak, and J. D. Lindl, Phys. Plasmas **8**, 2296 (2001).
7. M. Tabak *et al.*, Phys. Plasmas **1**, 1626 (1994).
8. M. Murakami and H. Nagatomo, Nucl. Instrum. Methods Phys. Res. A **544**, 67 (2005).
9. R. Betti and C. Zhou, Phys. Plasmas **12**, 110702 (2005); R. Betti, K. Anderson, T. R. Boehly, T. J. B. Collins, R. S. Craxton, J. A. Delettrez, D. H. Edgell, R. Epstein, V. Yu. Glebov, V. N. Goncharov, D. R. Harding, R. L. Keck, J. H. Kelly, J. P. Knauer, S. J. Loucks, J. A. Marozas, F. J. Marshall, A. V. Maximov, D. N. Maywar, R. L. McCrory, P. W. McKenty, D. D. Meyerhofer, J. Myatt, P. B. Radha, S. P. Regan, C. Ren, T. C. Sangster, W. Seka, S. Skupsky, A. A. Solodov, V. A. Smalyuk, J. M. Soures, C. Stoeckl, W. Theobald, B. Yaakobi, C. Zhou, J. D. Zuegel, J. A. Frenje, C. K. Li, R. D. Petrasso, and F. H. Séguin, Plasma Phys. Control. Fusion **48**, B153 (2006).
10. C. D. Zhou, W. Theobald, R. Betti, P. B. Radha, V. A. Smalyuk, D. Shvarts, V. Yu. Glebov, C. Stoeckl, K. S. Anderson, D. D. Meyerhofer, T. C. Sangster, C. K. Li, R. D. Petrasso, J. A. Frenje, and F. H. Séguin, Phys. Rev. Lett. **98**, 025004 (2007).
11. T. R. Boehly, D. L. Brown, R. S. Craxton, R. L. Keck, J. P. Knauer, J. H. Kelly, T. J. Kessler, S. A. Kumpan, S. J. Loucks, S. A. Letzring, F. J. Marshall, R. L. McCrory, S. F. B. Morse, W. Seka, J. M. Soures, and C. P. Verdon, Opt. Commun. **133**, 495 (1997).
12. C. Stoeckl, C. Chiritescu, J. A. Delettrez, R. Epstein, V. Yu. Glebov, D. R. Harding, R. L. Keck, S. J. Loucks, L. D. Lund, R. L. McCrory, P. W. McKenty, F. J. Marshall, D. D. Meyerhofer, S. F. B. Morse, S. P. Regan, P. B. Radha, S. Roberts, T. C. Sangster, W. Seka, S. Skupsky, V. A. Smalyuk, C. Sorce, J. M. Soures, R. P. J. Town, J. A. Frenje, C. K. Li, R. D. Petrasso, F. H. Séguin, K. Fletcher, S. Padalino, C. Freeman, N. Izumi, R. Lerche, and T. W. Phillips, Phys. Plasmas **9**, 2195 (2002).
13. T. C. Sangster, J. A. Delettrez, R. Epstein, V. Yu. Glebov, V. N. Goncharov, D. R. Harding, J. P. Knauer, R. L. Keck, J. D. Kilkenny, S. J. Loucks, L. D. Lund, R. L. McCrory, P. W. McKenty, F. J. Marshall, D. D. Meyerhofer, S. F. B. Morse, S. P. Regan, P. B. Radha, S. Roberts, W. Seka, S. Skupsky, V. A. Smalyuk, C. Sorce, J. M. Soures, C. Stoeckl, K. Thorp, J. A. Frenje, C. K. Li, R. D. Petrasso, F. H. Séguin, K. A. Fletcher, S. Padalino, C. Freeman, N. Izumi, J. A. Koch, R. A. Lerche, M. J. Moran, T. W. Phillips, and G. J. Schmid, Phys. Plasmas **10**, 1937 (2003).
14. T. C. Sangster, R. Betti, R. S. Craxton, J. A. Delettrez, D. H. Edgell, L. M. Elasky, V. Yu. Glebov, V. N. Goncharov, D. R. Harding, D. Jacobs-Perkins, R. Janezic, R. L. Keck, J. P. Knauer, S. J. Loucks, L. D. Lund, F. J. Marshall, R. L. McCrory, P. W. McKenty, D. D. Meyerhofer, P. B. Radha, S. P. Regan, W. Seka, W. T. Shmayda, S. Skupsky, V. A. Smalyuk, J. M. Soures, C. Stoeckl, B. Yaakobi, J. A. Frenje, C. K. Li, R. D. Petrasso, F. H. Séguin, J. D. Moody, J. A. Atherton, B. D. MacGowan, J. D. Kilkenny, T. P. Bernat, and D. S. Montgomery, Phys. Plasmas **14**, 058101 (2007).
15. T. R. Boehly, V. A. Smalyuk, D. D. Meyerhofer, J. P. Knauer, D. K. Bradley, R. S. Craxton, M. J. Guardalben, S. Skupsky, and T. J. Kessler, J. Appl. Phys. **85**, 3444 (1999).
16. Y. Lin, T. J. Kessler, and G. N. Lawrence, Opt. Lett. **21**, 1703 (1996).
17. S. Skupsky, R. W. Short, T. Kessler, R. S. Craxton, S. Letzring, and J. M. Soures, J. Appl. Phys. **66**, 3456 (1989).
18. K. Anderson and R. Betti, Phys. Plasmas **11**, 5 (2004).
19. J. P. Knauer, K. Anderson, R. Betti, T. J. B. Collins, V. N. Goncharov, P. W. McKenty, D. D. Meyerhofer, P. B. Radha, S. P. Regan, T. C. Sangster, V. A. Smalyuk, J. A. Frenje, C. K. Li, R. D. Petrasso, and F. H. Séguin, Phys. Plasmas **12**, 056306 (2005).
20. F. H. Séguin, J. A. Frenje, C. K. Li, D. G. Hicks, S. Kurebayashi, J. R. Rygg, B.-E. Schwartz, R. D. Petrasso, S. Roberts, J. M. Soures, D. D. Meyerhofer, T. C. Sangster, J. P. Knauer, C. Sorce, V. Yu. Glebov, C. Stoeckl, T. W. Phillips, R. J. Leeper, K. Fletcher, and S. Padalino, Rev. Sci. Instrum. **74**, 975 (2003).
21. R. A. Lerche, D. W. Phillion, and G. L. Tietbohl, Rev. Sci. Instrum. **66**, 933 (1995).
22. C. Stoeckl, V. Yu. Glebov, S. Roberts, T. C. Sangster, R. A. Lerche, R. L. Griffith, and C. Sorce, Rev. Sci. Instrum. **74**, 1713 (2003).
23. V. Yu. Glebov, D. D. Meyerhofer, C. Stoeckl, and J. D. Zuegel, Rev. Sci. Instrum. **72**, 824 (2001).

24. C. K. Li, D. G. Hicks, F. H. Séguin, J. A. Frenje, R. D. Petrasso, J. M. Soures, P. B. Radha, V. Yu. Glebov, C. Stoeckl, D. R. Harding, J. P. Knauer, R. L. Kremens, F. J. Marshall, D. D. Meyerhofer, S. Skupsky, S. Roberts, C. Sorce, T. C. Sangster, T. W. Phillips, M. D. Cable, and R. J. Leeper, Phys. Plasmas **7**, 2578 (2000).

25. R. D. Petrasso, J. A. Frenje, C. K. Li, F. H. Séguin, J. R. Rygg, B. E. Schwartz, S. Kurebayashi, P. B. Radha, C. Stoeckl, J. M. Soures, J. Delettrez, V. Yu. Glebov, D. D. Meyerhofer, and T. C. Sangster, Phys. Rev. Lett. **90**, 095002 (2003).

26. V. A. Smalyuk, P. B. Radha, J. A. Delettrez, V. Yu. Glebov, V. N. Goncharov, D. D. Meyerhofer, S. P. Regan, S. Roberts, T. C. Sangster, J. M. Soures, C. Stoeckl, J. A. Frenje, C. K. Li, R. D. Petrasso, and F. H. Séguin, Phys. Rev. Lett. **90**, 135002 (2003).

27. J. Delettrez, R. Epstein, M. C. Richardson, P. A. Jaanimagi, and B. L. Henke, Phys. Rev. A **36**, 3926 (1987); M. C. Richardson, P. W. McKenty, F. J. Marshall, C. P. Verdon, J. M. Soures, R. L. McCrory, O. Barnouin, R. S. Craxton, J. Delettrez, R. L. Hutchison, P. A. Jaanimagi, R. Keck, T. Kessler, H. Kim, S. A. Letzring, D. M. Roback, W. Seka, S. Skupsky, B. Yaakobi, S. M. Lane, and S. Prussin, in *Laser Interaction and Related Plasma Phenomena*, edited by H. Hora and G. H. Miley (Plenum Publishing, New York, 1986), Vol. 7, pp. 421–448.

28. P. B. Radha, T. J. B. Collins, J. A. Delettrez, Y. Elbaz, R. Epstein, V. Yu. Glebov, V. N. Goncharov, R. L. Keck, J. P. Knauer, J. A. Marozas, F. J. Marshall, R. L. McCrory, P. W. McKenty, D. D. Meyerhofer, S. P. Regan, T. C. Sangster, W. Seka, D. Shvarts, S. Skupsky, Y. Srebro, and C. Stoeckl, Phys. Plasmas **12**, 056307 (2005).

29. C. D. Zhou and R. Betti, Phys. Plasmas **14**, 072703 (2007).

30. T. R. Boehly, E. Vianello, J. E. Miller, R. S. Craxton, T. J. B. Collins, V. N. Goncharov, I. V. Igumenshchev, D. D. Meyerhofer, D. G. Hicks, P. M. Celliers, and G. W. Collins, Phys. Plasmas **13**, 056303 (2006).

31. A. Sunahara, J. A. Delettrez, C. Stoeckl, R. W. Short, and S. Skupsky, Phys. Rev. Lett. **91**, 095003 (2003).

32. V. N. Goncharov, O. V. Gotchev, E. Vianello, T. R. Boehly, J. P. Knauer, P. W. McKenty, P. B. Radha, S. P. Regan, T. C. Sangster, S. Skupsky, V. A. Smalyuk, R. Betti, R. L. McCrory, D. D. Meyerhofer, and C. Cherfils-Clérouin, Phys. Plasmas **13**, 012702 (2006).

33. P. B. Radha, V. Yu. Glebov, V. N. Goncharov, D. D. Meyerhofer, T. C. Sangster, S. Skupsky, J. A. Frenje, and R. D. Petrasso, Bull. Am. Phys. Soc. **51**, 106 (2006).

34. P. D. Roberts *et al.*, J. Phys. D **13**, 1957 (1980).

35. T. C. Sangster, V. N. Goncharov, P. B. Radha, V. A. Smalyuk, R. Betti, R. S. Craxton, J. A. Delettrez, D. H. Edgell, V. Yu. Glebov, D. R. Harding, D. Jacobs-Perkins, J. P. Knauer, F. J. Marshall, R. L. McCrory, P. W. McKenty, D. D. Meyerhofer, S. P. Regan, W. Seka, R. W. Short, S. Skupsky, J. M. Soures, C. Stoeckl, B. Yaakobi, D. Shvarts, J. A. Frenje, C. K. Li, R. D. Petrasso, and F. H. Séguin, "High-Areal-Density Fuel Assembly in Direct-Drive Cryogenic Implosions," submitted to Physical Review Letters.

36. J. D. Moody *et al.*, Phys. Rev. Lett. **86**, 2810 (2001).

37. C. Stoeckl, R. E. Bahr, B. Yaakobi, W. Seka, S. P. Regan, R. S. Craxton, J. A. Delettrez, R. W. Short, J. Myatt, A. V. Maximov, and H. Baldis, Phys. Rev. Lett. **90**, 235002 (2003).

Time-Resolved Absorption in Cryogenic and Room-Temperature, Direct-Drive Implosions

Introduction

Absorption of laser light in laser inertial confinement fusion (ICF) implosion experiments[1–4] is of pre-eminent importance since it provides the energy input. Current ICF implosions are scaled from future ignition experiments with thermonuclear gain and typically require laser pulses of complex temporal shape. These pulse shapes are chosen—among other considerations—to minimize the growth of hydrodynamic instabilities in the acceleration phase of the implosion.[5,6] They drive an optimized series of shock and compression waves that coalesce in the fuel and lead to hot-spot ignition, provided the fuel has been kept at a low adiabat α (α = minimum fuel pressure over Fermi-degenerate pressure).

An accurate understanding of the coupling of laser light to the target is essential for the success of implosion experiments. The laser light can be refracted, scattered, and absorbed. Hydrodynamic simulations are used to optimize the pulse shapes for specific target designs.[7–11] These simulations indicate that the scattered-light distribution in 60-beam implosion experiments is isotropic to within 1% or 2%. Experimental measurements of the laser light scattered into 4π strad are used to infer the absorption for comparison with hydrodynamic simulations.

Current implosion experiments on OMEGA are designed to study various parameters including the hydrodynamic stability of the implosion. The absorption of laser light crucially influences the hydrodynamics. All phases of laser absorption, refraction, and scattering in current experiments will be encountered in the early phases of future ignition experiments. Some potential problems of future ignition experiments cannot be fully investigated at present. The longer scale lengths that will be encountered in the future may favor nonlinear interaction processes beyond those in current implosion experiments[12] or dedicated long-scale-length planar interaction experiments.[13–16]

Time-integrated absorption measurements have been previously reported for direct-drive spherical target experiments.[2,4,17–21] Time-integrated measurements can mask differences in the time evolution of the absorption that can lead to significant hydrodynamic consequences, such as shock mistiming and an increased adiabat of the inner shell surface of the imploding target. This article describes the experimental conditions, followed by examples of time-resolved scattered-light measurements in implosion experiments and a discussion of the underlying absorption processes. Conclusions are also presented.

Experimental Conditions

The OMEGA Laser System[22] operating with 60 UV beams (λ_L = 351 nm) irradiates cryogenic and room-temperature targets of ~860-μm diameter. Total laser energies are ≤24 kJ in laser pulses of ≤4 ns with shapes with or without 100-ps pickets ahead of the main pulse. The maximum overlapped irradiation intensity is 1.5×10^{15} W/cm^2. All beams are equipped with distributed phase plates (DPP's),[23–25] polarization smoothing (PS),[26] and smoothing by spectral dispersion (SSD)[27] in most experiments. The energy irradiation nonuniformity on target is <3% rms with each of the 60 beams slightly overfilling the target with ~5% energy spillover around the cold target. The intensity nonuniformity on target during the slowly varying parts of the pulse shape ranges between 3% and 7% when averaged over 200 to 300 ps. In the rapidly varying parts of the pulse shape the intensity nonuniformity is more difficult to quantify since it depends on pulse-shape irregularities, timing jitter among beams, and the precision and accuracy of the pulse-shape measurements for each beam. The intensity nonuniformity during the rapidly varying parts of the pulse shapes is estimated to be ≤15% rms.

The cryogenic targets[28] are plastic (CD) shells of ~860-μm diameter and 3- to 10-μm wall thickness filled with ~1000 atm of DT or D_2 and cooled and frozen into uniform,[29,30] ~100-μm solid DT or D_2 "ice" layers at ~18 K. The room-temperature targets are either CH or CD shells with walls of 10 to 40 μm filled with D_2 or DT gas (3 to 40 atm). The room-temperature targets are coated with ~100 nm of Al for gas retention. Gas diffusion at cryogenic temperatures is negligible and no Al coating is applied.

The principal diagnostic for determining laser absorption in these implosion experiments is provided by two full-aperture backscattering stations (FABS) located in beams 25 and 30.[4,18,31] Time-resolved scattered-light spectroscopy and time-integrated calorimetry in these stations are used to infer the absorption of light by the target. The absolutely calibrated FABS calorimeters provide cross-calibration for all time-resolved scattered-light spectra. A schematic of the diagnostic arrangement is shown in Fig. 113.36(a) along with typical time-resolved scattered-light spectra for a narrowband (no SSD bandwidth), 1-ns, room-temperature implosion.

There are four spectrally and time-resolved scattered-light–measurement channels[31] (one channel in each FABS and two channels located between focusing lenses). Two typical time-resolved scattered-light spectra are shown in Figs. 113.36(b) and 113.36(c) with no SSD bandwidth applied. The temporal resolution is ~80 ps and the spectral resolution is ~0.08 nm.

The calorimeters are calibrated using shots through the target chamber without a target, yielding absolute errors on the energy measurements of 1% to 3% at ~10 J into the focusing lenses of beam 25 or 30. The detection threshold for these calorimeters is ~0.04 J. For a typical 20-kJ implosion with ~50% absorption, this results in a calorimetry precision of ~1.5%. In the implosion experiments, the calorimeter measurements vary by 4% to 6%, leading to typical errors on the absorption of ~2% to 3%. These errors are about twice as large as expected but the source of these errors is not well understood at present. In addition to the FABS calorimeters, there are up to 17 scattered-light calorimeters located inside and outside of the target chamber. These calorimeters are cross-calibrated to the FABS calorimeters since absolute calibration of these calorimeters has proven to be very difficult to ascertain and maintain.

Near isotropy of the scattered light is predicted by hydrodynamic simulations. The schematic ray trace in Fig. 113.36(a) shows a variety of scattered ray paths that contribute to the FABS calorimeter and streak camera channels. This figure is greatly simplified as each point on each lens receives rays from many different directions and each FABS sees contributions from all 60 beams. The fractional contributions from each beam vary with time and beam. Since the FABS stations are in the line of sight of opposing beams, some light passes around the targets at early times [unshifted signal in Fig. 113.36(b)] and contributes to the FABS energy measurements. This "blow-by" is not isotropic and must be subtracted from the scattered-light measurements before the isotropically scattered-light energy

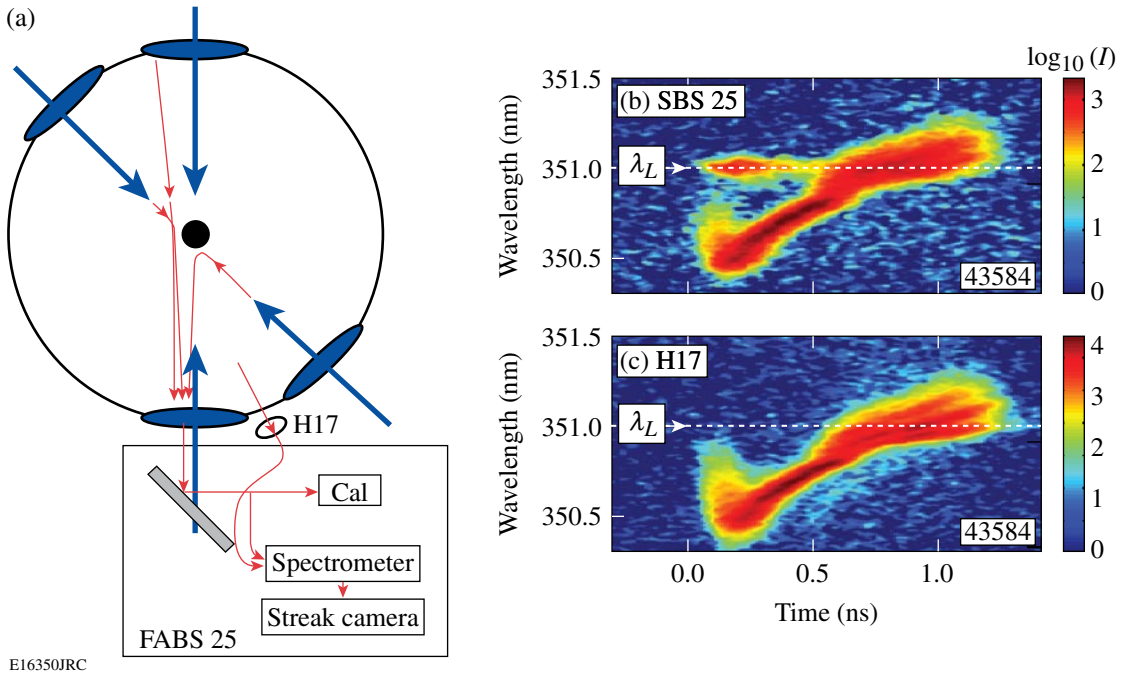

Figure 113.36
(a) Schematic of scattered-light diagnostics inside the OMEGA target chamber. The full-aperture backscatter station (FABS) is shown for beam 25 with its calorimeter and temporally and spectrally resolved backscatter channel. An additional channel for light scattered in between the focusing lenses is also shown (H17). Typical time-resolved backscatter spectra are shown in (b) for the FABS channel and (c) for the channel in between the focusing lenses for an imploding 20-μm-thick CH shell with DPP's and PS but no SSD bandwidth.

can be determined. This is done using target shots with only the beams opposing the two FABS stations. Since plasma formation on the limb of the target is minimal in this case, this measurement provides an upper limit of the blow-by. For consistency the two beams opposing the FABS can be turned off, which only minimally affects the FABS energy measurements for 58-beam shots but totally eliminates the need for blow-by corrections.

The two spectra shown in Fig. 113.36 clearly distinguish light that misses the target (blow-by) as it remains unshifted in wavelength [Fig. 113.36(b)]. For shots without beams opposing the FABS stations, the two spectra are practically indistinguishable. The time-resolved spectrum [Fig. 113.36(b)] allows for quantitative estimates of the blow-by, supporting the calorimetric estimates discussed above. The blow-by fraction depends on the pulse shape, pulse duration, and target and cannot be reasonably determined for all conditions. An estimated blow-by fraction of ~1.6% of the opposing beam energy is subtracted from the FABS calorimeter measurement to determine the diffusely scattered-light energy.

Results

Time-resolved scattered-light spectra are shown in Fig. 113.36 for a 1-ns square pulse implosion experiment and in Fig. 113.37(a) for an implosion using a complex pulse shape with 1-THz SSD bandwidth. The scattered-light power, obtained by integrating the spectra over the wavelength, is compared to predictions from hydrodynamic (*LILAC*[32]) simulations in Fig. 113.37(b). (Experimental time-resolved absorption fractions are not compared directly with simulations since the laser pulse shape and scattered-light spectra are recorded with different streak cameras and slight inaccuracies can lead to large errors upon division of one by the other.) To avoid the need for detailed blow-by corrections, the spectra taken in between the focusing lenses (e.g., H17) are used for most of the quantitative analyses. Two *LILAC* predictions for the scattered-light power are shown in Fig. 113.37(b), one for standard flux-limited electron-heat transport with $f = 0.06$ (Ref. 33) and the second using a nonlocal heat-transport model developed at LLE.[34,35] The differences between the experimental observations and the *LILAC* predictions apparent in Fig. 113.37(b) are typical for these experiments but the details differ depending on target and irradiation parameters.

The scattered-light spectra in Figs. 113.36 and 113.37 exhibit a similar rapid blue shift followed by a slow return to the initial laser wavelength and beyond. The spectra are modeled using ray-trace simulations based on density, velocity, and temperature profiles obtained from hydrodynamic (*LILAC*) simulations. Figure 113.38 shows schematically how all 60 beams of OMEGA contribute to the scattered light collected at any location. The contributions from each beam vary in time. The spectral shifts observed in Figs. 113.36 and 113.37 are due to the plasma evolution,[36] i.e., the temporally changing optical path length in the plasma traversed by any ray.

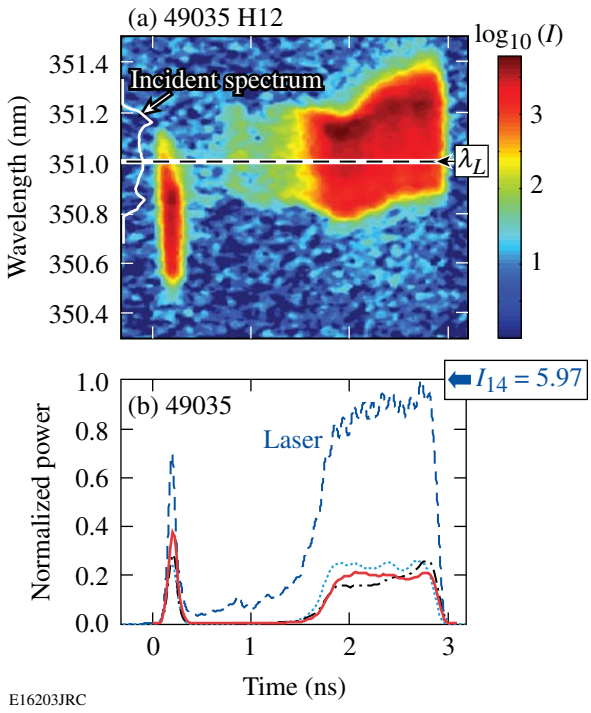

Figure 113.37
(a) Scattered-light spectrum and (b) incident and scattered-light powers for a cryogenic target (10-μm CH wall, 77-μm DT-ice layer, 858-μm diam) imploded with 17.7 kJ of fully smoothed laser energy (DPP's, PS, and 1-THz SSD bandwidth). The experimental scattered power is shown by the dotted line, the incident power by dashed lines, and *LILAC* predictions with nonlocal and flux-limited transport by solid and dashed–dotted lines, respectively.

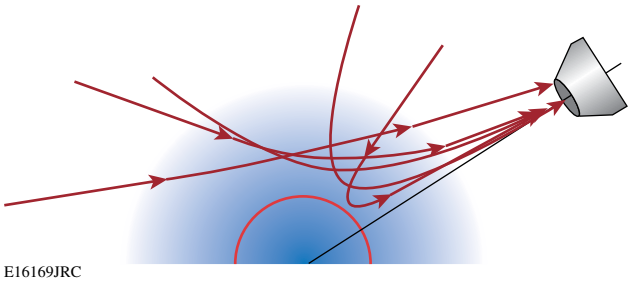

Figure 113.38
Illustration of scattered-light contributions from any of OMEGA's 60 beams to the light collected by a lens at the target chamber wall. The contributions from any one beam depend on both time and the position of the beam relative to the collector.

The experimental and simulated spectra are compared in Fig. 113.39 for a target irradiated with a 200-ps laser pulse without SSD corresponding to the picket shown in Fig. 113.37. For this narrowband experiment the anisotropic blow-by contribution to the scattered light observed in FABS25 is easily distinguished from the light that is isotropically scattered by the plasma. Simulations with the nonlocal electron-heat transport and the standard flux-limited transport are shown in Figs.113.39(b) and 113.39(c) with Fig.113.39(b) matching the experimental data better. The simulations include the blow-by around the target. The corresponding incident and scattered-light powers are shown in Fig. 113.40, where the blow-by has been removed from the spectrum. Excellent agreement between simulations using nonlocal transport and experimental data is apparent in this figure. The time-integrated absorption fraction for a number of 200-ps irradiation experiments is shown in Fig. 113.41. The agreement between the *LILAC* predictions using nonlocal transport is apparent from these figures, whereas the standard flux-limited transport significantly underestimates the absorption.

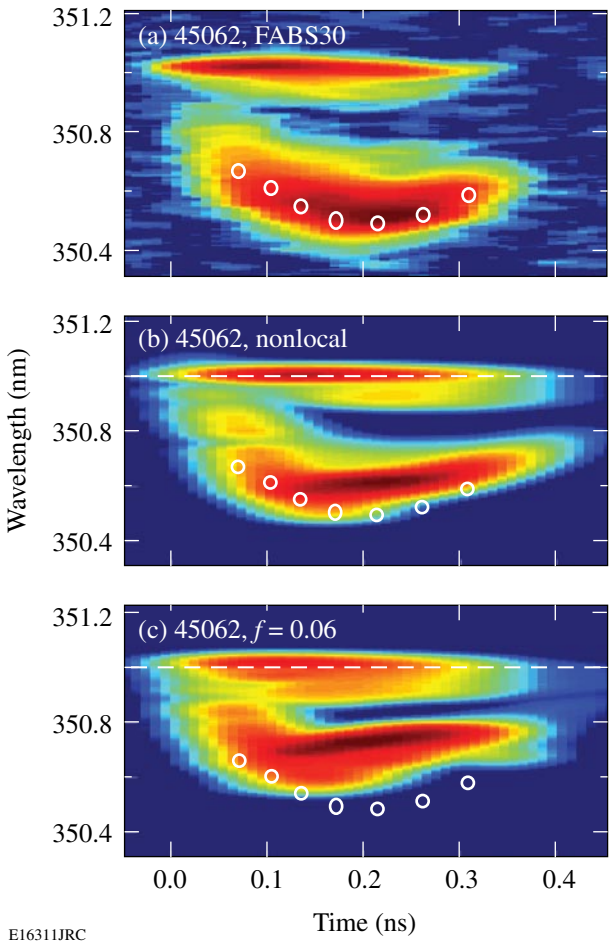

Figure 113.39
Time-resolved scattered-light spectra for a 200-ps spherical irradiation experiment of a warm 20-μm CH shell with DPP's and PS but no SSD bandwidth. The experimental spectrum is shown in (a) and two simulated spectra are shown in (b) and (c). Nonlocal electron-heat transport was used for the plasma parameters in (b) and standard flux-limited ($f = 0.06$) heat transport was used in (c). The white circles are added for easier comparison of the simulated spectra with the experimental spectrum.

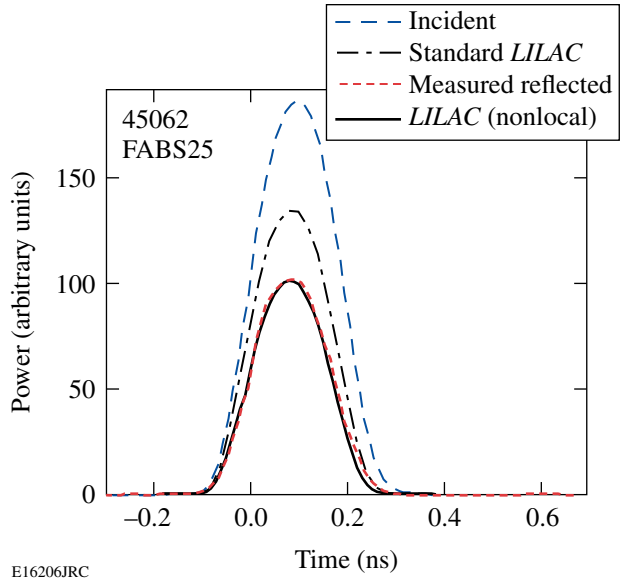

Figure 113.40
Power histories of the incident and scattered light for the spectra shown in Fig. 113.39: the measured scattered-light power (short-dashed line), the incident power (long-dashed line), the predictions based on nonlocal transport (solid line), and standard *LILAC* predictions using flux-limited heat transport with $f = 0.06$ (dashed–dotted line).

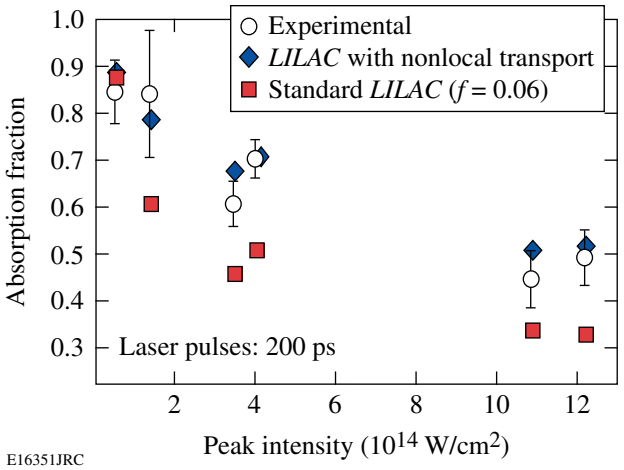

Figure 113.41
The time-integrated absorption fractions for 200-ps irradiation experiments of CH targets (20-μm shells or solid spheres) with DPP's and PS. Most shots were without SSD bandwidth while two shots had 1-THz SSD bandwidth.

As shown in Fig. 113.37, hydrodynamic simulations using either flux-limited or nonlocal transport cannot accurately predict the scattered-light power at later times during the main part of the compression pulse ($t > 1.5$ ns in Fig. 113.37). A particularly striking example is shown in Fig. 113.42 where a warm plastic shell (20-μm CH wall, 873-μm diam) was imploded with a 1-ns square pulse, full beam smoothing, and 15.3-kJ laser energy. Instantaneously, the scattered-light spectra differ significantly from the incident spectrum as is evident from the lineouts in Fig. 113.42(a). The scattered-light power predicted by *LILAC* using constant flux-limited thermal transport significantly over-predicts the scattered power during the first half of the pulse and then under-predicts it during the latter half. Simulations using nonlocal transport correctly estimate the scattered power during the first 150 ps but are consistently too low beyond that. The differences between the incident and scattered-light spectra [see lineouts in Fig. 113.42(a)] are indicative of a nonlinear interaction process as will be discussed on p. 43.

Another example of the measured and simulated scattered-light spectrum is shown in Fig. 113.43 for a cryogenic target implosion with a complex laser pulse designed to drive the target on a low fuel adiabat ($\alpha = 2$). Hydrodynamic simulations

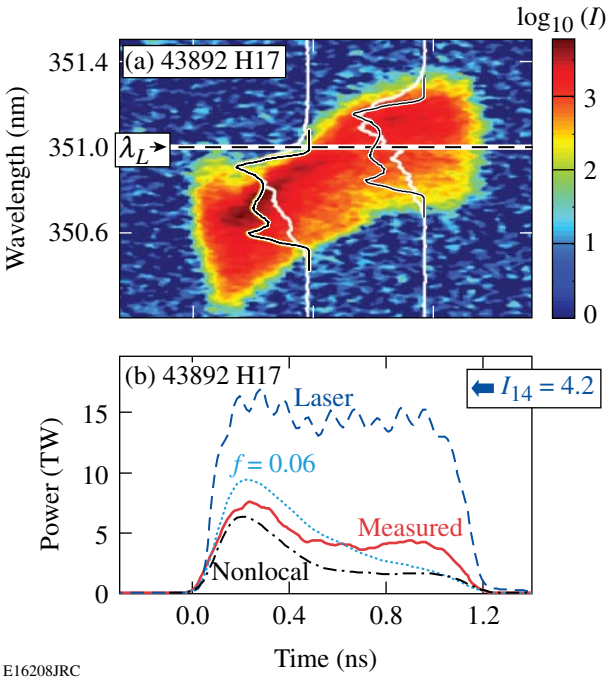

Figure 113.42
(a) Scattered-light spectrum and (b) incident, measured, and predicted scattered-light powers for a room-temperature target (20-μm CH wall, 873-μm diam, 15 atm of D_2) imploded with a 1-ns laser pulse of 15.3-kJ energy with full beam smoothing (DPP's and PS, 1-THz SSD bandwidth). Lineouts of the spectrum shown in (a) are in white with the incident spectrum superposed in black-on-white. In (b) the measured scattered-light power is shown as a solid line, *LILAC* predictions using standard flux-limited electron transport with $f = 0.06$ are shown as a dotted line, and those with nonlocal transport are shown as a dashed–dotted line.

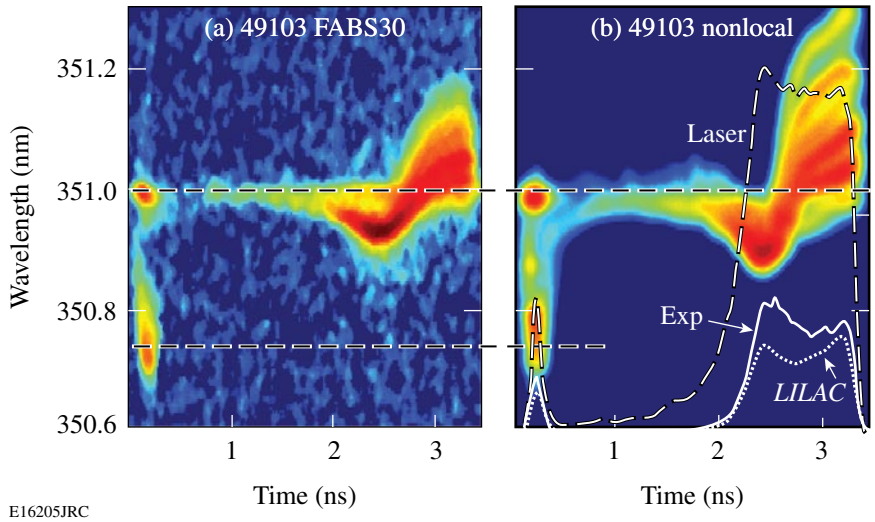

Figure 113.43
(a) Measured and (b) simulated time-resolved scattered-light spectra for an imploding cryogenic target (10-μm CD wall, 95-μm D_2-ice layer, 855-μm diam) with 16 kJ of laser energy smoothed with DPP's and PS but no SSD bandwidth. The laser pulse shape is shown as white dashes in (b) along with the measured (solid white) and simulated (dotted white) scattered-light powers. The hydrodynamic simulations used nonlocal electron transport. (For details of comparison see the **Discussion** section, p. 43.)

with nonlocal transport were used to calculate the simulated spectrum [Fig. 113.43(b)]. The general shape of the simulated spectrum is close to that measured. The incident laser power is shown in Fig. 113.43(b) along with the measured and predicted scattered laser power.

In addition to light scattered near the incident laser wavelength, laser light is scattered into half-harmonics ($\omega/2$ and $3\omega/2$) due to the two-plasmon-decay (TPD) instability. Stimulated Raman scattering (SRS)[37] has never been observed on OMEGA direct-drive-implosion experiments while half-harmonic spectra are regularly observed on OMEGA. The plasma waves produced by the TPD instability can generate energetic electrons leading to emission of hard x rays beyond 50 keV. Various scattered-light spectra and powers observed during a typical room-temperature implosion experiment are shown in Fig. 113.44. The wavelength scales of the half-harmonic spectra are chosen to have equal frequency (energy) scales for convenient comparison of the spectral features that are indicative of the TPD instability.

The half-harmonic and hard x-ray emission are superposed in Fig. 113.44(d). The power histories (two half-harmonics and hard x rays) are strikingly similar, suggesting their common TPD origin. Under well-controlled irradiation conditions (similar targets, same pulse shapes, but different intensities) the half-harmonic and hard x-ray signals exhibit an essentially identical exponential scaling with intensity (Fig. 113.45). An x-ray threshold around 4 to 5×10^{14} W/cm^2 is observed in Fig. 113.45. The half-harmonic emission has a threshold that is around 2×10^{14} W/cm^2, comparable to the theoretical threshold[38] as calculated for the average intensity in an equivalent linear density gradient for plane waves at normal incidence.

The intricate dependence of the TPD threshold to the density-gradient scale length (L_n), electron temperature (T_e), and intensity is seen in Fig. 113.46. A rough estimate for the TPD threshold is provided by the plane wave, linear-gradient-threshold parameter[38] $\alpha_{th} = I_{14} L_{n,\mu m} / 230\, T_{e,keV} > 1$, where I_{14} is the average intensity on target in units of 10^{14} W/cm^2. The laser burns through the plastic shell of this cryogenic target around the dip of the α_{th}-curve in Fig. 113.46(b). It should also be noted that the instantaneous peak intensities on target are typically 5× larger than the average intensities.

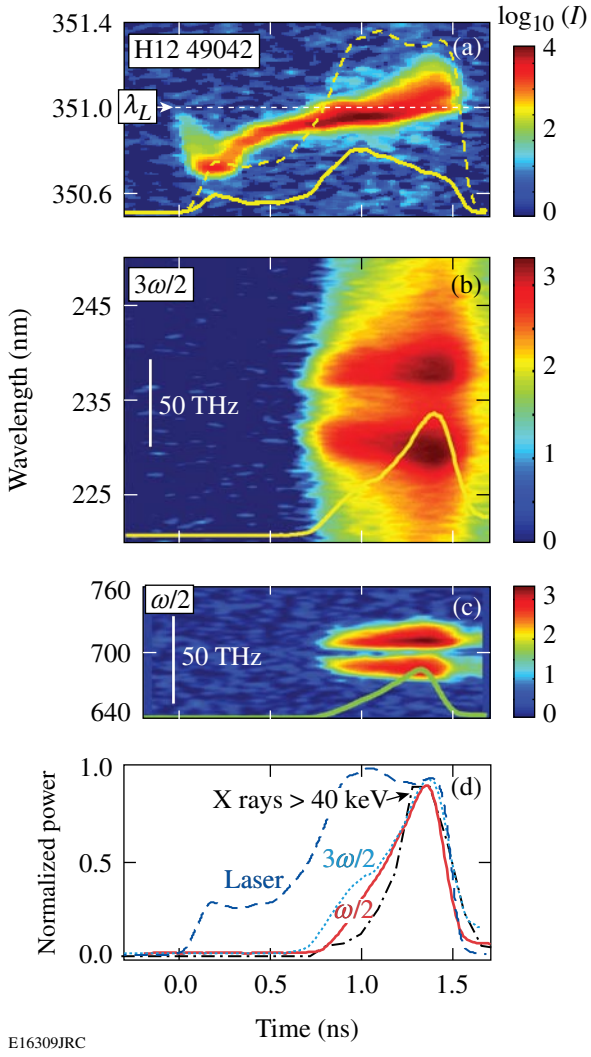

Figure 113.44
Time-resolved scattered-light spectra for a room-temperature implosion using 25 kJ of laser energy with DPP and PS smoothing but no SSD bandwidth. [Target: plastic shell, 24-μm wall, outer 10 μm are doped with 6% (atomic) Si, filled with 15 atm of D_2.] The spectrum of the scattered light around the laser frequency and the incident and scattered power are shown in (a). In (b) and (c) the $3\omega/2$ and $\omega/2$ spectra and powers are shown on a common frequency (energy) scale. The normalized incident laser, odd-integer half-harmonic powers, and the time-resolved x-ray emission for $h\nu_x > 40$ keV are shown in (d).

Discussion

While time-integrated absorption measurements have been previously reported to be in good agreement with simulations,[4,21,39] the data presented here show the value of time-resolved data since compensating differences between experimental data and predictions can lead to erroneous interpretations. Time-resolved spectral measurements show a high sensitivity to the actual drive intensity on target. Time-resolved spectral measurements are particularly important for determining the hydrodynamic wave timing in the ignition-scaled experiments with complex pulse shapes presently carried out on OMEGA.

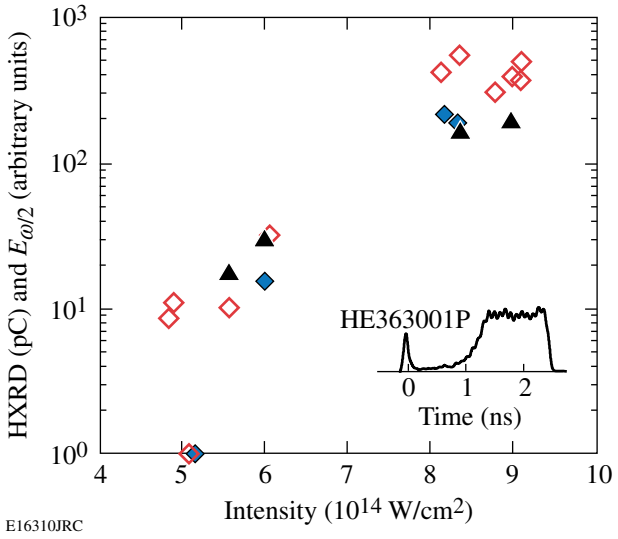

Figure 113.45
Intensity scaling of hard x rays (open and solid diamonds, $h\nu_x > 40$ keV) and the half-harmonic emission (solid triangles) for cryogenic shots with pulse shapes as shown in the insert. The targets were 10-μm CH or CD shells with a 95-μm D_2- or DT-ice layer. Shots with pure CD or CH shells are shown as open diamonds; those with Si-doped outer layers (5 μm) are shown as solid diamonds.

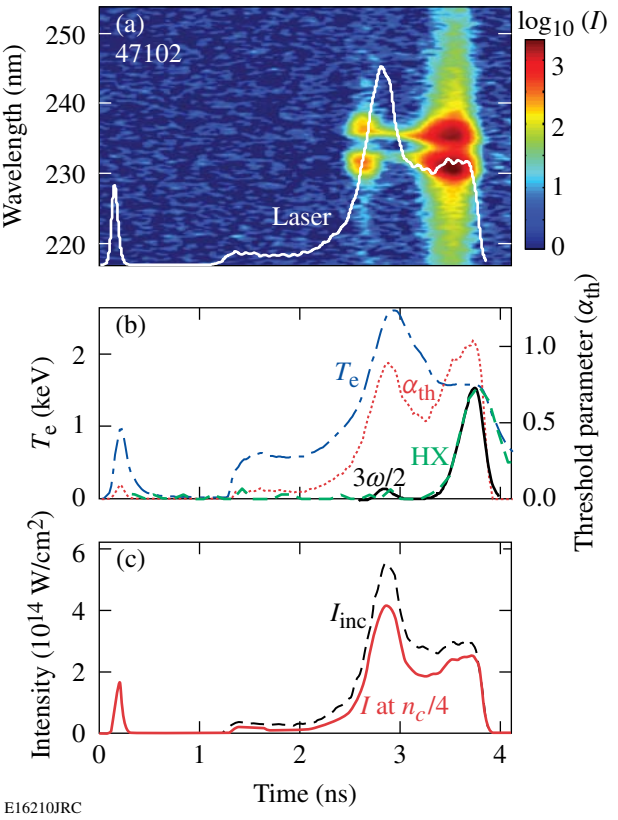

Figure 113.46
Spectrum of the 3/2-harmonic emission (a) from a cryogenic target (4.5-μm CH shell and 95-μm D_2 ice layer) imploded with 11.7 kJ of laser energy and full beam smoothing (DPP, PS, and 1-THz SSD bandwidth). *LILAC* predictions for T_e and α_{th} are shown in (b). Also, shown in (b) are the normalized 3/2-harmonic and hard x-ray powers. (The extended hard x-ray emission is an artifact of the cryogenic target implosion and does not relate to extended fast electron production.) In (c) the incident intensity and the intensity at $n_c/4$ are shown. The thin CH shell burns through at ~3.2 ns.

Discrepancies between the hydrodynamic predictions and experimental scattered-light data as shown in Fig. 113.37(b) are common. The initial spike of the incident laser pulse is typically more strongly absorbed than predicted by simulations using standard flux-limited electron-heat transport [dashed–dotted line in Fig. 113.37(b)]. In contrast, the *LILAC* prediction using nonlinear electron-heat transport is in excellent agreement for the scattered light of the initial spike. At later times (between 2 and 3 ns in Fig. 113.37) the experimental data tend to be predicted better using flux-limited electron transport. Both transport models consistently predict less scattered light than is observed.

The scattered-light spectra (Figs. 113.36, 113.37, 113.39, 113.42, and 113.43) contain a wealth of information about the plasma evolution and the laser–plasma interaction processes. Refraction in the plasma deflects part of all 60 beams of OMEGA into the collection optics as shown schematically in Fig. 113.38. The exact contribution of any beam varies in time and with the position of the beam relative to the collection optics. This is simulated numerically with a ray-trace code using the time-varying plasma profiles obtained from one-dimensional *LILAC* simulations.[40] These simulations show that the rapid blue shift during the initial irradiation of the target is due to the buildup of plasma[36] that occurs when the optical path length traversed by the scattered light decreases rapidly with time, since the index of refraction in the plasma is $\mu = \left(1 - n_e/n_c\right)^{1/2} < 1$, where n_e and n_c are the electron density and critical electron density. These ray-trace simulations show that the scattered light shifts to the blue whenever the mass ablation rate increases.

The remarkable sensitivity of the scattered-light spectra on the electron-heat-transport model used in the hydrodynamic simulations is shown in Fig. 113.39. For this narrowband shot (no SSD bandwidth) we note that the simulations reproduce both the refracted spectrum and the "blow-by" spectrum (the

small part of the laser beam opposing the FABS that misses the target entirely and is seen only when viewing the target through one of the focusing lenses). The experimental spectrum [Fig. 113.39(a)] is better (though not perfectly) matched by the simulations using nonlocal electron-heat transport [Fig. 113.39(b)] than by the standard flux-limited heat transport with $f = 0.06$ [Fig. 113.39(c)]. Figure 113.40 also shows much better agreement between observed and simulated scattered-light power with the nonlocal heat-transport model. The improved predictability of the hydrodynamic simulations for picket pulses is evident in the time-integrated absorption fractions for the 200-ps experiments shown in Fig. 113.41.

Obtaining accurate hydrodynamic simulations of these short-pulse experiments is crucial since the initial spikes in these ignition-relevant pulse shapes (Figs. 113.37, 113.42, 113.45, and 113.46) are intended to shape the adiabat of the implosion.[10]

The scattered laser power is generally underpredicted by *LILAC* during the main part of the laser pulse (see Figs. 113.37, 113.42, and 113.43). The scattered-light spectrum in Fig. 113.42 (20-μm CH shell, 1-ns square pulse, 1-THz SSD) shows a change from the symmetrical, incident SSD spectrum to one that is red peaked (see lineouts in Fig. 113.42). This change is evidence for nonlinear scattering in the plasma corona such as stimulated Brillouin scattering (SBS) with a strong electromagnetic (EM) seed.[15] Intrabeam forward SBS, where scattering of the blue spectrum seeds SBS in the red of the same beam, would be expected to give rise to a red-peaked spectrum with negligible net energy loss. In contrast, cross-beam energy transfer has been shown in planar geometry to be very effective[15,41] and can lead to significant loss of drive energy. The effects seen in spherical geometry are difficult to reproduce in planar geometry with its restricted number of beam angles. The multitude of contributing beams and varying beam paths render it difficult to numerically model these effects in spherical geometry. The enhanced scattering at later times tends to be less detrimental to a low-adiabat implosion than the increased absorption during the early phase of plasma formation that is better modeled using the nonlocal model.

The potential significance of the cross-beam energy transfer is seen in Fig. 113.43 for an implosion experiment without SSD bandwidth. The scattered light during the picket is well reproduced in spectrum and power by the simulations using nonlocal transport. In contrast, significant differences are observed between the experimental and simulated spectra and powers starting with the intensity rise to the main pulse. The simulated spectrum predicts a larger blue shift than is observed. As mentioned previously, ray-trace simulations indicate that an increasing mass ablation rate leads to an increasing blue shift. The observed time-resolved spectrum in Fig. 113.43 indicates that there is less drive pressure at the onset of the main pulse than predicted, consistent with the observed increased scattered-light power at that time. The simulated spectrum in Fig. 113.43 between 2 and 3.3 ns shows two strongly red-shifted components not seen in the experimental data. These components are due to light rays with the closest approach to the critical surface; they also are the most intense rays in each beam and provide the most efficient drive. It is plausible that their absence indicates a loss due to cross-beam energy transfer. (Increased absorption for these rays could explain the absence of these red components but would be inconsistent with the reduced drive deduced from the reduced blue shift of the spectrum and the observed increased scattered-light power.) It should be noted that these detailed features of the spectra are only visible without SSD bandwidth as a 1-THz SSD bandwidth completely washes out these details.

The scattered-light spectra at various wavelengths are shown in Fig. 113.44 for a room-temperature, low-adiabat ($\alpha = 3$), narrowband (no SSD bandwidth) implosion. The outer 5 μm of this target are doped with 6% atomic Si in an effort to reduce hard x-ray production. Figures 113.44(a)–113.44(c) show the spectra and powers of the scattered light near the incident laser wavelength and the odd-integer half-harmonics. The wavelength scales of the $\omega/2$ and $3\omega/2$ spectra are chosen to have equal frequency scales. The existence of these odd-integer half-harmonic spectra is compelling evidence for the TPD instability,[2,13] while the separation of the two peaks reflects the different secondary scattering processes involved.[42]

The half-harmonic spectrum in Fig. 113.44(c) is consistent with plasmon-to-photon mode conversion[42] analogous to the conversion process underlying resonance absorption.[43] The red component of this spectrum is stronger since the lower-frequency TPD plasmon can convert near the point of its creation while the higher-frequency (blue) plasmon has to propagate to its turning point before conversion. The spectral splitting is consistent with linear TPD theory.[38]

The 3/2-harmonic emission [Fig. 113.44(b)] is due to Thomson scattering of incident photons off TPD plasmons. In spherical geometry, the relevant phase-matching conditions are easily satisfied due to the large number of available probe rays for Thomson scattering. This explains why the blue peak of the 3/2-harmonic spectrum tends to be more intense than the red peak since the phase-matching conditions

can be satisfied for the blue plasmon at its point of creation. For the red 3/2-harmonic component, the phase-matching conditions require that the red plasmon propagate down the density gradient and acquire the requisite k-vector length for Thomson scattering.[42]

Given these differences in the generation processes for the odd-integer half-harmonic emissions, it is surprising that their power histories are nearly identical, as seen in Fig. 113.44(d). It is equally surprising that the temporal hard x-ray emission follows the half-harmonic emission as shown in Fig. 113.44(d). This is probably a consequence of the extremely rapid growth of the TPD instability, which is followed by saturation.

The exponential scaling of the hard x-ray and half-harmonic emission with laser intensity is shown in Fig. 113.45. This kind of scaling is observed only if the target and pulse shapes are kept constant while the intensity alone is varied. Changing either the pulse shape or the target causes the simple scaling to break down. In particular, doping the outer layers of the target with high-Z elements (Si or Ge) reduces the hard x-ray emission while affecting the half-harmonics to a lesser extent.[44] The underlying cause for these changes can be partly attributed to changes in density scale length, electron temperature, and absorption of the incident light on the way to $n_c/4$. However, a Z-dependence in the saturation mechanisms for the TPD instability cannot be ruled out.

The TPD threshold (and presumably also its saturation) dependence on density scale length, electron temperature, and intensity is illustrated in Fig. 113.46. The 3/2-harmonic emission has an initial, weak burst at 2.8 ns before the peak of the laser pulse. Its main emission occurs at the end of the laser pulse when the laser intensity is only half of its peak value but the threshold parameter α_{th} is highest due to the reduced temperature. The fast-electron production also peaks at that time as indicated in Fig. 113.46(b). [The extended hard x-ray signal observed in Fig. 113.46(b) is consistently observed in cryogenic shots and is tentatively attributed to energetic electrons striking surfaces in the vicinity of the target that are present only during cryogenic shots.] As in room-temperature targets, the strong half-integer harmonic emission generally correlates well with the hard x-ray emission temporally. Weaker precursor half-integer harmonic emission is typically not reflected in the hard x-ray signals.

The threshold parameter α_{th} represents a simplified view of the actual experimental conditions, yet it appears to give useful insight into the threshold behavior (and possibly also its saturation behavior) of this instability. This instability is as ubiquitous for direct-drive laser-fusion experiments as it is intractable theoretically, particularly with regard to its ramifications of fast-electron generation and fast-electron preheat.

Conclusions

The spectra and powers of the scattered laser light during direct-drive ICF implosion experiments on OMEGA have been shown to be powerful tools for fine-tuning hydrodynamic code simulations and identifying laser–plasma interaction processes. Short pulses frequently precede the main laser pulse for adiabat shaping of the implosion. These pulses have been shown experimentally to have higher absorption than predicted by hydrodynamic code simulations using flux-limited diffusion. Comparisons of *LILAC* simulations with these experimental data have led to an improved nonlocal electron-transport model.

Later during target irradiation the scattered-light spectra and powers indicate the presence of enhanced scattering that reduces the laser drive of the target. The scattered-light spectra point to a nonlinear interaction process that is tentatively identified as EM-seeded SBS. The EM seed here is provided by the scattered light of any of the 60 beams of OMEGA and the required SBS gain is small. The spectra indicate that the increase in mass ablation during the rise of the main pulse is not as large as predicted by hydrodynamic simulations, supporting the reduced laser–plasma coupling observed in the power measurements.

The presence of the TPD instability is clearly seen in these direct-drive-implosion experiments through the emission of $\omega/2$ and $3\omega/2$ light as well as hard x rays above 50 keV. The sensitivity of the TPD instability to laser intensity, density-gradient scale lengths, and electron temperature has been identified using complex pulse shapes. Although there is no easily applicable theory for interpreting the details of the observation, the data obtained so far permit tailoring implosion experiments to minimize the detrimental effects of the energetic electron production associated with the TPD. In particular, doping of the outer plastic layers of the target with high-Z elements appears to mitigate hard x-ray production although the detailed mechanism is not well understood at present.

ACKNOWLEDGMENT

This work was supported by the U.S. Department of Energy Office of Inertial Confinement Fusion under Cooperative Agreement No. DE-FC52-08NA28302 and the University of Rochester. The support of DOE does not constitute an endorsement by DOE of the views expressed in this article.

REFERENCES

1. R. S. Craxton and R. L. McCrory, Laboratory for Laser Energetics, University of Rochester, Rochester, NY, LLE Report No. 108 (1980).
2. M. C. Richardson, R. S. Craxton, J. Delettrez, R. L. Keck, R. L. McCrory, W. Seka, and J. M. Soures, Phys. Rev. Lett. **54**, 1656 (1985).
3. R. Cauble and W. Rozmus, Phys. Fluids **28**, 3387 (1985).
4. W. Seka, C. Stoeckl, V. N. Goncharov, R. E. Bahr, T. C. Sangster, R. S. Craxton, J. A. Delettrez, A. V. Maximov, J. Myatt, A. Simon, and R. W. Short, Bull. Am. Phys. Soc. **49**, 179 (2004).
5. P. W. McKenty, J. A. Marozas, V. N. Goncharov, K. S. Anderson, R. Betti, D. D. Meyerhofer, P. B. Radha, T. C. Sangster, S. Skupsky, and R. L. McCrory, Bull. Am. Phys. Soc. **51**, 295 (2006).
6. P. W. McKenty, T. C. Sangster, M. Alexander, R. Betti, R. S. Craxton, J. A. Delettrez, L. Elasky, R. Epstein, A. Frank, V. Yu. Glebov, V. N. Goncharov, D. R. Harding, S. Jin, J. P. Knauer, R. L. Keck, S. J. Loucks, L. D. Lund, R. L. McCrory, F. J. Marshall, D. D. Meyerhofer, S. P. Regan, P. B. Radha, S. Roberts, W. Seka, S. Skupsky, V. A. Smalyuk, J. M. Soures, K. A. Thorp, M. Wozniak, J. A. Frenje, C. K. Li, R. D. Petrasso, F. H. Séguin, K. A. Fletcher, S. Padalino, C. Freeman, N. Izumi, J. A. Koch, R. A. Lerche, M. J. Moran, T. W. Phillips, G. J. Schmid, and C. Sorce, Phys. Plasmas **11**, 2790 (2004).
7. V. N. Goncharov, P. McKenty, S. Skupsky, R. Betti, R. L. McCrory, and C. Cherfils-Clérouin, Phys. Plasmas **7**, 5118 (2000).
8. R. L. McCrory, R. E. Bahr, T. R. Boehly, T. J. B. Collins, R. S. Craxton, J. A. Delettrez, W. R. Donaldson, R. Epstein, V. N. Goncharov, R. Q. Gram, D. R. Harding, P. A. Jaanimagi, R. L. Keck, J. P. Knauer, S. J. Loucks, F. J. Marshall, P. W. McKenty, D. D. Meyerhofer, S. F. B. Morse, O. V. Gotchev, P. B. Radha, S. P. Regan, W. Seka, S. Skupsky, V. A. Smalyuk, J. M. Soures, C. Stoeckl, R. P. J. Town, M. D. Wittman, B. Yaakobi, J. D. Zuegel, R. D. Petrasso, D. G. Hicks, and C. K. Li, in *Inertial Fusion Sciences and Applications 99*, edited by C. Labaune, W. J. Hogan, and K. A. Tanaka (Elsevier, Paris, 2000), pp. 43–53.
9. S. Skupsky, R. Betti, T. J. B. Collins, V. N. Goncharov, D. R. Harding, R. L. McCrory, P. W. McKenty, D. D. Meyerhofer, and R. P. J. Town, in *Inertial Fusion Sciences and Applications 2001*, edited by K. Tanaka, D. D. Meyerhofer, and J. Meyer-ter-Vehn (Elsevier, Paris, 2002), pp. 240–245.
10. V. N. Goncharov, J. P. Knauer, P. W. McKenty, P. B. Radha, T. C. Sangster, S. Skupsky, R. Betti, R. L. McCrory, and D. D. Meyerhofer, Phys. Plasmas **10**, 1906 (2003).
11. R. Betti, K. Anderson, T. R. Boehly, T. J. B. Collins, R. S. Craxton, J. A. Delettrez, D. H. Edgell, R. Epstein, V. Yu. Glebov, V. N. Goncharov, D. R. Harding, R. L. Keck, J. H. Kelly, J. P. Knauer, S. J. Loucks, J. A. Marozas, F. J. Marshall, A. V. Maximov, D. N. Maywar, R. L. McCrory, P. W. McKenty, D. D. Meyerhofer, J. Myatt, P. B. Radha, S. P. Regan, C. Ren, T. C. Sangster, W. Seka, S. Skupsky, A. A. Solodov, V. A. Smalyuk, J. M. Soures, C. Stoeckl, W. Theobald, B. Yaakobi, C. Zhou, J. D. Zuegel, J. A. Frenje, C. K. Li, R. D. Petrasso, and F. H. Séguin, Plasma Phys. Control. Fusion **48**, B153 (2006).
12. S. E. Bodner, D. G. Colombant, J. H. Gardner, R. H. Lehmberg, S. P. Obenschain, L. Phillips, A. J. Schmitt, J. D. Sethian, R. L. McCrory, W. Seka, C. P. Verdon, J. P. Knauer, B. B. Afeyan, and H. T. Powell, Phys. Plasmas **5**, 1901 (1998); J. Myatt, A. V. Maximov, W. Seka, R. S. Craxton, and R. W. Short, Phys. Plasmas **11**, 3394 (2004).
13. W. Seka, R. S. Craxton, R. E. Bahr, D. L. Brown, D. K. Bradley, P. A. Jaanimagi, B. Yaakobi, and R. Epstein, Phys. Fluids B **4**, 432 (1992).
14. W. Seka, R. S. Craxton, R. Bahr, D. Bradley, P. Jaanimagi, J. Knauer, S. Letzring, D. Meyerhofer, R. L. Short, A. Simon, and J. M. Soures, Bull. Am. Phys. Soc. **35**, 1944 (1990).
15. W. Seka, H. A. Baldis, J. Fuchs, S. P. Regan, D. D. Meyerhofer, C. Stoeckl, B. Yaakobi, R. S. Craxton, and R. W. Short, Phys. Rev. Lett. **89**, 175002 (2002).
16. W. Seka, R. E. Bahr, R. W. Short, A. Simon, R. S. Craxton, D. S. Montgomery, and A. E. Rubenchik, Phys. Fluids B **4**, 2232 (1992).
17. J. M. Soures, T. C. Bristow, H. Deckman, J. Delettrez, A. Entenberg, W. Friedman, J. Forsyth, Y. Gazit, G. Halpern, F. Kalk, S. Letzring, R. McCrory, D. Peiffer, J. Rizzo, W. Seka, S. Skupsky, E. Thorsos, B. Yaakobi, and T. Yamanaka, in *Laser Interaction and Related Plasma Phenomena*, edited by H. J. Schwarz, H. Hora, M. J. Lubin, and B. Yaakobi (Plenum Press, New York, 1981), Vol. 5, pp. 463–481.
18. W. Seka, R. S. Craxton, J. Delettrez, L. Goldman, R. Keck, R. L. McCrory, D. Shvarts, J. M. Soures, and R. Boni, Opt. Commun. **40**, 437 (1982).
19. W. Seka, L. M. Goldman, M. C. Richardson, J. M. Soures, K. Tanaka, B. Yaakobi, R. S. Craxton, R. L. McCrory, R. Short, E. A. Williams, T. Boehly, R. Keck, and R. Boni, in *Plasma Physics and Controlled Nuclear Fusion Research 1982* (IAEA, Vienna, 1983), Vol. I, pp. 131–137.
20. C. Garban-Labaune *et al.*, Phys. Fluids **28**, 2580 (1985).
21. S. P. Regan, H. Sawada, D. Li, V. N. Goncharov, R. Epstein, J. A. Delettrez, J. P. Knauer, J. A. Marozas, F. J. Marshall, R. L. McCrory, P. W. McKenty, D. D. Meyerhofer, P. B. Radha, W. Seka, T. C. Sangster, S. Skupsky, V. A. Smalyuk, R. Mancini, S. H. Glenzer, O. Landen, and G. Gregori, Bull. Am. Phys. Soc. **51**, 254 (2006).
22. T. R. Boehly, R. S. Craxton, T. H. Hinterman, P. A. Jaanimagi, R. L. Keck, J. H. Kelly, T. J. Kessler, R. L. Kremens, S. A. Kumpan, S. A. Letzring, R. L. McCrory, S. F. B. Morse, W. Seka, S. Skupsky, J. M. Soures, and C. P. Verdon, in *Proceedings of the IAEA Technical Committee Meeting on Drivers for Inertial Confinement Fusion*, edited by J. Coutant (IAEA, Vienna, 1995), pp. 79–86.
23. Kato *et al.*, Phys. Rev. Lett. **53**, 1057 (1984).
24. T. J. Kessler, Y. Lin, J. J. Armstrong, and B. Velazquez, in *Laser Coherence Control: Technology and Applications*, edited by H. T. Powell and T. J. Kessler (SPIE, Bellingham, WA, 1993), Vol. 1870, pp. 95–104.

25. T. J. Kessler, Y. Lin, L. S. Iwan, W. P. Castle, C. Kellogg, J. Barone, E. Kowaluk, A. W. Schmid, K. L. Marshall, D. J. Smith, A. L. Rigatti, J. Warner, and A. R. Staley, in *Second Annual International Conference Solid State Lasers for Application to Inertial Confinement Fusion*, edited by M. L. André (SPIE, Bellingham, WA, 1997), Vol. 3047, pp. 272–281.

26. J. E. Rothenberg, J. Appl. Phys. **87**, 3654 (2000).

27. S. Skupsky, R. W. Short, T. Kessler, R. S. Craxton, S. Letzring, and J. M. Soures, J. Appl. Phys. **66**, 3456 (1989).

28. D. R. Harding, D. D. Meyerhofer, S. J. Loucks, L. D. Lund, R. Janezic, L. M. Elasky, T. H. Hinterman, D. H. Edgell, W. Seka, M. D. Wittman, R. Q. Gram, D. Jacobs-Perkins, R. Early, T. Duffy, and M. J. Bonino, Phys. Plasmas **13**, 056316 (2006).

29. D. H. Edgell, W. Seka, R. S. Craxton, L. M. Elasky, D. R. Harding, R. L. Keck, and M. D. Wittman, Fusion Sci. Technol. **49**, 616 (2006).

30. D. H. Edgell, W. Seka, R. S. Craxton, L. M. Elasky, D. R. Harding, R. L. Keck, L. D. Lund, and M. D. Wittman, J. Phys. IV France **133**, 903 (2006).

31. W. Seka, V. N. Goncharov, J. A. Delettrez, D. H. Edgell, I. V. Igumenshchev, R. W. Short, A. V. Maximov, J. Myatt, and R. S. Craxton, Bull. Am. Phys. Soc. **51**, 340 (2006).

32. J. Delettrez, R. Epstein, M. C. Richardson, P. A. Jaanimagi, and B. L. Henke, Phys. Rev. A **36**, 3926 (1987).

33. R. C. Malone, R. L. McCrory, and R. L. Morse, Phys. Rev. Lett. **34**, 721 (1975).

34. V. N. Goncharov, T. C. Sangster, P. B. Radha, T. R. Boehly, T. J. B. Collins, R. S. Craxton, J. A. Delettrez, R. Epstein, V. Yu. Glebov, S. X. Hu, I. V. Igumenshchev, R. Janezic, S. J. Loucks, J. R. Marciante, J. A. Marozas, F. J. Marshall, D. N. Maywar, J. P. Knauer, P. W. McKenty, S. P. Regan, R. G. Roides, W. Seka, S. Skupsky, V. A. Smalyuk, J. M. Soures, C. Stoeckl, R. Betti, R. L. McCrory, D. D. Meyerhofer, D. Shvarts, J. A. Frenje, R. D. Petrasso, and C. K. Li, "Performance of Direct-Drive Cryogenic Targets on OMEGA," to be published Physics of Plasmas (invited).

35. V. N. Goncharov, O. V. Gotchev, E. Vianello, T. R. Boehly, J. P. Knauer, P. W. McKenty, P. B. Radha, S. P. Regan, T. C. Sangster, S. Skupsky, V. A. Smalyuk, R. Betti, R. L. McCrory, D. D. Meyerhofer, and C. Cherfils-Clérouin, Phys. Plasmas **13**, 012702 (2006).

36. T. Dewandre, J. R. Albritton, and E. A. Williams, Phys. Fluids **24**, 528 (1981).

37. W. L. Kruer, *The Physics of Laser–Plasma Interactions*, Frontiers in Physics, Vol. 73, edited by D. Pines (Addison-Wesley, Redwood City, CA, 1988), Chap. 4, pp. 37–43.

38. A. Simon, R. W. Short, E. A. Williams, and T. Dewandre, Phys. Fluids **26**, 3107 (1983).

39. A. L. Richard, J. P. Jadaud, N. Dague, M. C. Monteil, R. E. Turner, D. Bradley, R. J. Wallace, O. L. Landen, J. M. Soures, S. Morse, and G. Pien, in *ECLIM 2000: 26th European Conference on Laser Interaction with Matter*, edited by M. Kálal, K. Rohlena, and M. Šinor (SPIE, Bellingham, WA, 2001), Vol. 4424, pp. 23–26.

40. D. Edgell, W. Seka, J. A. Delettrez, R. S. Craxton, V. N. Goncharov, I. V. Igumenshchev, J. Myatt, A. V. Maximov, R. W. Short, T. C. Sangster, and R. E. Bahr, Bull. Am. Phys. Soc. **52**, 195 (2007).

41. R. K. Kirkwood, J. D. Moody, A. B. Langdon, B. I. Cohen, E. A. Williams, M. R. Dorr, J. A. Hittinger, R. Berger, P. E. Young, L. J. Suter, L. Divol, S. H. Glenzer, O. L. Landen, and W. Seka, Phys. Rev. Lett. **89**, 215003 (2002).

42. R. L. Berger and L. V. Powers, Phys. Fluids **28**, 2895 (1985).

43. W. L. Kruer, in *Laser Plasma Interactions*, edited by R. A. Cairns and J. J. Sanderson (Scottish Universites Summer School in Physics, Edinburgh, Scotland, 1980), pp. 387–432.

44. P. B. Radha, J. P. Knauer, T. C. Sangster, V. N. Goncharov, I. V. Igumenshchev, R. Betti, R. Epstein, D. D. Meyerhofer, and S. Skupsky, Bull. Am. Phys. Soc. **52**, 143 (2007); J. P. Knauer, P. B. Radha, V. N. Goncharov, I. V. Igumenshchev, R. Betti, R. Epstein, F. J. Marshall, S. P. Regan, V. A. Smalyuk, D. D. Meyerhofer, and S. Skupsky, Bull. Am. Phys. Soc. **52**, 233 (2007).

Monoenergetic Proton Radiography of Inertial Fusion Implosions

Identification and characterization of the physical phenomena associated with dynamic, extreme states of matter, such as those of high-energy-density physics[1,2] found in inertial fusion,[3,4] laboratory astrophysics,[2,5] and laser–plasma interaction physics,[6] are of fundamental scientific importance. A unique method of diagnosing inertial fusion implosions has resulted in the characterization of two distinct electromagnetic field configurations that have potentially consequential effects on implosion dynamics. This method also makes possible the quantitative study of the temporal evolution of capsule size and areal density.

The method involves radiography using a pulsed (0.1 ns), monoenergetic (15.0 MeV), quasi-isotropic proton source.[7] Fields are revealed in radiographs through deflection of proton trajectories, and areal densities are quantified through the energy lost by protons while traversing the plasma. The imaged samples are inertial confinement fusion (ICF) capsules of the fast-ignition (FI) variety,[8,9] initially 430 μm in radius, imploded by 36 laser beams that deposit 14 kJ of energy in a 1-ns pulse (see the appendix, p. 51).

For electricity generation[3,4] and for studies of high-energy-density physics in the laboratory,[1,2] ICF seeks to release copious energy by igniting a compressed pellet of fusion fuel. Fuel compression to densities of 300 g/cm^3 or higher will be achieved by energy deposition onto the surface of a fuel capsule over nanosecond time scales, either by laser light (direct drive) or by x rays generated in a cavity by laser light (indirect drive). Ignition and energy gain will occur in a central hot spot or, in the FI scheme, by the extremely rapid (~picoseconds) deposition of additional energy, either directly onto the compressed pellet,[8] or along the axis of a cone that keeps the path clear of plasma ablated from the pellet surface.[9]

The 15-MeV, monoenergetic proton radiography applied herein was recently used by Li *et al.* in a different context to investigate fields generated by laser–foil interactions.[10,11] MacKinnon *et al.*[12] used a broadband, non-isotropic proton source to study six-beam implosions, although they did not observe either striated or coherent field structures. In addition, earlier workers, using optical techniques largely sensitive to density perturbations, observed very fine-scale radial filaments and jets[13,14] in targets driven by one to four laser beams. However, the character of these structures is qualitatively different in several ways from the striations described in this article (see the appendix, p. 51).

In the experiments reported here (Fig. 113.47), cone-in-shell FI targets were radiographed before and during implosion, 1.56 ns after the start of the laser drive (Fig. 113.48), shortly after the end of the acceleration phase.[4] The radiographs were taken perpendicular to the Au cone axis. Figure 113.49 shows the experimental results (which are also characteristic of many implosions without cones). Because the detector records proton fluence and energy, Fig. 113.49 shows images that illustrate the spatial distributions of both proton fluence and mean proton energy.

Five important features are apparent in these images: First, the character of the isotropic and monoenergetic proton source

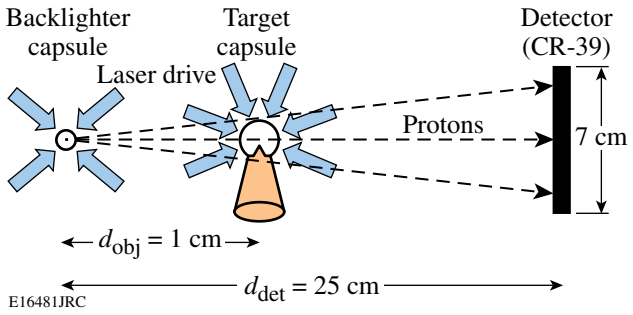

Figure 113.47
Schematic of experimental setup. A short (130 ps), monoenergetic ($\Delta E/E < 3\%$), quasi-isotropic pulse of 15.0-MeV D^3He fusion protons is generated by laser implosion of a backlighter capsule filled with D_2 and ^3He gas. The $\sim 3 \times 10^8$ protons emitted from the 45-μm FWHM source region interact with matter and electromagnetic fields in a cone-in-shell capsule implosion. The position and energy of every proton reaching the detector are individually recorded on CR-39, encoding the details of the matter and field distributions surrounding the target capsule.

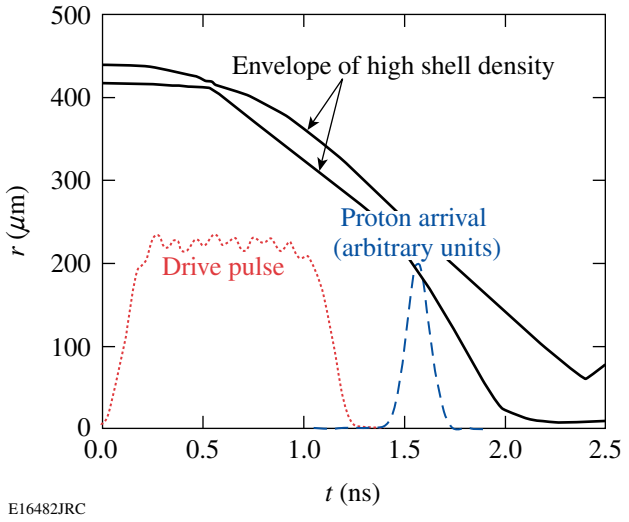

Figure 113.48
Cone-in-shell capsule drive pulse (dotted), simulated[16] shell trajectory (solid), and experimental backlighter proton arrival time (dashed). Simulations predict that the shell has compressed from its original radius by about a factor of 2, and the ρR has doubled to 5 mg/cm^2 when the backlighter protons arrive at 1.56 ns (OMEGA shot 46529).

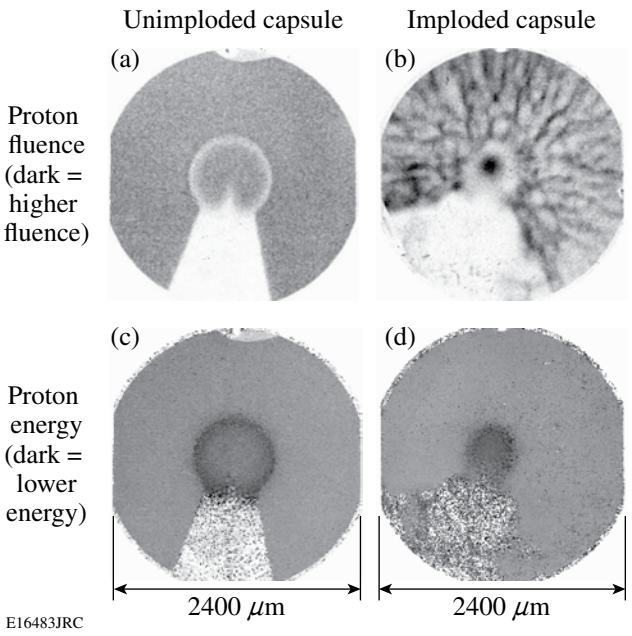

Figure 113.49
Images of a 430-μm-radius spherical CH capsule with attached gold cone, before and during implosion. Images (a) and (c) show the unimploded capsule used in OMEGA shot 46531. Images (b) and (d) show a capsule at 1.56 ns after the onset of the laser drive (shot 46529). In (a) and (b) dark areas correspond to regions of higher proton fluence, and in (c) and (d) dark areas correspond to regions of lower proton energy. The energy image values in the region shadowed by the cone are mostly noise since very few protons were detected in that region. See lineouts in Figs. 113.50 and 113.52 for image values.

is reflected in the uniform background of Figs. 113.49(a) and 113.49(c). Second, a complex filamentary structure is seen in the fluence image of Fig. 113.49(b). The uniform energy seen outside the capsule in Fig. 113.49(d) demonstrates that the fluence striations are caused by electromagnetic deflection rather than scattering through plasma density filaments. Third, substantial plasma blowoff from the cone casts a much wider shadow as the capsule is imploded. Fourth, a significant enhancement of the proton fluence at the center of the imploded target [Fig. 113.49(b)] suggests the presence of a radially directed, focusing electric field. Finally, radial compression of the capsule by a factor of 2 is seen in Fig. 113.49(d). The basic repeatability of the field structure and capsule compression was demonstrated using radiographs taken at the same relative time, but on different implosions.

In the images, field structure is studied by means of the spatial distribution of proton fluence. The proton-path–integrated electric (E) or magnetic (B) field can be estimated from the angular deflection θ of protons of energy E_p passing through the field region:

$$\int E_{\perp} d\ell = 2\left(E_p/e\right)\tan\theta, \tag{1}$$

$$\int B \times d\ell = \left(m_p v_p/e\right)\sin\theta, \tag{2}$$

$$\tan\theta = M\xi/\left(d_{det} - d_{obj}\right), \tag{3}$$

where m_p is the proton mass, v_p is the proton speed, e is the fundamental unit charge, the magnification $M = 25$, and d_{det} and d_{obj} are defined in Fig. 113.47. The deflection angle is determined by measuring the apparent displacement ξ of protons in the target plane using Eq. (3).

Areal density at different positions in the target capsule is studied through the downshift in proton energy relative to the incident energy of 15.0 MeV. It is proportional to the amount of matter traversed between the source and detector,[15] quantified by $\rho L\left(= \int \rho d\ell\right)$.

Radial lineouts of the images in Fig. 113.49 are shown in Fig. 113.50. In the fluence lineout [Fig. 113.50(b)] for the imploded target, the value near $r = 0$ μm is strikingly enhanced relative to the values at large radii (by a factor of 3) and at $r =$ 200 μm (by a factor of 6). To explain this, a radial electric field of about 1.5×10^9 V/m is necessary to "focus" 15.0-MeV protons passing near $r = 200$ μm toward the center to the extent observed. Scattering is insufficient to explain this result (see Fig. 113.51).

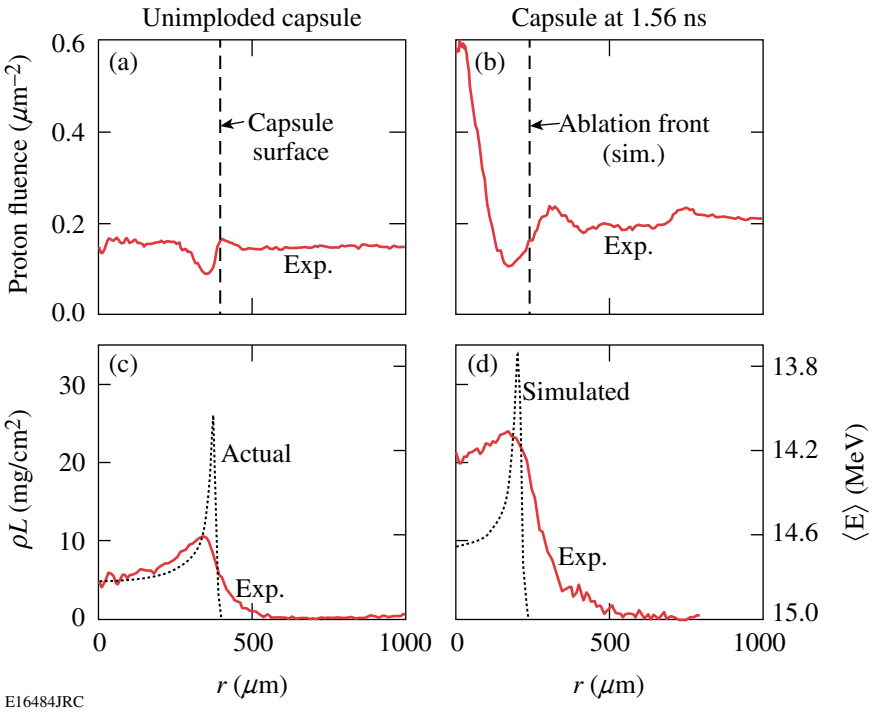

Figure 113.50
Radial lineouts of proton fluence and mean-path areal density (ρL) from Fig. 113.49. All lineouts are averaged over the azimuth, excluding the region of the cone shadow. (a) and (c): Unimploded capsule of shot 46531; (b) and (d): capsule of shot 46529, 1.56 ns after start of laser drive. The fluence lineout (a) shows the effects of angular scattering through the limb of the capsule shell. In (b), angular scattering effects alone are insufficient to explain the peak at $r = 0$. A radial electric field of ~10^9 V/m is necessary to "focus" the protons to the extent observed. In (c) and (d) radial lineouts of the mean energy images in Fig. 113.49 were converted to ρL. Also displayed are the (c) actual and (d) simulated ρL, assuming no angular scattering (dotted), where $\rho L/2 = \rho R$ at $r = 0$.

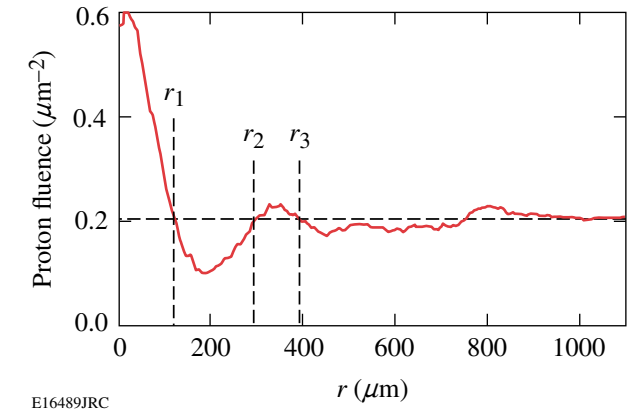

Figure 113.51
Reproduction of Fig. 113.50(b), marking the boundaries of the proton fluence enhancement at the center ($r < r_1$), the fluence depression through the capsule limb and E-field region ($r_1 < r < r_2$), and a secondary fluence enhancement outside the shell ($r_2 < r < r_3$). Fluence peaks and troughs in the far-field region ($r > 430$ μm = initial capsule radius) are the result of filamentary structures. Also marked is the proton fluence of 0.20 protons/μm^2, equal to the far-field average fluence. In the absence of a focusing electric field, one would expect that scattering of protons through the capsule limb should deflect an approximately equal number of protons inward as outward. The number of protons deflected out of the trough region $r_1 < r < r_2$ is about 12,300, calculated as the difference in the number of protons over an azimuthal integral in that region compared to the expected number based on the far-field fluence and the area of the region. The number of protons deflected into the inner and outer proton fluence peaks are 8200 and 4100, respectively. Therefore, angular scattering through the limb plasma can account for only about half of the protons in the central peak; we invoke the presence of a focusing E field to explain the remainder of the fluence enhancement at the center.

We conjecture that this coherent field is a consequence of a large, outward-directed electron pressure gradient that exists in the vicinity of the fuel–shell interface. Such a field might be expected to occur during, and shortly after, the acceleration phase of the implosion in which substantial shell mass is rapidly assembled and compressed. Such an electric field, given by $-\nabla P_e / en_e$, has been observed in the context of other recent laser–plasma experiments.[10] In this case, future measurements of the evolution of this coherent E field might effectively map capsule pressure dynamics throughout the implosion. Such information would be invaluable in assessing implosion performance.

Lineouts of the mean energy images of Figs. 113.49(c) and 113.49(d) can be used to infer the mean-path areal density ρL, shown in Figs. 113.50(c) and 113.50(d). The ρL lineout [Fig. 113.50(c)] of the unimploded target gives an initial radial areal density (ρR) of 2.5 mg/cm^2, which is very close to the actual initial ρR of 2.4 mg/cm^2. Scattering of protons smears out measured ρL values near the limb of the shell at $r = 410$ μm. Both measurement and simulation[16] indicate a factor-of-2 reduction in capsule radius at 1.56 ns. However, the ρL lineout [Fig. 113.50(d)] of the imploded capsule at 1.56 ns implies that the capsule ρR has increased to 10 mg/cm^2, which is twice the 5 mg/cm^2 predicted by numerical simulation. This high apparent experimental ρR is due in part to scattering and in part to E-field focusing of the lower-energy protons passing through the limb of the capsule shell.

Returning to the filamentary fields, we note how the outer edge of the coherent field merges, at a boundary just outside the imploding capsule, into the striated fields. As illustrated in Fig. 113.52(c) and in Fig. 113.55 of the appendix, the striated fields originate inside the critical surface, which is extremely close to the capsule surface. Azimuthal lineouts of the proton fluence image of Fig. 113.49(b) at radii 430 μm and 860 μm show the amplitude and scale of proton fluence variations (Fig. 113.52) due to striations. Peak-to-valley fluence modulations of a factor of 4 are seen at both radii. The typical angular oscillation period is 20° and 10° for the inner and outer radii, respectively, corresponding to the same 150-μm spatial distance between striations. This distance implies a deflection angle of 0.45°, which gives a path-integrated magnetic field $\int \mathrm{B} \times \mathrm{d}\ell$ of 4000 T μm. Assuming an integration path length equal to the typical width of striations (75 μm) results in a magnetic field strength of ~60 T. If the fluence variations are instead due to E fields, the field strength required is ~3×10^9 V/m, although quasi-neutrality of the coronal plasma with no laser energy source makes this interpretation unlikely.

The occurrence of such strong inhomogeneities inside the critical surface ~0.5 ns after the laser drive ends suggests that substantially larger fields are likely present just before laser shutoff.[17,18] This situation would be reflected in a Hall parameter ($\omega\tau$) of the order of 1 or larger, the inverse square of which reduces the classical electron heat transport.[17,18] This situation would result in the inhomogeneous inhibition of thermal transport over the capsule surface, altering even the zeroth-order hydrodynamics.[18,19] Whether the source of these inhomogeneities is Rayleigh–Taylor (RT),[20] electrothermal,[19] collisional Weibel,[13,17] or another instability, they will provide seeds for RT growth that, if too substantial, could degrade capsule compression and quench ignition during the final stagnation phase.[4,17,18] These issues are being actively investigated.

It seems plausible that either the electrothermal or RT instability could be the relevant source. Ongoing planar experiments, in which RT was purposely seeded, measured B fields of the order of 100 T using the method described here (see the appendix, p. 51). Furthermore, estimates (based on Ref. 18) of the RT-generated B field under similar conditions give fields of the same magnitude (see the appendix, p. 51). Radiography of driven solid-CH balls, which undergo no acceleration to drive RT growth, could be used to determine if RT is a contributing mechanism.

Finally, the vast spatial extent of these striated fields likely reflects their outward convection resulting from the plasma flow because the fields are tied to the out-flowing plasma due to high plasma electrical conductivity. We conjecture that these radiographic images thus provide snapshots of structures originally produced inside the critical surface at various times during the implosion.

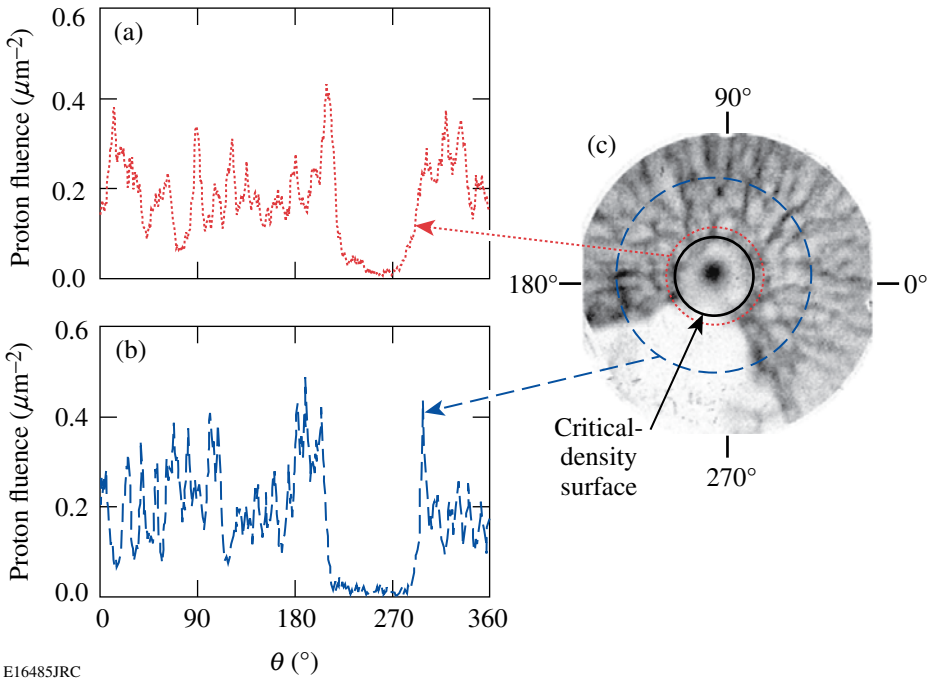

Figure 113.52
Circular lineouts of proton fluence obtained from shot 46529 at radii of (a) 430 μm and (b) 860 μm. The filamentary structures represent a 2-D projection of a 3-D field structure that originates inside the critical density surface (c).

In summary, two distinctly different, simultaneously occurring electromagnetic field structures, with important implications for implosion dynamics, have been characterized in imploding ICF capsules. First, a complex filamentary field topology permeates the entire 2400-μm field of view with striations corresponding to 60-T magnetic fields. This field, through the inhomogeneous inhibition of heat flux in the vicinity of the ablation surface, could generate seeds for RT growth, thereby affecting the overall implosion dynamics.[4,6,18,19] Second, a coherent, radial electric field of magnitude 10^9 V/m exists in the immediate vicinity of the capsule, dramatically focusing protons toward the center.[21] This hitherto unobserved field is conjectured to originate from the gradient of electron pressure. If verified, a window for analyzing the evolution of the internal pressure dynamics is opened; this would be of immense value for critically assessing the entire implosion process.

Appendix: Monoenergetic Proton Radiography of Inertial Fusion Implosions

1. Materials and Methods

All experiments were performed at the OMEGA Laser Facility,[22] which delivers up to 30 kJ in 60 beams at a wavelength of 351 nm. Full beam smoothing[23] was used on each beam to reduce high-mode nonuniformities caused by laser speckle.

A schematic illustration of the proton radiography setup is shown in Fig. 113.47. The source of monoenergetic protons is a 220-μm-radius, 2.2-μm-thick spherical glass (SiO_2) shell filled with deuterium (D_2) and helium-3 (^{3}He) gas.[7] This backlighter capsule is illuminated by 17 laser beams, delivering 6.9 kJ of energy in a 1-ns pulse, which compresses and heats the gas such that the D-^{3}He fusion reaction, D + ^{3}He $\longrightarrow$ ^{4}He + p, proceeds. The protons are quasi-isotropically emitted in a 130-ps pulse[24] at an energy of 15.0 MeV[25] with a spectral width[26] $\Delta E/E < 3\%$ and from a region 45 μm across[7] (see Fig. 113.53). Typical proton yields are 1 to 4 $\times$ 10^8, and the yields for the OMEGA shots shown in the manuscript were 2.9 $\times$ 10^8 (shot 46531) and 3.7 $\times$ 10^8 (shot 46529). The backlighter implosion has not yet been fully optimized for proton yield, pulse duration, or source size.

The target imaged is a 430-μm-radius, 23-μm-thick spherical plastic (CH) shell with an embedded gold (Au) cone of 5-mm height, 30-μm thickness, and an opening angle of 35°. The cone ends in a shelf (see Fig. 113.54) where the cone intersects the shell, and a smaller cone tip reaches inward to a distance of 40 μm from the capsule center. Forty beams in a spherically symmetric configuration are pointed at the spherical shell; the shell is then directly driven with 14.1 kJ using 36 of those beams (the four beams aimed nearest the cone axis remain off to avoid the laser hitting the inside of the cone), for an on-target illumination intensity of 6.7 $\times$ 10^{14} W/cm^2. Because the OMEGA system is optimized for a 60-beam spherical drive, the illumination uniformity is degraded in this configuration from <2% to ~7% rms.

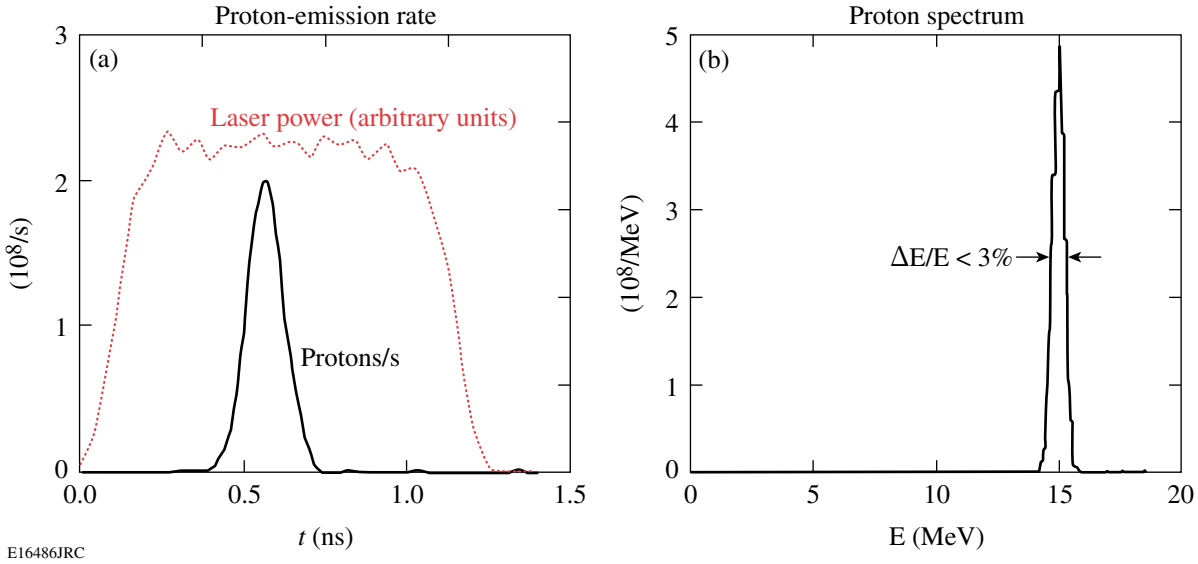

Figure 113.53
Measured characteristics of proton emission from the source implosion. (a) Emission history and (b) spectrum of emitted D^{3}He protons from the backlighter capsule on OMEGA shot 46531. The total D^{3}He proton yield was 2.9 $\times$ 10^8.

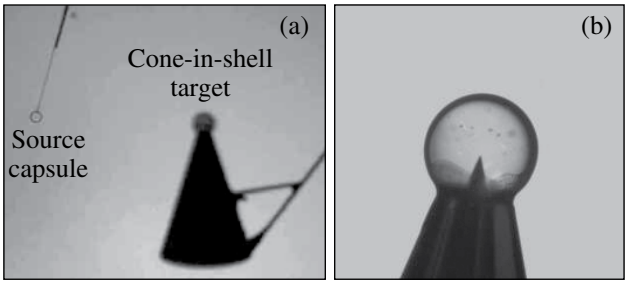

Figure 113.54
(a) Pre-implosion snapshot of source and target capsules. (b) A close-up photograph of the cone-in-shell target sphere. (See also Fig. 113.47.)

The imaging detector is CR-39, a plastic nuclear track detector with submicron spatial resolution, low sensitivity to electromagnetic and x-ray noise sources, and energy-resolving characteristics.[26] The position and energy of every incident proton are recorded. The center of the sphere in the subject target is placed 1.0 cm from the center of the backlighter capsule, and the detector is located 25 cm from the source, so structure in the subject is magnified by a factor $M = 25$ at the detector. The relative timing of the backlighter and subject-capsule laser drive beams is adjusted so the backlighter protons arrive at the subject capsule at a desired time interval following the onset of target-capsule drive (Fig. 113.54).

The spatial resolution of the system, neglecting scattering in the target, is limited primarily by the finite source size and results in convolution of structure in the target plane by a Gaussian of about 43-μm FWHM. Smaller structures cannot be observed in the capsule corona without further optimization of the backlighter source.

The energy resolution of the system is about 0.05 MeV, corresponding to an areal-density resolution of about 1.5 mg/cm^2. A more thorough analysis of the absolute accuracy of proton energy measurements on the radiographic CR-39, as well as an assessment of the effects of angular scattering of protons through plasma in the target plane, is currently in progress.

2. Other Relevant Work

Of direct relevance to this article, and in support of the presence of the observed field structures, Shiraga *et al.*[27] and Séguin *et al.*[28] inferred the presence of residual electromagnetic fields outside imploded capsules (exploding pushers and ablatively driven implosions similar to those studied here, respectively) on the basis of fluence variations in self-emitted, charged fusion products. Furthermore, characterization of capsule assembly and symmetry in ICF-relevant implosions has included extensive use of self-emitted fusion protons,[26,29] including those from implosions of fast-ignition (FI) targets.[30] Recently, Li *et al.*[7] suggested that a complementary way to study implosions and, in particular, the spatial structure of fields and areal density, is through monoenergetic proton radiography.

Filamentary and jet-like structures were previously observed near the critical surface using shadowgraphic, interferometric, and Faraday rotation techniques by several groups during laser illumination of both planar[31,32] and spherical targets.[13,14] As mentioned in the main text, there are substantial differences between the filamentary structures observed by these groups and those reported in this article: (1) The lateral spatial wavelength of structures was 10 μm, and examination of their data shows no evidence of the ~150-μm spatial scale that we see. (2) The radial extent of the earlier structures is much smaller and confined, whereas the structures reported here fill the entire field of view. (3) Fine structures originate well into the underdense plasma, while the structures here originate inside the critical surface, even approaching the ablation surface (see Fig. 113.55). (4) For uniformly illuminated implosions, fields greater than 10 T were not detected.[33] In addition, it is useful to point out that one of the unique advantages of the particle probe that we have used is that it is not "cut off" by critical-density plasma effects as is the case for optical probes.

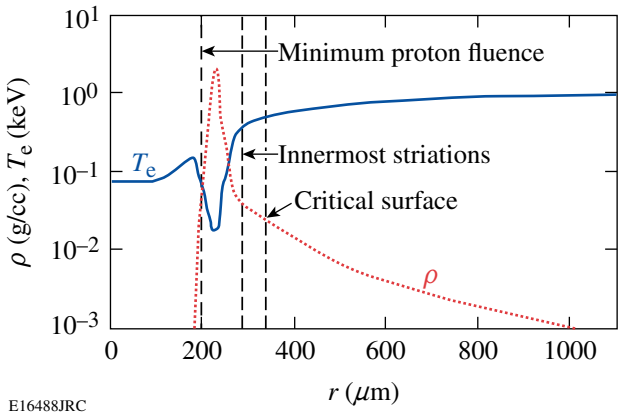

Figure 113.55
LILAC[36] simulation of the mass density and electron temperature profiles of the imploding capsule at 1.56 ns, ~0.3 ns after the laser has turned off. At this time, the capsule shell (the region of highest density near 230 μm) is imploding inward at approximately constant speed. The radius corresponding to the observed minimum proton fluence (Fig. 113.51) occurs at the inner shell surface in the simulation. The innermost striations are observed at about 300 μm [Fig. 113.49(b)], well inside the critical-density surface (for $\lambda = 0.351$ μm).

Previous studies of laser–capsule interactions using broadband proton radiography[34] include Borghesi *et al.*[35] and MacKinnon *et al.*[12] Borghesi illuminated a sphere from one side using a short (1 ps), intense pulse and observed filamentary structures similar to those described in the previous paragraph. MacKinnon, however, saw no filamentary or focusing fields surrounding a capsule driven with six 1-ns laser beams. The fact that MacKinnon did not see these structures is not presently understood. There are, however, substantial differences in the implosion conditions compared to the current work. For example, MacKinnon used six beams at 1-μm wavelength and 1.5×10^{13}-W/cm^2 intensity; herein we used 36 beams at 1/3 μm and 6.7×10^{14} W/cm^2. In addition, MacKinnon's radiographic images were obtained substantially after (~1.5 ns) the end of the driving laser pulse, whereas in the current work, radiographs were obtained shortly after (~0.3 ns) the end of the pulse. If the observed field structures are produced and sustained by the laser (see Possible Mechanisms below), the structures may no longer be detectable 1 ns after their generating source has turned off.

The monoenergetic D^{3}He fusion proton emission from backlighter capsules has, for the purposes of these experiments, distinct advantages over broadband, non-isotropic proton emissions associated with intense-laser-beam experiments.[34] A single energy provides unambiguous quantitative relationships between proton energy loss through the target and areal density and also between proton trajectory bending and field strengths at the target. Quasi-isotropy allows for imaging of large objects, or even simultaneous imaging of multiple objects in totally different directions (as has been done in other contexts[11]).

3. Possible Mechanisms

Numerous instabilities that generate magnetic fields in laser–plasma experiments have been identified or proposed,[17] and take place over a wide range of plasma conditions. Instabilities generated outside the critical surface are the collisionless Weibel, thermomagnetic, and filamentation instabilities. Just inside the critical surface, the collisional Weibel, $\nabla T \times \nabla n$, and thermomagnetic instabilities will grow. Nernst convection can carry B fields generated by these instabilities inward.[17] The electrothermal instability occurs when the mean free path is shorter than the electron skin depth.[19] The Rayleigh–Taylor (RT) instability generates B fields at the ablation front.[18,20]

Monoenergetic proton radiography of planar foils seeded with RT ripples is currently in progress to investigate the generation and growth of fields by RT processes. Preliminary results have observed ~100-T-magnitude magnetic field structures, which are absent when the rippled RT seed is absent from the foil.

An estimate of the RT-induced B-field magnitude can be obtained using the work of Nishiguchi.[18] The capsule shell's acceleration g can be approximated from the experimental observations as the distance the shell has traveled over one half the square of the time it took to get there, $g = 2 \times (430–215\ \mu\text{m})/(1.5\ \text{ns})^2 \approx 200\ \mu\text{m/ns}^2$. The observed transverse spacing between filaments near the capsule surface is typically 150 μm. From *LILAC* simulations,[36] $L = 10\ \mu$m is typical of the plasma density scale length. From these values, $kL = 0.42$. Consulting Fig. 1 of Nishiguchi, this gives a peak B-field magnitude of about 300 T at the end of the linear phase of RT growth—only 5× the observed B-field magnitude "averaged" over the width of a filament.

Although RT processes could plausibly generate the observed B fields, other mechanisms cannot yet be ruled out. New experiments using monoenergetic proton radiography will be performed to investigate which instability mechanism(s) is (are) at work. A time sequence of radiographs would enable observation of the onset, growth, and decay of such filamentary structures. Variation of the intensity and other laser conditions could be used to elucidate the origin and any thresholds. Comparison of these radiography results with those from driven solid-CH balls, which undergo no acceleration to drive RT growth, would determine if RT is a dominant mechanism.

Whatever the mechanism, magnetic fields generated close to the ablation front would get "frozen in" to the ablating material and would follow the plasma flow off the capsule surface. Therefore, structures at the edge of the field of view were actually generated some several hundred picoseconds earlier, making it possible to record a history of the filamentary structure in a single radiographic snapshot.

In regard to the coherent focusing field, this article has emphasized the possible and likely connection between the central coherent electric field and the pressure gradient at the fuel–shell interface. Yet, another intriguing consequence is that this field could also opportunely reflect hot electrons that otherwise might preheat the fuel. To make such an assessment quantitative would require that we have information about both the evolution of this coherent field and how it is affected by the laser pulse shape and the capsule itself. (Because of shot limitations, for example, we have so far investigated only the coherent field for the 1-ns square pulse shape, as depicted in Fig. 113.48.) We would also need rather detailed information

about the bath of hot electrons, how it is generated, how it depends on pulse shape and the capsule, and, in general, how the hot-electron distribution evolves. In the course of exploring the full consequences of the central coherent field, we will investigate this preheat amelioration possibility.

ACKNOWLEDGMENT

We express our gratitude to the OMEGA engineers and operations crew who supported these experiments, and to General Atomics for providing high-quality backlighter and target capsules. This work was supported by the Fusion Science Center (FSC) for Extreme States of Matter and Fast Ignition at the University of Rochester and by the U. S. Department of Energy Office of Inertial Confinement (Grant No. DE-FG03-03NA00058). J. R. R. also acknowledges the FSC for his post-doctoral financial support.

REFERENCES

1. National Research Council (U.S.) Committee on High Energy Density Plasma Physics, *Frontiers in High Energy Density Physics: The X-Games of Contemporary Science* (National Academies Press, Washington, DC, 2003).

2. R. P. Drake, *High-Energy-Density Physics: Fundamentals, Inertial Fusion, and Experimental Astrophysics, Shock Wave and High Pressure Phenomena* (Springer, Berlin, 2006).

3. J. Nuckolls *et al.*, Nature **239**, 139 (1972).

4. S. Atzeni and J. Meyer-ter-Vehn, *The Physics of Inertial Fusion: Beam Plasma Interaction, Hydrodynamics, Hot Dense Matter*, International Series of Monographs on Physics (Clarendon Press, Oxford, 2004).

5. B. A. Remington, R. P. Drake, and D. D. Ryutov, Rev. Mod. Phys. **78**, 755 (2006).

6. W. L. Kruer, *The Physics of Laser Plasma Interactions, Frontiers in Physics* (Westview Press, Boulder, CO, 2003), pp. 39–43.

7. C. K. Li, F. H. Séguin, J. A. Frenje, J. R. Rygg, R. D. Petrasso, R. P. J. Town, P. A. Amendt, S. P. Hatchett, O. L. Landen, A. J. Mackinnon, P. K. Patel, V. Smalyuk, J. P. Knauer, T. C. Sangster, and C. Stoeckl, Rev. Sci. Instrum. **77**, 10E725 (2006).

8. M. Tabak *et al.*, Phys. Plasmas **1**, 1626 (1994).

9. R. Kodama *et al.*, Nature **418**, 933 (2002).

10. C. K. Li, F. H. Séguin, J. A. Frenje, J. R. Rygg, R. D. Petrasso, R. P. J. Town, P. A. Amendt, S. P. Hatchett, O. L. Landen, A. J. Mackinnon, P. K. Patel, V. A. Smalyuk, T. C. Sangster, and J. P. Knauer, Phys. Rev. Lett. **97**, 135003 (2006).

11. C. K. Li, F. H. Séguin, J. A. Frenje, J. R. Rygg, R. D. Petrasso, R. P. J. Town, O. L. Landen, J. P. Knauer, and V. A. Smalyuk, Phys. Rev. Lett. **99**, 055001 (2007).

12. A. J. Mackinnon *et al.*, Phys. Rev. Lett. **97**, 045001 (2006).

13. T. Mochizuki *et al.*, Jpn. J. Appl. Phys. **19**, L645 (1980).

14. O. Willi and P. T. Rumsby, Opt. Commun. **37**, 45 (1981).

15. C. K. Li and R. D. Petrasso, Phys. Rev. Lett. **70**, 3059 (1993).

16. Numerical simulations of full-sphere capsules, equivalent to the target capsule with no cone, were performed with the 1-D hydrodynamic code *LILAC*.[36] The use of 1-D spherical geometry to simulate the areal density of cone-in-shell capsules was previously used and found reasonable.[30]

17. M. G. Haines, Can. J. Phys. **64**, 912 (1986).

18. A. Nishiguchi, Jpn. J. Appl. Phys. **41**, 326 (2002).

19. M. G. Haines, Phys. Rev. Lett. **47**, 917 (1981).

20. K. Mima, T. Tajima, and J. N. Leboeuf, Phys. Rev. Lett. **41**, 1715 (1978).

21. The filamentary and focusing fields are present irrespective of whether the capsule is of the hot-spot or fast-ignition variety.

22. T. R. Boehly, D. L. Brown, R. S. Craxton, R. L. Keck, J. P. Knauer, J. H. Kelly, T. J. Kessler, S. A. Kumpan, S. J. Loucks, S. A. Letzring, F. J. Marshall, R. L. McCrory, S. F. B. Morse, W. Seka, J. M. Soures, and C. P. Verdon, Opt. Commun. **133**, 495 (1997).

23. S. Skupsky and R. S. Craxton, Phys. Plasmas **6**, 2157 (1999).

24. J. A. Frenje, C. K. Li, F. H. Séguin, J. Deciantis, S. Kurebayashi, J. R. Rygg, R. D. Petrasso, J. Delettrez, V. Yu. Glebov, C. Stoeckl, F. J. Marshall, D. D. Meyerhofer, T. C. Sangster, V. A. Smalyuk, and J. M. Soures, Phys. Plasmas **11**, 2798 (2003).

25. Hot electrons escaping from the backlighter capsule during laser irradiation results in a capsule charge of several hundred kV, which accelerates the escaping D^3He protons above their 14.7-MeV birth energy. This shift is measured to 0.1-MeV accuracy by the proton spectrometers.[26]

26. F. H. Séguin, J. A. Frenje, C. K. Li, D. G. Hicks, S. Kurebayashi, J. R. Rygg, B.-E. Schwartz, R. D. Petrasso, S. Roberts, J. M. Soures, D. D. Meyerhofer, T. C. Sangster, J. P. Knauer, C. Sorce, V. Yu. Glebov, C. Stoeckl, T. W. Phillips, R. J. Leeper, K. Fletcher, and S. Padalino, Rev. Sci. Instrum. **74**, 975 (2003).

27. H. Shiraga, T. Mochizuki, and C. Yamanaka, Appl. Phys. Lett. **37**, 602 (1980).

28. F. H. Séguin, C. K. Li, J. A. Frenje, S. Kurebayashi, R. D. Petrasso, F. J. Marshall, D. D. Meyerhofer, J. M. Soures, T. C. Sangster, C. Stoeckl, J. A. Delettrez, P. B. Radha, V. A. Smalyuk, and S. Roberts, Phys. Plasmas **9**, 3558 (2002).

29. H. Azechi *et al.*, Laser Part. Beams **9**, 193 (1991).

30. C. Stoeckl, T. R. Boehly, J. A. Delettrez, S. P. Hatchett, J. A. Frenje, V. Yu. Glebov, C. K. Li, J. E. Miller, R. D. Petrasso, F. H. Séguin, V. A. Smalyuk, R. B. Stephens, W. Theobald, B. Yaakobi, and T. C. Sangster, Plasma Phys. Control. Fusion **47**, B856 (2005).

31. B. Grek *et al.*, Phys. Rev. Lett. **41**, 1811 (1978).

32. G. Thiell and B. Meyer, Laser Part. Beams **3**, 51 (1985).

33. O. Willi, P. T. Rumsby, and C. Duncan, Opt. Commun. **37**, 40 (1981).

34. A. J. Mackinnon, P. K. Patel, R. P. Town, M. J. Edwards, T. Phillips, S. C. Lerner, D. W. Price, D. Hicks, M. H. Key, S. Hatchett, S. C. Wilks, M. Borghesi, L. Romagnani, S. Kar, T. Toncian, G. Pretzler, O. Willi, M. Koenig, E. Martinolli, S. Lepape, A. Benuzzi-Mounaix, P. Audebert, J. C. Gauthier, J. King, R. Snavely, R. R. Freeman, and T. Boehly, Rev. Sci. Instrum. **75**, 3531 (2004).

35. M. Borghesi *et al.*, Phys. Plasmas **9**, 2214 (2002).

36. J. Delettrez, R. Epstein, M. C. Richardson, P. A. Jaanimagi, and B. L. Henke, Phys. Rev. A **36**, 3926 (1987).

Publications and Conference Presentations

Publications

B. Ashe, C. Giacofei, G. Myhre, and A. W. Schmid, "Optimizing a Cleaning Process for Multilayer-Dielectric- (MLD) Diffraction Grating," in *Laser-Induced Damage in Optical Materials: 2007*, edited by G. J. Exarhos, A. H. Guenther, K. L. Lewis, D. Ristau, M. J. Soileau, and C. J. Stolz (SPIE, Bellingham, WA, 2007), Vol. 6720, p. 67200N.

T. R. Boehly, J. E. Miller, D. D. Meyerhofer, J. H. Eggert, P. M. Celliers, D. G. Hicks, and G. W. Collins, "Measurements of the Release of Alpha Quartz: A New Standard for Impedance-Matching Experiments," in *Shock Compression of Condensed Matter–2007*, edited by M. Elert, M. D. Furnish, R. Chau, N. Holmes, and J. Nguyen (American Institute of Physics, Melville, NY, 2007), Vol. 955, pp. 19–22.

A. S. Cross, D. Wang, G. Guarino, S. Wu, A. Mycielski, and R. Sobolewski, "Studies of Coherent Acoustic Phonons in CdMnTe Diluted-Magnetic Single Crystals," J. Phys., Conf. Ser. **92**, 012015 (2007).

J. E. DeGroote, A. E. Marino, J. P. Wilson, A. L. Bishop, and S. D. Jacobs, "The Role of Nanodiamonds in the Polishing Zone During Magnetorheological Finishing (MRF)," in *Optical Manufacturing and Testing VII*, edited by J. H. Burge, O. W. Faehnle, and R. Williamson (SPIE, Bellingham, WA, 2007), Vol. 6671, p. 66710Z.

J. E. DeGroote, A. E. Marino, J. P. Wilson, A. L. Bishop, J. C. Lambropoulos, and S. D. Jacobs, "Removal Rate Model for Magnetorheological Finishing of Glass," Appl. Opt. **46**, 7927 (2007).

C. Dorrer, "Analysis of Pump-Induced Temporal Contrast Degradation in Optical Parametric Chirped-Pulse Amplification," J. Opt. Soc. Am. B **24**, 3048 (2007).

W. Guan, Z. Jiang, and J. R. Marciante, "Specialty Fibers Shine as High-Power, High-Beam-Quality, Fiber Sources," Laser Focus World **43**, 105 (2007).

W. Guan and J. R. Marciante, "Pump-Induced, Dual-Frequency Switching in a Short-Cavity, Ytterbium-Doped Fiber Laser," Opt. Express **15**, 14,979 (2007).

C. Kim, J. U. Wallace, A. Trajkovska, J. J. Ou, and S. H. Chen, "Quantitative Assessment of Coumarin-Containing Polymer Film's Capability for Photoalignment of Liquid Crystals," Macromolecules **40**, 8924 (2007).

K. L. Marshall, Z. Culakova, B. Ashe, C. Giacofei, A. L. Rigatti, T. J. Kessler, A. W. Schmid, J. B. Oliver, and A. Kozlov, "Vapor-Phase–Deposited Organosilane Coatings as 'Hardening' Agents for High-Peak-Power Laser Optics," in *Thin-Film Coatings for Optical Applications IV*, edited by M. J. Ellison (SPIE, Bellingham, WA, 2007), Vol. 6674, p. 667407.

K. L. Marshall, R. Wang, M. Coan, A. G. Noto, K. Leskow, R. Pauszek, and A. Moore, "Using Time-Dependent Density Functional Theory (TDDFT) in the Design and Development of Near-IR Dopants for Liquid Crystal Device Applications," in *Liquid Crystals XI*, edited by I. C. Khoo (SPIE, Bellingham, WA, 2007), Vol. 6654, p. 66540F.

D. N. Maywar, K. P. Solomon, and G. P. Agrawal, "Remote Optical Control of an Optical Flip-Flop," Opt. Lett. **32**, 3260 (2007).

R. L. McCrory, D. D. Meyerhofer, S. J. Loucks, S. Skupsky, R. Betti, T. R. Boehly, T. J. B. Collins, R. S. Craxton, J. A. Delettrez, D. H. Edgell, R. Epstein, K. A. Fletcher, C. Freeman, J. A. Frenje, V. Yu. Glebov, V. N. Goncharov, D. R. Harding, I. V. Igumenshchev, R. L. Keck, J. D. Kilkenny, J. P. Knauer, C. K. Li, J. Marciante, J. A. Marozas, F. J. Marshall, A. V. Maximov, P. W. McKenty, S. F. B. Morse, J. Myatt, S. Padalino, R. D. Petrasso, P. B. Radha, S. P. Regan, T. C. Sangster, F. H. Séguin, W. Seka, V. A. Smalyuk, J. M. Soures, C. Stoeckl, B. Yaakobi, and J. D. Zuegel, "Progress in Direct-Drive Inertial Confinement Fusion Research at the Laboratory for Laser Energetics," Eur. Phys. J. D **44**, 233 (2007).

C. Miao, K. M. Bristol, A. E. Marino, S. N. Shafrir, J. E. DeGroote, and S. D. Jacobs, "Magnetorheological Fluid Template for Basic Studies of Mechanical-Chemical Effects During Polishing," in *Optical Manufacturing and Testing VII*, edited by J. H. Burge, O. W. Faehnle, and R. Williamson (SPIE, Bellingham, WA, 2007), Vol. 6671, p. 667110.

J. E. Miller, T. R. Boehly, D. D. Meyerhofer, and J. H. Eggert, "Equation-of-State Measurements in Ta_2O_5 Aerogel," in *Shock Compression of Condensed Matter–2007*, edited by M. Elert, M. D. Furnish, R. Chau, N. Holmes, and J. Nguyen (American Institute of Physics, Melville, NY, 2007), Vol. 955, pp. 71–74.

A. V. Okishev, C. Dorrer, V. I. Smirnov, L. B. Glebov, and J. D. Zuegel, "ASE Suppression in a Diode-Pumped Nd:YLF Regenerative Amplifier Using a Volume Bragg Grating," in *Frontiers in Optics 2007/Laser Science XXIII/Organic Materials and Devices for Displays and Energy Conversion* (Optical Society of America, Washington, DC, 2007), Paper LTuB4.

S. Papernov, A. W. Schmid, J. B. Oliver, and A. L. Rigatti, "Damage Thresholds and Morphology of the Front- and Back-Irradiated SiO_2 Thin Films Containing Gold Nanoparticles as Artificial Absorbing Defects," in *Laser-Induced Damage in Optical Materials: 2007*, edited by G. J. Exarhos, A. H. Guenther, K. L. Lewis, D. Ristau, M. J. Soileau, and C. J. Stolz (SPIE, Bellingham, WA, 2007), Vol. 6720, p. 67200G.

T. C. Sangster, R. L. McCrory, V. N. Goncharov, D. R. Harding, S. J. Loucks, P. W. McKenty, D. D. Meyerhofer, S. Skupsky, B. Yaakobi, B. J. MacGowan, L. J. Atherton, B. A. Hammel, J. D. Lindl, E. I. Moses, J. L. Porter, M. E. Cuneo, M. K. Matzen, C. W. Barnes, J. C. Fernandez, D. C. Wilson, J. D. Kilkenny, T. P. Bernat, A. Nikroo, B. G. Logan, S. Yu, R. D. Petrasso, J. D. Sethian, and S. Obenschain, "Overview of Inertial Fusion Research in the United States," Nucl. Fusion **47**, S686 (2007).

H. Sawada, S. P. Regan, D. D. Meyerhofer, I. V. Igumenshchev, V. N. Goncharov, T. R. Boehly, R. Epstein, T. C. Sangster, V. A. Smalyuk, B. Yaakobi, G. Gregori, S. H. Glenzer, and O. L. Landen, "Diagnosing Direct-Drive, Shock-Heated, and Compressed Plastic Planar Foils with Noncollective Spectrally Resolved X-Ray Scattering," Phys. Plasmas **14**, 122703 (2007).

S. N. Shafrir, J. C. Lambropoulos, and S. D. Jacobs, "MRF Spotting Technique for Studying Subsurface Damage in Deterministic Microground Polycrystalline Alumina," in *Optical Manufacturing and Testing VII*, edited by J. H. Burge, O. W. Faehnle, and R. Williamson (SPIE, Bellingham, WA, 2007), Vol. 6671, p. 66710J.

S. N. Shafrir, J. C. Lambropoulos, and S. D. Jacobs, "Toward Magnetorheological Finishing of Magnetic Materials," J. Manuf. Sci. Eng. **129**, 961 (2007).

C. Stoeckl, T. R. Boehly, J. A. Delettrez, S. P. Hatchett, J. A. Frenje, V. Yu. Glebov, C. K. Li, J. E. Miller, R. D. Petrasso, F. H. Séguin, V. A. Smalyuk, R. B. Stephens, W. Theobald, B. Yaakobi, and T. C. Sangster, "Hydrodynamics Studies of Direct-Drive Cone-in-Shell, Fast-Ignitor Targets on OMEGA," Phys. Plasmas **14**, 112702 (2007).

A. Trajkovska, C. Kim, J. U. Wallace, and S. H. Chen, "Photoalignment of Monodisperse Glassy-Nematic Oligofluorenes," in *Liquid Crystals XI*, edited by I. C. Khoo (SPIE, Bellingham, WA, 2007), Vol. 6654, p. 665409.

J. U. Wallace, R. H. Young, C. W. Tang, and S. H. Chen, "Charge-Retraction Time-of-Flight Measurement for Organic Charge Transport Materials," Appl. Phys. Lett. **91**, 152104 (2007).

L. Welser-Sherrill, R. C. Mancini, J. A. Koch, N. Izumi, R. Tommasini, S. W. Haan, D. A. Haynes, I. E. Golovkin, J. J. MacFarlane, J. A. Delettrez, F. J. Marshall, S. P. Regan, V. A. Smalyuk, and G. Kyrala, "Spectroscopic Determination of Temperature and Density Spatial Profiles and Mix in Indirect-Drive Implosion Cores," Phys. Rev. E **76**, 056403 (2007).

S. Wu, J. Zhang, A. Belousov, J. Karpinski, and R. Sobolewski, "Ultra-Long-Lived Coherent Acoustic Phonons in GaN Single Crystals," J. Phys., Conf. Ser. **92**, 012021 (2007).

Forthcoming Publications

A. M. Cok, R. S. Craxton, and P. W. McKenty, "Polar-Drive Designs for Optimizing Neutron Yields on the National Ignition Facility," to be published in Physics of Plasmas.

C. Dorrer and J. Bromage, "Impact of High-Frequency, Spectral Phase Modulation on the Temporal Profile of Short Optical Pulses," to be published in Optics Express.

C. Dorrer and I. Kang, "Linear Self-Referencing Techniques for Short Optical Pulse Characterization," to be published in the Journal of the Optical Society of America B (invited).

M. C. Ghilea, T. C. Sangster, D. D. Meyerhofer, R. A. Lerche, and L. Disdier, "Aperture Tolerances for Neutron Imaging Systems in Inertial Confinement Fusion," to be published in Review of Scientific Instruments.

V. N. Goncharov, "Ablative Richtmyer–Meshkov Instability: Theory and Experimental Results," to be published in the Proceedings of Scottish Summer School.

V. N. Goncharov, "Direct-Drive Inertial Fusion: Basic Concepts and Ignition Target Designing," to be published in the Proceedings of Scottish Summer School.

V. N. Goncharov, T. C. Sangster, P. B. Radha, T. R. Boehly, T. J. B. Collins, R. S. Craxton, J. A. Delettrez, R. Epstein, V. Yu. Glebov, S. X. Hu, I. V. Igumenshchev, R. Janezic, S. J. Loucks, J. R. Marciante, J. A. Marozas, F. J. Marshall, D. N. Maywar, J. P. Knauer, P. W. McKenty, S. P. Regan, R. G. Roides, W. Seka, S. Skupsky, V. A. Smalyuk, J. M. Soures, C. Stoeckl, R. Betti, R. L. McCrory, D. D. Meyerhofer, D. Shvarts, J. A. Frenje, R. D. Petrasso, and C. K. Li, "Performance of Direct-Drive Cryogenic Targets on OMEGA," to be published in Physics of Plasmas (invited).

O. V. Gotchev, N. W. Jang, J. P. Knauer, M. D. Barbero, R. Betti, C. K. Li, and R. D. Petrasso, "Magneto-Inertial Approach to Direct-Drive Laser Fusion," to be published in the Journal of Fusion Energy.

J. S. Green, V. M. Ovchinnikov, K. U. Akli, R. G. Evans, H. Azechi, F. N. Beg, C. Bellei, R. R. Freeman, H. Habara, R. Heathcote, M. H. Key, J. A. King, K. L. Lancaster, N. C. Lopes, T. Ma, A. J. MacKinnon, K. M. Markey, A. McPhee, Z. Najmudin, P. Nilson, R. Onofrei, R. Stephens, K. Takeda, K. A. Tanaka, W. Theobald, T. Tanimoto, J. Waugh, L. Van Woerkom, N. C. Woolsey, M. Zepf, J. R. Davies, and P. A. Norreys, "The Effect of Laser Intensity on Fast-Electron-Beam Divergence in Solid-Density Plasmas," to be published in Physical Review Letters.

I. V. Igumenshchev, "Magnetically Arrested Disks and Origin of Poynting Jets: Numerical Study," to be published in the Astrophysical Journal.

Z. Jiang and J. R. Marciante, "Impact of Transverse Spatial-Hole Burning on Beam Quality in Large-Mode-Area Yb-Doped Fibers," to be published in the Journal of the Optical Society of America B.

I. Kang, C. Dorrer, L. Zhang, M. Dinu, M. Rasras, L. Buhl, S. Cabot, A. Bhardwaj, X. Liu, M. Cappuzzo, L. Gomez, A. Wong-Foy, Y. F. Chen, N. K. Dutta, S. S. Patel, D. T. Neilson, C. R. Giles, A. Piccirilli, and J. Jaques, "Characterization of the Dynamical Processes in All-Optical Signal Processing Using Semiconductor Optical Amplifiers," to be published in IEEE Journal of Selected Topics in Quantum Electronics (invited).

R. L. McCrory, D. D. Meyerhofer, R. Betti, R. S. Craxton, J. A. Delettrez, D. H. Edgell, V. Yu. Glebov, V. N. Goncharov, D. R. Harding, D. W. Jacobs-Perkins, J. P. Knauer, F. J. Marshall, P. W. McKenty, P. B. Radha, S. P. Regan, T. C. Sangster, W. Seka, R. W. Short, S. Skupsky, V. A. Smalyuk, J. M. Soures, C. Stoeckl, B. Yaakobi, D. Shvarts, J. A. Frenje, C. K. Li, R. D. Petrasso, and F. H. Séguin, "Progress in Direct-Drive Inertial Confinement Fusion Research," to be published in Physics of Plasmas (review talk).

P. Nilson, W. Theobald, J. Myatt, C. Stoeckl, C. Mileham, M. Storm, O. V. Gotchev, I. A. Begishev, J. Brown, J. D. Zuegel, R. Betti, D. D. Meyerhofer, and T. C. Sangster, "High-Intensity Laser–Plasma Interactions in the Refluxing Limit," to be published in Physics of Plasmas (invited).

A. Simon, "An Alternative Analysis of Some Recent Diffusion Experiments on the LAPD Device," to be published in Physics of Plasmas.

A. Simon, "Comment on 'Two-Dimensional Equilibrium of a Low Temperature Magnetized Plasma' [Plasma Sources Science and Technology **14**, 152–157 (2005)]," to be published in Plasma Sources Science and Technology.

W. Theobald, R. Betti, C. Stoeckl, K. S. Anderson, J. A. Delettrez, V. Yu. Glebov, V. N. Goncharov, F. J. Marshall, D. N. Maywar, R. L. McCrory, D. D. Meyerhofer, P. B. Radha, T. C. Sangster, D. Shvarts, V. A. Smalyuk, A. A. Solodov, B. Yaakobi, C. D. Zhou, J. A. Frenje, C. K. Li, F. H. Séguin, R. D. Petrasso, and L. J. Perkins, "Initial Experiments of the Shock-Ignition ICF Concept," to be published in Physics of Plasmas (invited).

A. Trajkovska-Petkoska and S. D. Jacobs, "Effect of Different Dopants on Polymer Cholesteric Liquid Crystals," to be published in Molecular Crystals and Liquid Crystals.

A. Trajkovska-Petkoska, T. Z. Kosc, K. L. Marshall, K. Hasman, and S. D. Jacobs, "Motion of Doped-Polymer-Cholesteric Liquid Crystal Flakes in a Direct-Current Electric Field," to be published in the Journal of Applied Physics.

Conference Presentations

T. C. Sangster, R. Betti, K. S. Anderson, J. A. Delettrez, V. Yu. Glebov, V. N. Goncharov, F. J. Marshall, D. N. Maywar, R. L. McCrory, D. D. Meyerhofer, P. B. Radha, D. Shvarts, V. A. Smalyuk, R. B. Stephens, C. Stoeckl, B. Yaakobi, C. D. Zhou, J. A. Frenje, C. K. Li, F. H. Séguin, and R. D. Petrasso, "Fast-Ignition Research at the Laboratory for Laser Energetics," 1st International Conference on Ultra-Intense Laser Interaction Sciences, Bordeaux, France, 1–5 October 2007.

The following presentations were made at the 6th International Laser Operations Workshop, Bordeaux, France, 9–11 October 2007:

J. L. Edwards, "Accessing Information and Maintaining Configuration Control of the OMEGA EP Laser System."

R. Janezic, L. M. Elasky, D. R. Harding, and S. J. Loucks, "Cryogenic DT Target Operations in the LLE OMEGA Facility."

B. E. Kruschwitz, L. J. Waxer, and J. H. Kelly, "OMEGA EP Activation Status."

S. J. Loucks, "LLE Overviews."

S. F. B. Morse, "Availability and Effectiveness Planning on OMEGA EP."

G. Pien, "Multi-Facility Diagnostic Development."

A. L. Rigatti, "Operational Issues Related to OMEGA and OMEGA EP Optics."

B. Ashe, K. L. Marshall, D. Mastrosimone, and C. McAtee, "Minimizing Contamination to Multilayer Dielectric Diffraction Gratings Within a Large Vacuum System," 54th AVS International Symposium, Seattle, WA, 14–19 October 2007.

J. R. Marciante, W. R. Donaldson, and R. G. Roides, "Enhanced-Dynamic-Range, Single-Shot Measurement of Nanosecond Pulses via Optical Replication," IEEE/LEOS, Lake Buena Vista, FL, 21–25 October 2007.

T. J. Kessler, "Laser Development at the Laboratory for Laser Energetics," 10th Annual Directed Energy Symposium, Huntsville, AL, 5–8 November 2007.

The following presentations were made at the 49th Annual Meeting of the APS Division of Plasma Physics, Orlando, FL, 12–16 November 2007:

K. S. Anderson, R. Betti, I. V. Igumenshchev, P. W. McKenty, P. B. Radha, W. Theobald, C. Stoeckl, and M. M. Marinak, "Direct-Drive Fuel-Assembly Simulations of Fast-Ignition Cone-in-Shell Implosions."

R. Betti and C. D. Zhou, "Measurable Lawson Criterium and Hydro-Equivalent Curves for Inertial Confinement Fusion."

T. R. Boehly, M. A. Barrios, D. E. Fratanduono, T. C. Sangster, D. D. Meyerhofer, P. M. Celliers, D. Munro, G. W. Collins, O. L. Landen, and R. E. Olson, "Development of Shock-Timing Techniques for the National Ignition Facility."

M. Braaten, C. Brown, S. Padalino, V. Glebov, T. C. Sangster, and T. Duffy, "Measuring Positron Annihilation in Na(Tl) Detectors as the Final Stage in a Carbon Diagnostic."

D. T. Casey, J. A. Frenje, S. C. McDuffee, C. K. Li, J. R. Rygg, F. H. Séguin, R. D. Petrasso, V. Yu. Glebov, D. D. Meyerhofer, S. Roberts, and T. C. Sangster, "The CR-39 Coincidence Counting Technique for Enhanced Signal-to-Background in a Large Range of Charged-Particle Measurements on OMEGA and the NIF."

T. J. B. Collins, J. A. Marozas, P. W. McKenty, P. B. Radha, S. Skupsky, and J. D. Zuegel, "Single-Beam Smoothing Requirements for Wetted-Foam, Direct-Drive NIF Ignition Target Designs."

J. H. Cooley, L. Welser-Sherrill, D. C. Wilson, H. W. Herrmann, J. M. Mack, S. C. Evans, T. J. Sedillo, C. J. Horsfield, D. W. Drew, E. K. Miller, and V. Yu. Glebov, "Evaluation and Modeling of Neutron Reaction Histories Using a Directly Driven Capsule with Two Laser Pulses."

R. S. Craxton, A. M. Cok, and P. W. McKenty, "Initial Polar-Direct-Drive Designs to Optimize Neutron Yields on the NIF."

M. Cummings, K. Donovan, S. Padalino, V. Glebov, and T. C. Sangster, "Elemental Analysis of Carbon Disks Using Proton Induced X-Ray Emission."

J. A. Delettrez, D. Shvarts, P. B. Radha, C. Stoeckl, V. A. Smalyuk, A. V. Maximov, T. C. Sangster, R. D. Petrasso, and J. A. Frenje, "Transport of Energetic Electrons Produced from Two-Plasmon Decay in the 1-D Hydrodynamic Code *LILAC*."

D. H. Edgell, W. Seka, J. A. Delettrez, R. S. Craxton, V. N. Goncharov, I. V. Igumenshchev, J. Myatt, A. V. Maximov, R. W. Short, T. C. Sangster, and R. E. Bahr, "Scattered-Laser-Light Spectroscopy in Direct-Drive Implosion Experiments."

R. Epstein, J. A. Delettrez, V. N. Goncharov, J. P. Knauer, P. W. McKenty, F. J. Marshall, D. Li, P. B. Radha, S. P. Regan, H. Sawada, and B. Yaakobi, "Radiative Transport Modeling Relevant to Cryogenic Implosion Simulation and Diagnosis."

S. H. Fay, C. M. Kuhn, E. E. Smith, S. L. Stephenson, T. C. Sangster, V. Glebov, and S. J. Padalino, "Modeling a Carbon Diagnostic System Using MCNPX."

D. E. Fratanduono, M. A. Barrios, T. R. Boehly, D. D. Meyerhofer, D. G. Hicks, P. M. Celliers, S. Wilks, and J. E. Miller, "Nonequilibrium Conditions in a Shock Front."

J. A. Frenje, D. T. Casey, C. K. Li, J. R. Rygg, F. H. Séguin, R. D. Petrasso, V. Yu. Glebov, D. D. Meyerhofer, and T. C. Sangster, "First Measurements of the Neutron Spectrum Using the Magnetic Recoil Spectrometer (MRS) at OMEGA."

M. Ghilea, D. D. Meyerhofer, T. C. Sangster, D. J. Lonobile, A. Dillenbeck, R. A. Lerche, and L. Disdier, "First Tests on OMEGA of a Bubble Chamber for Neutron Detection."

V. Yu. Glebov, T. C. Sangster, C. Stoeckl, S. Roberts, W. Bittle, J. L. Bourgade, J. L. Leray, and R. A. Lerche, "Neutron-Induced Signal Measurements in Coaxial Cables on OMEGA."

V. N. Goncharov, T. C. Sangster, P. B. Radha, T. R. Boehly, T. J. B. Collins, R. S. Craxton, J. A. Delettrez, R. Epstein, V. Yu. Glebov, S. X. Hu, I. V. Igumenshchev, R. Janezic, S. J. Loucks, J. R. Marciante, J. A. Marozas, F. J. Marshall, D. N. Maywar, J. P. Knauer, P. W. McKenty, S. P. Regan, R. G. Roides, W. Seka, S. Skupsky, V. A. Smalyuk, J. M. Soures, C. Stoeckl, R. Betti, R. L. McCrory, D. D. Meyerhofer, D. Shvarts, J. A. Frenje, R. D. Petrasso, and C. K. Li, "Performance of Direct-Drive Cryogenic Targets on OMEGA" (invited).

O. V. Gotchev, P. Y. Chang, N. W. Jang, J. P. Knauer, D. D. Meyerhofer, R. Betti, C. K. Li, J. A. Frenje, F. H. Séguin, and R. D. Petrasso, "Laser-Driven Magnetic-Flux Compression Experiments on the OMEGA Laser."

D. R. Harding, D. H. Edgell, and L. M. Elasky, "Forming Cryogenic DT Targets for OMEGA."

S. X. Hu, V. A. Smalyuk, V. N. Goncharov, P. B. Radha, J. P. Knauer, T. C. Sangster, D. D. Meyerhofer, I. V. Igumenshchev, J. A. Marozas, and S. Skupsky, "Validation of Thermal Transport Modeling in Direct-Drive Targets Using Planar-Foil Experiments on OMEGA."

I. V. Igumenshchev, V. N. Goncharov, F. J. Marshall, M. J. Bonino, P. W. McKenty, D. D. Meyerhofer, and T. C. Sangster, "The Effect of Target Mounts in Direct-Drive Implosions on OMEGA."

J. P. Knauer, P. B. Radha, V. N. Goncharov, I. V. Igumenshchev, R. Betti, R. Epstein, F. J. Marshall, S. P. Regan, V. A. Smalyuk,

D. D. Meyerhofer, and S. Skupsky, "Rayleigh–Taylor Growth and Spherical Compression Measurements of Silicon-Doped Ablators."

G. A. Kyrala, A. Seifter, N. M. Hoffman, D. C. Wilson, S. R. Goldman, N. D. Delamater, V. Glebov, C. Stoeckl, F. Marshall, C. K. Li, and J. Frenje, "Using Beam Pushing and Pointing to Control Indirect Drive Implosion Symmetry."

D. Li, V. N. Goncharov, I. V. Igumenshchev, and S. Skupsky, "Modeling Ion Heat Transport in ICF Targets."

G. Li, C. Ren, R. Yan, V. N. Goncharov, T. L. Wang, W. B. Mori, and J. Tonge, "Laser Channeling in Millimeter-Scale Underdense Plasmas of Fast Ignition."

J. Lundgren, B. Esham, S. J. Padalino, T. C. Sangster, and V. Glebov, "VELoCiRaPTORS."

J. Mack, C. Young, S. Evans, H. Herrmann, M. Moran, R. Malone, and V. Glebov, "NIF Conceptual Design Studies of Bang Time Diagnostics Using d-t Fusion Gamma Rays."

J. A. Marozas, T. J. B. Collins, C. Dorrer, and J. D. Zuegel, "Alternative Laser-Speckle-Smoothing Schemes for the NIF."

F. J. Marshall, J. P. Knauer, T. C. Sangster, J. A. Delettrez, P. W. McKenty, R. Epstein, V. N. Goncharov, and B. Yaakobi, "X-Ray Spectral Measurements of Cryogenic Capsules Imploded by OMEGA."

A. V. Maximov, J. Myatt, R. W. Short, W. Seka, and C. Stoeckl, "Two-Plasmon-Decay Instability Driven by Incoherent Laser Irradiation."

R. L. McCrory, D. D. Meyerhofer, R. Betti, R. S. Craxton, J. A. Delettrez, D. H. Edgell, V. Yu. Glebov, V. N. Goncharov, D. R. Harding, D. W. Jacobs-Perkins, J. P. Knauer, F. J. Marshall, P. W. McKenty, P. B. Radha, S. P. Regan, T. C. Sangster, W. Seka, R. W. Short, S. Skupsky, V. A. Smalyuk, J. M. Soures, C. Stoeckl, B. Yaakobi, D. Shvarts, J. A. Frenje, C. K. Li, R. D. Petrasso, and F. H. Séguin, "Progress in Direct-Drive Inertial Confinement Fusion Research" (review talk).

P. W. McKenty, A. Shvydky, T. J. B. Collins, J. A. Marozas, S. Skupsky, D. Keller, D. D. Meyerhofer, and R. L. McCrory, "Multidimensional Numerical Investigation of NIF Saturn PDD Designs with 3-D Laser Ray Tracing."

D. D. Meyerhofer, J. H. Kelly, S. J. Loucks, R. L. McCrory, S. F. B. Morse, and C. Stoeckl, "OMEGA EP: Status and Use Planning."

J. Myatt, A. V. Maximov, R. W. Short, and D. D. Meyerhofer, "Design of a Positron–Electron Pair-Plasma Production Experiment on OMEGA EP."

P. Nilson, W. Theobald, J. Myatt, C. Stoeckl, C. Mileham, M. Storm, O. V. Gotchev, I. A. Begishev, J. Brown, J. D. Zuegel, R. Betti, D. D. Meyerhofer, and T. C. Sangster, "High-Intensity Laser–Plasma Interactions in the Refluxing Limit" (invited).

S. Padalino, "Plasma Physics Research at an Undergraduate Institution."

E. Pogozelski, B. See, C. Kieffer, W. Becker, S. Padalino, and C. Sangster, "Impact of Cryogenic Temperatures on the Mechanical Properties of *Steatoda Triangulosa* Spider Silk."

P. B. Radha, J. P. Knauer, T. C. Sangster, V. N. Goncharov, I. V. Igumenshchev, R. Betti, R. Epstein, D. D. Meyerhofer, S. P. Regan, V. A. Smalyuk, S. Skupsky, J. A. Frenje, C. K. Li, and R. D. Petrasso, "Using Doped Ablators on OMEGA to Achieve a Low-Adiabat Cryogenic Implosion at High Intensities."

S. P. Regan, T. C. Sangster, D. D. Meyerhofer, W. Seka, B. Yaakobi, R. L. McCrory, C. Stoeckl, V. Yu. Glebov, N. B. Meezan, B. Kruer, L. J. Suter, E. A. Williams, O. S. Jones, D. A. Callahan, M. D. Rosen, O. L. Landen, S. H. Glenzer, C. Sorce, and B. J. MacGowan, "Hohlraum Hot-Electron Production."

T. C. Sangster, V. N. Goncharov, V. A. Smalyuk, R. Betti, D. Shvarts, P. B. Radha, J. A. Delettrez, D. H. Edgell, R. Epstein, V. Yu. Glebov, R. L. McCrory, P. W. McKenty, D. D. Meyerhofer, F. J. Marshall, W. Seka, S. Skupsky, C. Stoeckl, B. Yaakobi, J. A. Frenje, C. K. Li, R. D. Petrasso, and F. H. Séguin, "High-Areal-Density Cryogenic D_2 Implosions on OMEGA."

H. Sawada, S. P. Regan, P. B. Radha, R. Epstein, V. N. Goncharov, D. D. Meyerhofer, V. A. Smalyuk, T. C. Sangster, B. Yaakobi, and R. C. Mancini, "Investigation of Shock Heating and Heat-Front Penetration in Direct-Drive Targets Using Absorption Spectroscopy."

W. Seka, D. H. Edgell, J. P. Knauer, J. Myatt, A. V. Maximov, R. W. Short, T. C. Sangster, R. E. Bahr, R. S. Craxton, J. A. Delettrez, V. N. Goncharov, I. V. Igumenshchev, and D. Shvarts, "Time-Resolved Absorption in Cryogenic and Room-Temperature, Direct-Drive Implosions" (invited).

R. W. Short and J. Myatt, "Kinetic and Fluid Models of the Filamentation Instability of Relativistic Electron Beams for Fast-Ignition Conditions."

A. Shvydky, I. V. Igumenshchev, D. Keller, J. A. Marozas, P. W. McKenty, and S. Skupsky, "Irradiation Uniformity in Direct-Drive Simulations Using 3-D Ray Trace."

S. Skupsky, V. N. Goncharov, and D. Li, "Nonlocal Ion-Heat Transport and Viscosity in ICF Implosions Using a Quasi-Monte Carlo Approach."

V. A. Smalyuk, J. A. Delettrez, V. N. Goncharov, S. X. Hu, D. D. Meyerhofer, S. P. Regan, T. C. Sangster, D. Shvarts, C. Stoeckl, B. Yaakobi, J. A. Frenje, and R. D. Petrasso, "Effects of Preheating on Compression and Rayleigh–Taylor Growth in Planar Plastic Targets on OMEGA."

A. A. Solodov, K. S. Anderson, R. Betti, V. Gotcheva, J. Myatt, J. A. Delettrez, and S. Skupsky, "Integrated Simulation of Fast-Ignition ICF."

C. Stoeckl, W. Theobald, P. A. Jaanimagi, P. Nilson, M. Storm, J. A. Delettrez, R. Epstein, T. C. Sangster, D. Hey, A. J. MacKinnon, H.-S. Park, P. K. Patel, R. Shepherd, J. Green, K. L. Lancaster, and P. A. Norreys, "High-Brightness ~keV Source Development."

M. Storm, D. D. Meyerhofer, C. Mileham, J. Myatt, P. Nilson, T. C. Sangster, C. Stoeckl, and W. Theobald, "High Spatially Resolved Measurements of MeV Electron Beam Transport Through Solids Using Coherent Transition Radiation."

J. Strain, G. Rawcliffe, J. Katz, K. Fletcher, J. Frenje, and S. MacMullin, "Preparation of Deuterated Polymer Targets for the OMEGA Magnetic Recoil Spectrometer."

S. Sublett, J. P. Knauer, D. D. Meyerhofer, and A. Frank, "OMEGA Laser-Driven Hydrodynamic Plasma Jet Experiments with Relevance to Astrophysics."

W. Theobald, R. Betti, C. Stoeckl, K. S. Anderson, J. A. Delettrez, V. Yu. Glebov, V. N. Goncharov, F. J. Marshall, D. N. Maywar, R. L. McCrory, D. D. Meyerhofer, P. B. Radha, T. C. Sangster, D. Shvarts, V. A. Smalyuk, A. A. Solodov, B. Yaakobi, C. D. Zhou, J. A. Frenje, C. K. Li, F. H. Séguin, R. D. Petrasso, and L. J. Perkins, "Initial Experiments of the Shock-Ignition ICF Concept" (invited).

G. T. Young, S. M. Hupcher, C. G. Freeman, M. A. Stoyer, and T. C. Sangster, "Noble Gas Analysis for the OMEGA Gas Sampling System."

C. D. Zhou and R. Betti, "Hydrodynamic Relations for Direct-Drive, Fast-Ignition Inertial Confinement Fusion Implosions."

V. Yu. Glebov, T. C. Sangster, C. Stoeckl, S. Roberts, C. Mileham, O. Landoas, L. Disdier, M. Houry, M. Briat, B. Brullot, Ph. Bergonzo, H. Hamrita, and D. Tromson, "Development of Fast CVD Diamond Detectors for Inertial Confinement Fusion Experiments," Materials Research Society 2007 Fall Meeting, Boston, MA, 26–30 November 2007.

J. M. Soures, "Research Plans for OMEGA EP," FPA Annual Symposium, Oak Ridge, TN, 4–5 December 2007.